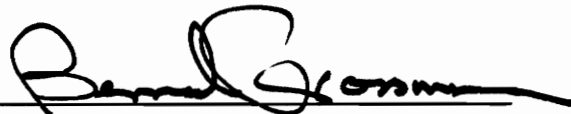# MULTIDISCIPLINARY OPTIMIZATION
OF HIGH-SPEED CIVIL TRANSPORT CONFIGURATIONS
USING VARIABLE-COMPLEXITY MODELING

by

Matthew Gerry Hutchison

Dissertation submitted to the Faculty of the

Virginia Polytechnic Institute and State University

in partial fulfillment of the requirements for the degree of
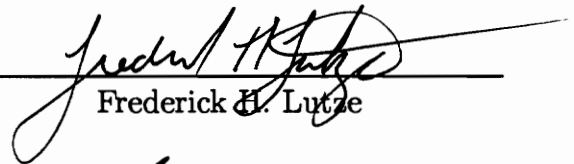
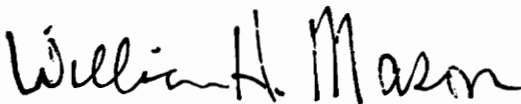DOCTOR OF PHILOSOPHY

in

Aerospace Engineering
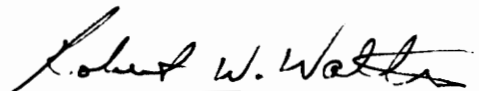
APPROVED:

Bernard Grossman, Chairman

Raphael T. Haftka

Frederick H. Lutze

William H. Mason

Robert W. Walters

March 1993

Blacksburg, Virginia

Abstract

An approach to aerodynamic configuration optimization is presented for the high-speed civil transport (HSCT). Methods to parameterize the wing shape, fuselage shape and nacelle placement are described. Variable-complexity design strategies are used to combine conceptual and preliminary-level design approaches, both to preserve interdisciplinary design influences and to reduce computational expense. The preliminary-design-level analysis methods used to estimate aircraft performance are described. Conceptual-design-level (approximate) methods are used to estimate aircraft weight, supersonic wave drag and drag due to lift, and landing angle of attack. The methodology is applied to the minimization of the gross weight of an HSCT that flies at Mach 2.4 with a range of 5500 n.mi. Results are presented for wing planform shape optimization and for combined wing and fuselage optimization with nacelle placement. Case studies include both all-metal wings and advanced composite wings. The results indicate the beneficial effect of simultaneous design of an entire configuration over the optimization of the wing alone and illustrate the capability of the optimization procedure.

Acknowledgements

I wish to express my heartfelt gratitude to all those who have made my graduate career both successful and enjoyable. To my advisor, Dr. Bernard Grossman, I owe an enormous debt for his contributions to my academic and professional development. His generosity with his time and expertise has been invaluable and I am greatly appreciative. Dr. William Mason, with his years of experience with aircraft design, supplied a practical viewpoint that, I hope, is illustrated in the present work. Over the course of my graduate career, Dr. Raphael Haftka never ceased to amaze me with his incisive reasoning and clear thinking; I found the solutions to many knotty problems while sitting in a chair in his office. To the other members of my committee, Drs. Lutze and Walters, I am grateful for their contributions both to this work and to my graduate education.

I am especially thankful for the generous support of the members of the Vehicle Integration Branch at the NASA Langley Research Center. Their grants funded this research and, quite simply, without this support my graduate career might not have been possible. Sam Dollyhigh, head of the Branch, and Peter Coen, grant monitor, offered many practical suggestions that greatly enhanced the quality of the research. In contrast to the experience of many grantees, working with and for them has been a great pleasure and I can only hope that, in some small way, I have justified their expectations.

Finally, and most importantly, I want to thank my wife Katie. It is a rare woman who would cheerfully encourage her husband to leave a stable job with good benefits to pursue a dream, and I have the great privelege of having married one. She has borne with quiet patience the impecunious and unpredictable life of her graduate-student husband and, with her unique humor and grace, has given me the support necessary to complete my degree. It is to her that this work is dedicated.

Table of Contents

List of Tables

List of Figures

Case

Chapter 1 — Introduction

Aircraft design has always demanded a balance between competing require-
ments to fulfill the design goals. For example, gains in aerodynamic efficiency
obtained by decreasing the wing's thickness may be offset by structural weight in-
creases associated with the thinner structure. Historically, these compromises have
been determined very early in the design process using simple, empirical analysis
tools. Because of the simplicity of the methods, the interplay between the various
disciplines is reasonably straightforward to model and to understand.

Some form of optimization has long been part of this design process. Trade
studies are conducted to determine, for example, the best balance between thrust-to-
weight ratio and wing loading to minimize take-off gross weight. These studies are
often embodied in *carpet plots* or *thumbprints*, which map contours of some objective
(like gross weight) as a function of 2 design parameters. Clearly, this strategy
has been effective—most aircraft flying today were conceived and developed using
such techniques. A difficulty arises, however, when one attempts to simultaneously
change more than two design parameters so as to minimize the objective. The
resulting 4 (or higher) dimensional surfaces are virtually impossible to visualize.

Mathematical optimization theory addresses this difficulty and offers numerical
strategies for finding extrema of functions depending on, in principle, any number of
parameters. In some sense, mathematical optimization methods propose to replace
the multiple trade studies found in the traditional design process with a mathemat-
ical algorithm. In so doing, these methods seek not just an acceptable combination
of the variables in the design, but the *best* combination. Antoine de Saint-Exupèry
captures this idea poetically.[1]

> Have you ever looked at a modern airplane? Have you followed from year
> to year the evolution of its lines? Have you ever thought, not only about
> the airplane but about whatever man builds, that all of man's industrial
> efforts, all his computations and calculations, all the nights spent over

working draughts and blueprints, invariably culminate in the production of a thing whose sole and guiding principle is the ultimate principle of simplicity?

It is as if there were a natural law which ordained that to achieve this end, to refine the curve of a piece of furniture, or a ship's keel, or the fuselage of an airplane, until gradually it partakes of the elementary purity of the curve of a human breast or shoulder, there must be the experimentation of several generations of craftsmen. In anything at all, perfection is finally attained not when there is no longer anything to add, but when there is no longer anything to take away...

Design optimization methods thus attempt to achieve Saint-Exupèry's concept of perfection by replacing "the experimentation of generations of craftsmen" with mathematical algorithms.

The ultimate goal of the design process is to successfully integrate the competing requirements of structures, aerodynamics, controls and propulsion to meet design requirements. The combination requires knowledge of the influence of one discipline upon another; for example, how changes in wing planform for aerodynamic reasons affects the loads placed upon the wing's internal structure. Multidisciplinary design optimization (MDO) schemes attempt to model these interactions to achieve the best integration of the different technologies. In a sense, MDO seeks to systematize the interaction found in the traditional design process. An illustration of this concept may be found in Ref. 2, where F.A. Maxam reviews the development of the highly successful Boeing 727.

Compromises are required in thousands of areas during design work but the successful designs are those wherein as many as possible of the compromises are synergistic. That is, through application of clever, innovative, and highly technically competent engineers and engineering managers many of the requirements can be brought together to complement each other in the total design solution. Obviously, the more the design is put together in this manner the more probable the overall success.

The research presented here demonstrates an approach to the multidisciplinary design optimization of aircraft configurations. The focal point of this work has been the development of efficient supersonic transport configurations as part of NASA's

High-Speed Research program. This particular project has sought to develop design optimization methods that include influences from more than one discipline without incurring excessive computational cost.

Research into MDO strategies and methods has been conducted by a number of workers at Virginia Tech over the last several years. In Ref. 3, the integrated structural-aerodynamic design of a sailplane wing was investigated using simple beam and lifting-line theories. Subsequently, this work was extended to incorporate more advanced finite-element structural analysis and vortex-lattice aerodynamic evaluation.[4] From this early work, focus was shifted towards the integrated design of a subsonic transport wing, again utilizing finite-element and vortex-lattice analyses.[5,6] The addition of active control systems is described by Rais-Rohani.[7] Malone and Mason[8] have investigated more complete configuration optimization using simple, analytic analysis methods.

Outside of this university, McGeer[9] examined the spanwise distribution of lift, chord and thickness on a subsonic wing to minimize induced drag in the presence of weight, friction drag and lift constraints. Gallman, *et al.*[10] have investigated combined aerodynamic-structural optimization for joined-wing aircraft concepts. Wrenn and Dovi[11] used multi-level decomposition techniques[12,13] for the optimization of a subsonic transport wing.

Early work on aircraft configuration optimization (sizing) is presented in Ref. 14. The computer program described there is known as ACSYNT (for AirCraft SYNThesis) and incorporates many conceptual-level analysis methods for use with a numerical optimization procedure. More recently, Stubbe[15] has described a program developed for the sizing optimization of hypersonic vehicles, which again uses simple analytic and empirical analysis methods.

Some of the potential benefits of a multidisciplinary design environment are outlined in Ref. 16, which describes a system of programs developed at Northrop. Welge[17] predicts the benfits obtainable by simultaneous optimization of planform,

engine location and structure using advanced computational fluid dynamics (CFD) analysis methods. Kulfan[18] investigates a number of unusual configuration concepts for supersonic aircraft, and predicts that significant gains in aerodynamic efficiency may be obtained through the use of design optimization and better design integration procedures.

Recent work by NASA researchers pertaining to the High-Speed Civil Transport (HSCT) program is presented in Refs. 19 and 20. Coen, *et al.*[19] present some preliminary results from the High Speed Airframe Integration Research project at the Langley Research Center and provide an overview of the challenges associated with modern integrated design methods. Dovi, *et al.*[20] describe the structural optimization of an HSCT wing using static aeroelastic analysis. Two parametric studies are presented that illustrate the influence of wing thickness and outboard wing sweep on the structural opimization results. Röhl[21] has proposed a similar study, though no results are presented. Chang, *et al.* present HSCT wing shape optimization results that were developed using Euler aerodynamic analysis. In a somewhat different vein, Nelson[23] examines the effects of wing planform on off-design aerodynamic performance of HSCT configurations.

To summarize, much of the research conducted on aircraft design optimization has fallen into one of two broad categories. First, overall configuration optimization has been performed with simple analytic or empirical analysis models (*e.g.*, Refs. 14 and 8). Second, more detailed optimization studies have focused on a specific aircraft component—typically the wing—and have utilized more advanced analysis methods. The research effort described here was motivated, in part, by a perceived gap in these optimization studies: the optimization of an entire aircraft configuration that relies upon reasonably sophisticated analysis methods. The expected benefit of such integrated designs is improved performance over designs whose components (*e.g.*, the wing) have been optimized separately. Thus, the principal goal of this research has been to seek the synergy described by Maxam using optimization

methods in conjunction with relatively detailed analysis techniques.

1.1 — Overview of Analysis Methods

Aircraft design requires the prediction of the system response and performance as a function of the design parameters in three distinct phases: *conceptual, preliminary* and *detailed design.* As the aircraft design progresses through these stages, the analysis methodology becomes increasingly sophisticated. Typically, the *conceptual* design of the system is performed using simple, experience-based algebraic expressions (often in the form of statistical analyses) based on elementary models of the system. In the *preliminary* design phase, system performance is predicted by more complex numerical simulation such as aerodynamic panel methods or structural plate-model approximations. Computational constraints often dictate that the models used at this stage make some simplifying assumptions and may not include all the complicating factors such as nonlinearities. Finally, at the *detailed* design level, the full force of state-of-the-art computation is brought to bear for all analyses.

In the following chapters, design optimization results obtained using what has been termed conceptual-level and preliminary-level analysis methods are presented. Detailed-design-level models, such as Euler aerodynamic analysis or finite-element structural analysis, have not been employed. The methods utilized are described in subsequent chapters. They include methods to estimate an aircraft's supersonic and subsonic aerodynamic performance, and methods to estimate the aircraft weight. Since detailed-design-level analyses were not used, the methods fall into two groups: conceptual and preliminary-level methods. More concisely, these two levels of analysis are referred to as *simple* or *detailed*, respectively.

1.2 — Variable-Complexity Modeling

The principal obstacle preventing the common use of MDO methods is computational expense. Variable-complexity modeling[6,24] seeks to address the expense of interdisciplinary calculation and optimization by coupling simple, conceptual-level

models to more detailed models. This approach provides greater insight and reduced computational cost, while comparing and correcting the performance predicted by simple methods with the more sophisticated techniques.

Two aspects of this technique are presented. First, the difficulty of retaining cross-disciplinary influences is addressed by coupling a detailed analysis model for one discipline with a simple model for another. Specifically, I present results for preliminary aerodynamic designs that include structural considerations through the use of a conceptual-design structures model. Secondly, it is shown that the computational expense associated with repetitive calculation in numerical optimization may be significantly reduced by combining detailed analyses with simple models. In the context of this work, two levels of modeling have been employed in the evaluation of supersonic wave drag and drag due to lift, and in the calculation of landing angle of attack.

Although the work presented here illustrates the use of variable-complexity modeling for preliminary-level design, the methodology should be extendable to more advanced, detailed-design-level methods. In fact, one of the principal goals of this research has been to investigate the implementation of variable-complexity modeling to provide the foundation for extension to more sophisticated analysis techniques.

1.3 — Overview of the Design Problem

In this work, an approach to the design optimization of a high-speed civil transport (HSCT) is demonstrated. An existing HSCT configuration is used as a baseline for the design optimization; the aircraft is shown in Fig. 1.1. It is a 251-passenger, 5500 *n. mi.* range aircraft, designed to cruise at Mach 2.4. This configuration was developed by the Vehicle Integration Branch at NASA's Langley Research Center as a generic HSCT used for technology integration studies. While the design was developed only as a platform for continuing research, it does reflect current advanced configuration design concepts.
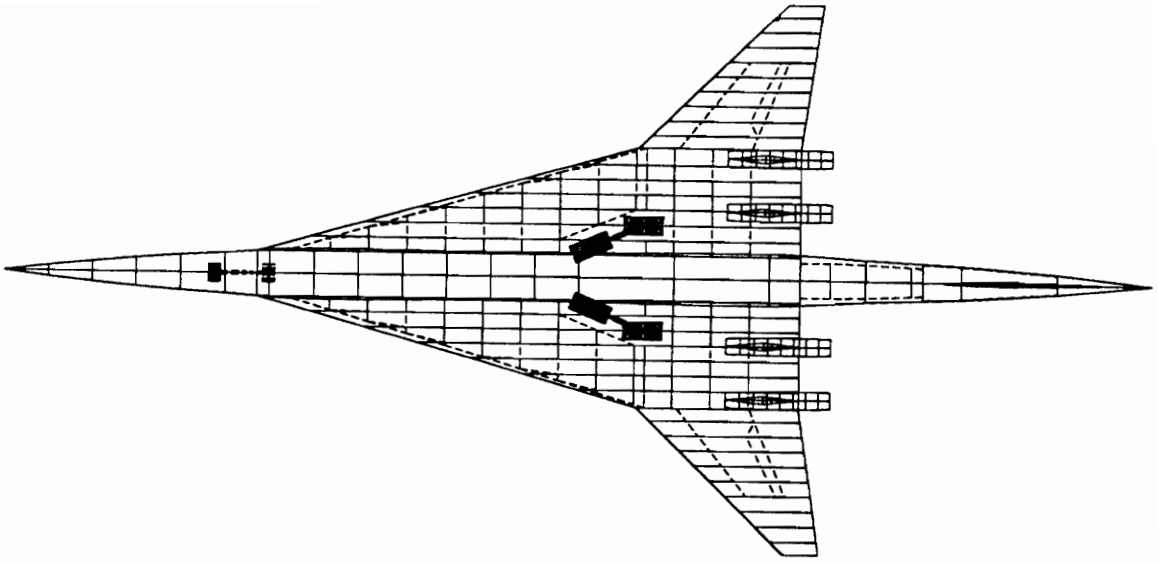
Fig. 1.1 — Baseline Configuration

There are several advantages in using an existing design as a baseline for the optimization. First, a well-designed baseline may be used to derive a reasonable set of design variables, as is shown in Ch. 2. Second, although the initial design in the optimization may or may not be feasible (in the sense of design optimization), a reasonable baseline configuration ensures that the numerical optimizer begins its work in or near the feasible design space. Third, a well-designed baseline serves as a benchmark against which the benefits of design optimization may be assessed. Finally, some portions of the configuration are not addressed (*e.g.,* tail surfaces) and the components from the baseline are used in the analysis that takes place in the optimization.

The design optimization studies, described in detail in Chapters 3 and 6, have centered on optimizing the aircraft configuration for minimum take-off gross weight (TOGW) subject to constraints on performance and geometric arrangement. Typical performance requirements were a minimum range of 5500 *n. mi.* and a maxi-

mum landing angle of attack of 12°. Geometric constraints were employed to keep the configurations physically meaningful; for example, one constraint ensured sufficient wing volume to store the mission fuel, and another specified minimum wing thickness-to-chord ratios.

Throughout the work to be presented, I distinguish between the configuration *definition* and *description*. The configurations are *defined* by a concise set of design variables (parameters), as set forth in the following chapter. By contrast, the configuration is *described* by discrete, numerical data. The Craidon geometry format[25], developed by Charlotte Craidon in the early 1970's at the NASA Langley Research Center, was a convenient choice for this description.

The Craidon geometry defines the fuselage at a number of axial stations by a collection of (y, z) data points. Similarly, the wing is described by airfoil cross-sections (*i.e.*, (x, z) data) at a number of spanwise locations. The engine nacelles (or *pods*) in the Craidon geometry are represented as axi-symmetric bodies. Tail surfaces, fins and canards are assumed to be trapezoidal, with symmetric airfoil sections specified at the root and the tip of the surface. The coordinate axes used in this work are illustrated in Fig. 1.2.

The motivation behind this distinction between aircraft definition and description is a practical one. The analysis methods described later are all programmed as individual routines or modules that depend *only* on the Craidon geometry to determine the characteristics of the configuration. Consequently, the analysis of a given design is independent of the design variables, once the geometry has been defined. This strategy minimizes the effort required to change the number or meaning of a set of design variables, and effectively isolates the analysis modules from the optimization process. Thus, the individual techniques used to define an aircraft and estimate its performance are easily changed or upgraded without repeated overhauls of the entire analysis and optimization framework.

The means used to define the configuration are presented in Ch. 2. In Ch. 3,
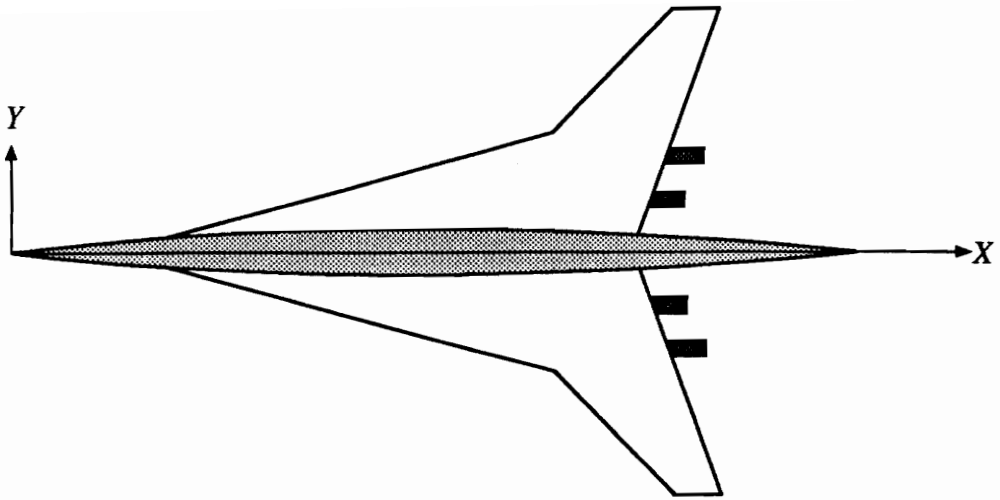
Fig. 1.2 — Coordinate Axes

the strategy employed in the optimization procedure is described. Chs. 4 and 5 present the detailed and simple analysis models used in the work. In Ch. 6, results are presented that illustrate the capability of the optimization methods and in Ch. 7 I conclude with some general observations and recommendations for future work.

Throughout the following discussion, I have made an effort to note the work of Dr. Eric Unger, a fellow researcher on this project, where appropriate. His contributions included the development of one of the approximate landing models, implementation of the ground-effect model and the development of the computational interface for the supersonic wave-drag program. Each of these topics is discussed in detail in later chapters. In addition, he played a key role in the development of the optimization strategies (particularly the appropriate selection of move limits), and with the implementation of the geometric modeling and description methods.

Successful optimization requires a simple yet meaningful mathematical characterization of the aircraft configuration. In the following sections, I describe the methods developed to define the airfoil and wing thickness distribution, the wing planform, the placement of the engine nacelles, the fuselage and a simplified mission profile.

As mentioned in the previous chapter, the methods used to define the configuration were developed to match the baseline design (see Fig. 1.1). Although this configuration was the focus of the work presented here, the geometry definition techniques were also successfully employed to model the wing of a Mach 3.0 aircraft.[24]

2.1 — Airfoil Thickness Distribution

The goal of the development of airfoil thickness distribution models was to define two families of airfoils with a small number of design parameters that have a simple, physical interpretation. Although the baseline configuration has airfoils whose leading edges (LE) are round, work with a Mach 3 configuration[24] led to the development of analytic definitions for both sharp and round-LE thickness distributions. For completeness, both models are presented.

The approach was to determine some function that closely approximated the 6A series airfoils found on the baseline configuration of Ref. 24. The resulting definitions also produced satisfactory agreement with the airfoils on the baseline design of the present work (Fig. 1.1).

The following expressions give the upper surface coordinates of a symmetrical airfoil, normalized by the chord, as z_t. The equations are written as a function of the normalized chordwise location, x/c.

2.1.1 — Round Leading Edge

The thickness distribution for airfoils with round leading edges was based on, though is not the same as, the NACA modified 4-digit airfoil description.[26] The resulting definition depends on 4 parameters:

I The leading-edge radius parameter.

t/c The maximum airfoil thickness-to-chord ratio.

m The x/c location of t/c.

τ_{TE} The trailing-edge half angle.

These 4 parameters are illustrated in Fig. 2.1.
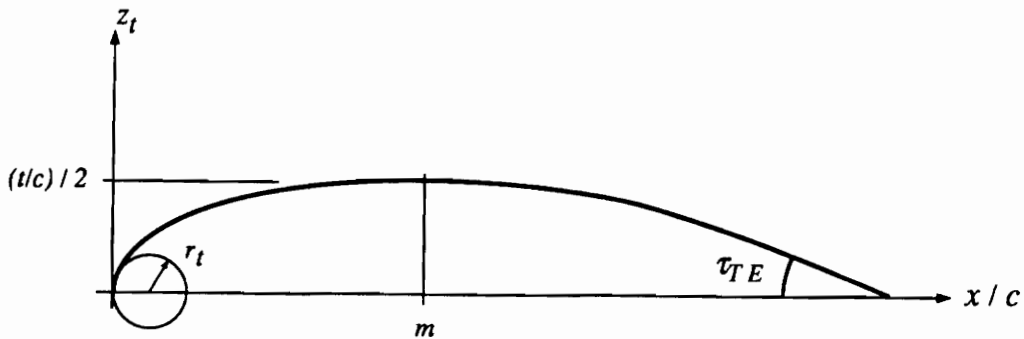
Fig. 2.1 — Round-LE Airfoil Thickness Distribution

The airfoil thickness is defined as z_{t_1} for $0 \leq x/c \leq m$ and z_{t_2} for $m \leq x/c \leq 1$. The functions are

$$z_{t_1}(x/c) = a_0 \sqrt{x/c} + a_1(x/c) + a_2(x/c)^2 + a_3(x/c)^3 \,,$$
$$z_{t_2}(x/c) = d_0 + d_1(1 - x/c) + d_2(1 - x/c)^2 + d_3(1 - x/c)^3 \,. \tag{2.1}$$

The coefficients d_i were determined by requiring that z_{t_2} equal half the airfoil thickness-to-chord ratio at m, the slope of z_{t_2} be zero at m, the thickness at the trailing edge be zero, and the slope at the trailing edge be the tangent of the

trailing-edge half angle. These conditions are written as:

$$z_{t_2}(m) = \frac{1}{2}(t/c)\,,$$

$$\frac{dz_{t_2}}{d(x/c)}(m) = 0\,,$$

$$z_{t_2}(1) = 0\,,$$

$$\frac{dz_{t_2}}{d(x/c)}(1) = -\tan\tau_{TE}\,.$$

(2.2)

Substituting Eq. (2.1) into Eqs. (2.2) and solving for d_i produces

$$d_0 = 0\,,$$

$$d_1 = \tan\tau_{TE}\,,$$

$$d_2 = \frac{3}{(1-m)^2}\left[\frac{t/c}{2} - d_0 - \frac{2d_1}{3}(1-m)\right]\,,$$

$$d_3 = -\frac{d_1 + 2d_2(1-m)}{3(1-m)^2}\,.$$

(2.3)

To define a_i, value and first and second derivative continuity of z_{t_1} and z_{t_2} were enforced at m; that is

$$z_{t_1}(m) = \frac{1}{2}(t/c)\,,$$

$$\frac{dz_{t_1}}{d(x/c)}(m) = 0\,,$$

$$\frac{d^2 z_{t_1}}{d(x/c)^2}(m) = 2d_2 + 6d_3(1-m)\,.$$

(2.4)

Finally, the definition of the NACA modified 4-digit leading-edge radius parameter was employed,

$$r_t = 1.1019\left[(I/6)(t/c)\right]^2 = \frac{a_0^2}{2}\,,$$

(2.5)

where r_t is the leading-edge radius-to-chord ratio.

Using the form of z_{t_1} with Eqs. (2.4) and (2.5) produces

$$a_0 = \sqrt{2r_t}\,,$$

$$a_1 = -\frac{a_0}{2\sqrt{m}} - 2ma_2 - 3m^2 a_3\,,$$

$$a_2 = \frac{a_0}{2}m^{-3/2} - \frac{t/c}{2m^2} - 2ma_3\,,$$

$$a_3 = \frac{1}{m}\left[d_2 + 3d_3(1-m) - \frac{3a_0}{8}m^{-3/2} + \frac{t/c}{2m^2}\right]\,.$$

(2.6)

Fig. 2.2 compares the analytic definition with a representative round-LE airfoil on the baseline configuration of Ref. 24.
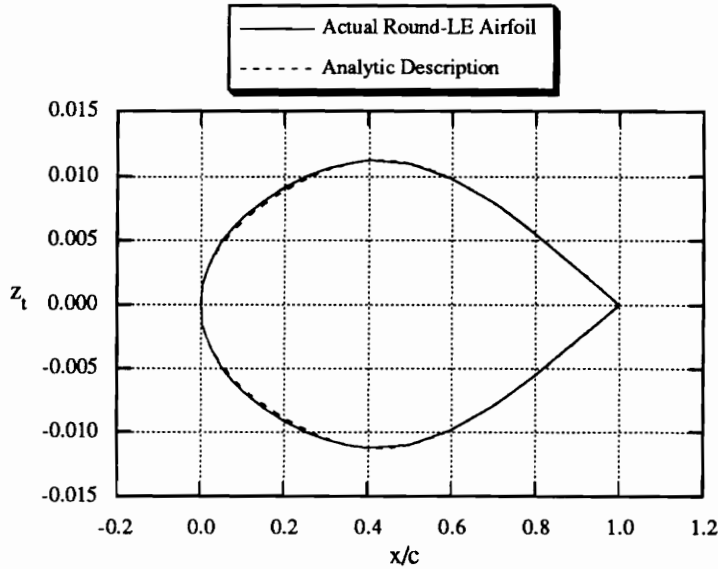
Fig. 2.2 — Comparison of Analytic Thickness Model with Round-LE Airfoil from Baseline Configuration of Ref. 24

2.1.2 — Sharp Leading Edge

Although not used in the results presented here, an analytic definition modeling a sharp-LE airfoil thickness distribution was developed for the work of Ref. 24. This definition depends on 5 parameters:

τ_{LE} The leading-edge half angle.

l The x/c location of the end of the linear section.

t/c The maximum airfoil thickness-to-chord ratio.

m The x/c location of t/c.

τ_{TE} The trailing-edge half angle.

These 5 parameters are illustrated in Fig. 2.3.

The airfoil thickness is defined as z_{t_1} for $0 \leq x/c \leq l$, z_{t_2} for $l \leq x/c \leq m$ and
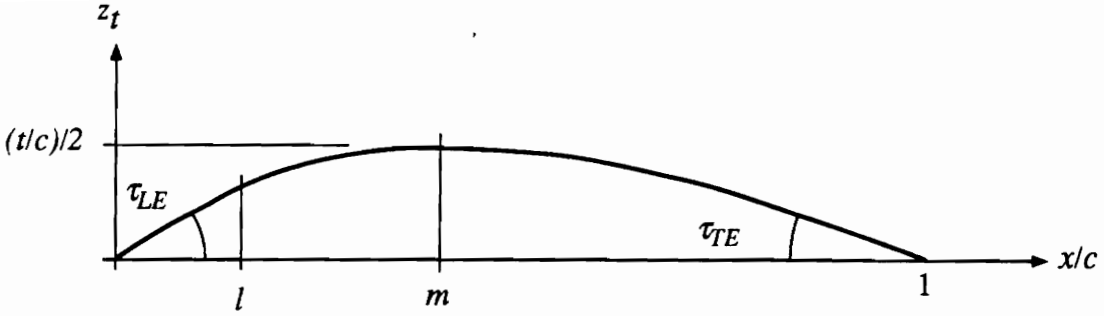
Fig. 2.3 — Sharp-LE Airfoil Thickness Definition Parameters

z_{t_3} for $m \leq x/c \leq 1$. The distributions are

$$z_{t_1}(x/c) = b_1(x/c),$$

$$z_{t_2}(x/c) = c_0 + c_1(x/c) + c_2(x/c)^2 + c_3(x/c)^3,$$ (2.7)

$$z_{t_3}(x/c) = d_0 + d_1(1 - x/c) + d_2(1 - x/c)^2 + d_3(1 - x/c)^3.$$

Note that z_{t_3} here is the same as z_{t_2} in the round-LE definition. The requirements of Eqs. (2.2) were employed for z_{t_3}, and hence the coefficients d_i are defined by Eqs. (2.3).

The coefficient b_1 is determined by requiring the thickness distribution slope at the nose to be the tangent of the leading-edge half angle; hence,

$$b_1 = \tan \tau_{LE}.$$ (2.8)

For c_i, value and slope continuity between z_{t_2} and z_{t_1} at l, and z_{t_2} and z_{t_3} are enforced at m. These conditions are written as

$$
\begin{aligned}
z_{t_1}(l) &= z_{t_2}(l), \\
\frac{dz_{t_1}}{d(x/c)}(l) &= \frac{dz_{t_2}}{d(x/c)}(l), \\
z_{t_2}(m) &= z_{t_3}(m) = \frac{1}{2}(t/c), \\
\frac{dz_{t_2}}{d(x/c)}(m) &= \frac{dz_{t_3}}{d(x/c)}(m) = 0.
\end{aligned}
$$ (2.9)

Using Eqs. (2.7) in Eqs. (2.9) to find c_i produces

$$c_3 = \frac{(l-m)^2}{l^3 + 3lm^2 - 3l^2m - m^3} \left[\frac{b_1}{l-m} - \frac{2}{(l-m)^2} \left(b_1 l - \frac{t/c}{2} \right) \right],$$

$$c_2 = -\frac{b_1 l - \frac{t/c}{2}}{(l-m)^2} + \frac{b_1}{l-m} - c_3 \left[\frac{3l^2}{l-m} - \frac{l^3 - m^3}{(l-m)^2} \right], \qquad (2.10)$$

$$c_1 = \frac{b_1 l - \frac{t/c}{2}}{l-m} - c_3 \frac{l^3 - m^3}{l-m} - c_2(l+m), \quad \text{and}$$

$$c_0 = b_1 l - l^3 c_3 - l^2 c_2 - l c_1.$$

Fig. 2.4 compares the analytic definition with a representative sharp-LE airfoil on the baseline configuration of Ref. 24. In practice, a value of $l = 0.05$ fits the data well for the sharp-LE airfoils and this value was fixed for the work of Ref. 24.
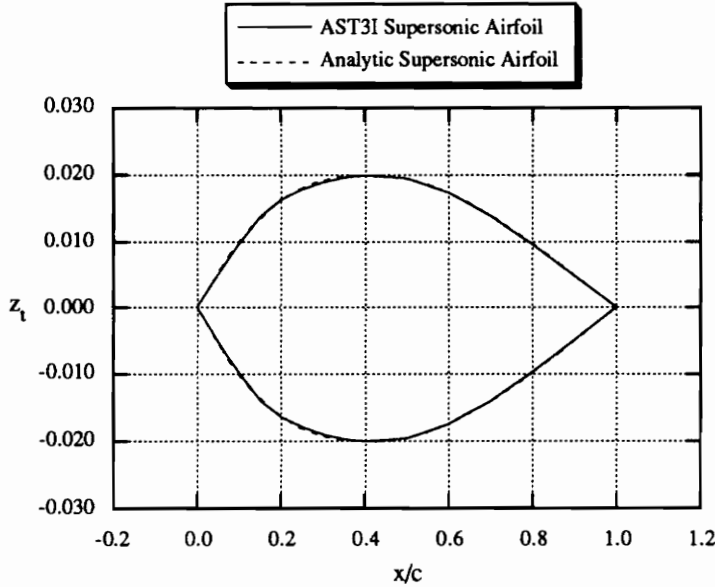
Fig. 2.4 — Comparison of Analytic Thickness Model with Sharp-LE Airfoil from Baseline Configuration of Ref. 24

2.2 — Wing Planform Description

The wing planform is specified by defining the leading and trailing edges using a blending of linear segments. The exponential blending was apparently first used by Barnwell,[27] and was later employed in the successful development of the SC3

wing concept.[28] The leading and trailing-edge equations are defined by the projected intersection points (*i.e.*, the planform breakpoints), the axial location of the wing tip, the wing semi-span and the wing-tip chord. Fig. 2.5 illustrates the planform definition parameters.
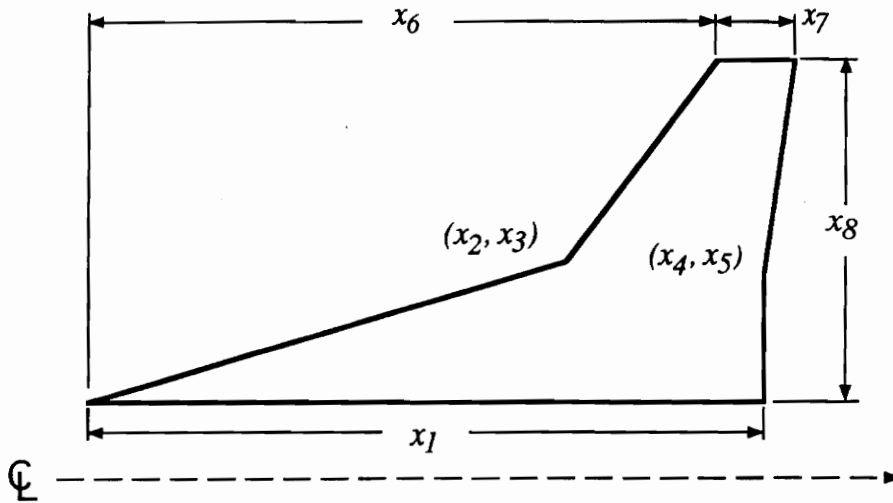
Fig. 2.5 — Wing Planform Parameters

An example of two blended linear segments is shown in Fig. 2.6. The equation for this curve is written as

$$x = A + B_1 y + \frac{(B_2 - B_1)(y - y_1)}{1 - \exp\left[\kappa \frac{B_2 - B_1}{x_1 \delta}(y - y_1)\right]}. \qquad (2.11)$$

The linear-segment slopes are defined as $B_1 = (x_1 - A)/y_1$ and $B_2 = (x_2 - x_1)/(y_2 - y_1)$. The blending parameter δ controls the degree of blending between the segments, with larger values corresponding to a larger blended region. Small values (*e.g.*, $\delta = 0.001$) allow an essentially sharp break between the adjacent segments. The

sign parameter κ is chosen based on the relative magnitudes of B_1 and B_2,

$$\kappa = \begin{cases} -1, & \text{if } B_2 > B_1 \\ 1/(B_2 - B_1), & \text{if } B_2 = B_1 \\ 1, & \text{if } B_2 < B_1. \end{cases} \tag{2.12}$$
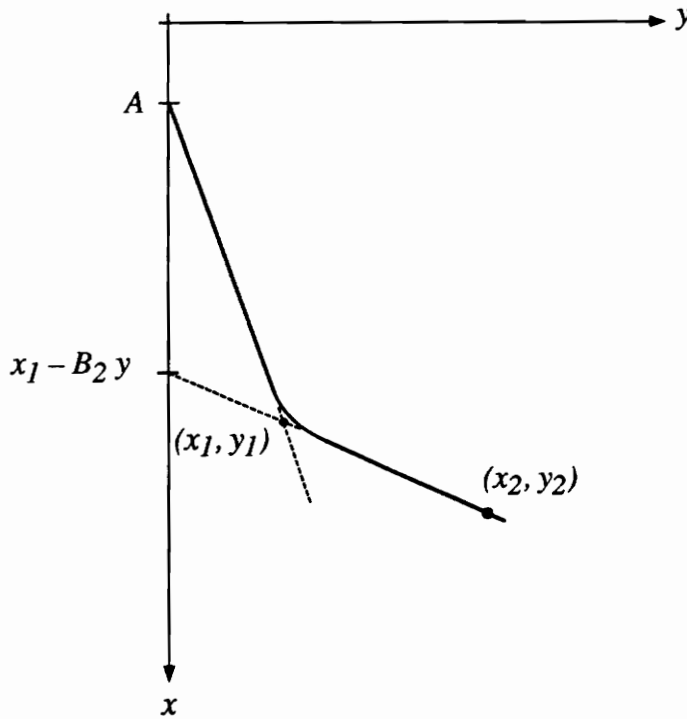
Fig. 2.6 — Blended Linear Equations

For values of $y \ll y_1$, Eq. (2.11) approaches the equation of the first linear segment, $x = A + B_1 y$. For values of $y \gg y_1$, it approaches the equation for the second segment, $x = x_1 - B_2 y_1 + B_2 y$. For $y = y_1$, Eq. (2.11) is singular, but it is easily shown that as $y \rightarrow y_1$, the equation approaches $x = A + B_1 y - \kappa x_1 \delta$. The

choice of κ for the case of $B_2 = B_1$ ensures that the equation reduces mathematically to $x = A + B_1 y$ in this instance.

To define a wing planform, one equation such as Eq. (2.11) is used to form the wing's leading edge and a second for the trailing edge. The parameters A, x_1, x_2, y_1 and y_2 are defined from the wing planform dimensions for both the leading and trailing edges. The principal advantage of the blended linear segment approach is its ability to model configurations with sharp planform breaks, as well as blended planforms. In addition, Eq. (2.11) is readily extended to include three or more linear segments. Although not presented here, this feature was utilized in Ref. 24.

2.3 — Airfoil/Planform Integration

To limit the number of design variables, the airfoil section used at a particular spanwise station is related to the planform at that station by the following rules derived from the baseline configuration:

(1) The wing thickness-to-chord ratio is specified at the wing root, the leading-edge break and the tip. The wing thickness varies linearly between these control points.

(2) The chordwise location of maximum thickness, m, is constant across the span.

(3) The leading-edge radius parameter, I, is constant across the span.

(4) The trailing-edge half angle of the airfoil section varies linearly with the thickness-to-chord ratio according to $\tau_{TE} = 3.03125(t/c) - 0.044188$. This expression was obtained by a least-squares fit of the data found on the baseline configuration.

The advantage accrued by these assumptions is the reduction in the number of parameters (design variables) required to define the wing's thickness distribution. In contrast, a more direct approach might specify I, m, t/c and τ_{TE} at 10 spanwise locations, resulting in 40 thickness design parameters. Clearly, these rules reduce the flexibility available to modify the aircraft design, but this is not necessarily detrimental. On the assumption that the baseline configuration is well designed,

these rules embody to some degree good design practice and are analogous to similar simplifications made in a traditional design process.

2.4 — Nacelle Placement

In this study, the engine nacelle locations are varied during the optimization process. However, for the preliminary-design-level results presented here, thermal and exhaust scrubbing effects are not considered, and hence the axial location of the nacelles are fixed in relation to the wing's trailing edge. A value of 25% nacelle overhang, taken from the baseline configuration, is assumed. Only the spanwise locations of the nacelles are specified. Fig. 2.7 illustrates the nacelle location parameters.
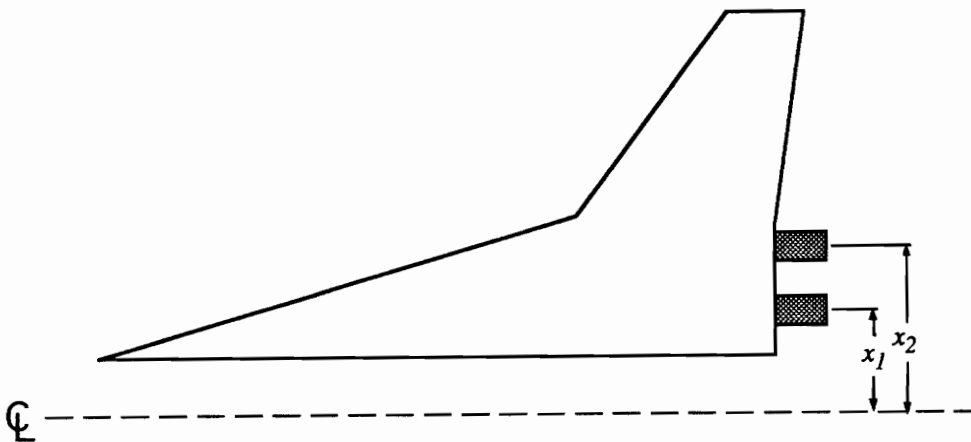
Fig. 2.7 — Nacelle Placement Parameters

2.5 — Axi-symmetric Fuselage Definition

The baseline configuration's fuselage is very nearly axi-symmetric, with the exception of the region near the wing root, where there is some degree of blending. Therefore, to simplify the parametric definition, I have assumed an axi-symmetric

fuselage. The length of the fuselage is fixed at $300\ ft$ and the volume at $23,270 ft^3$, values derived from the baseline. The axial location and radius of each of four *restraint* locations along the fuselage length are the design parameters. The shape of the fuselage between these restraints is defined by requiring that it be a minimum wave-drag body of known volume. "Wave drag" here refers to the supersonic wave drag predicted by linearized-potential theory for bodies in supersonic flow.

In Ref. 29, Eminton develops the methodology for defining such a minimum-drag body. The cross sectional area is given by

$$S(\tilde{x}) = \frac{128V}{3\pi l}\tilde{x}^{3/2}\left(1-\tilde{x}\right)^{3/2} + l^2 \sum_{i=1}^{4} \nu_i \left[\ln\left(\frac{z_1 + 2z_2}{z_1 - 2z_2}\right) + \frac{2z_2}{9}(9z_1 - 64z_2^2)\right],\quad (2.13)$$

where $z_1 = \tilde{x} + k_i - 2\tilde{x}k_i$ and $z_2^2 = \tilde{x}k_i(1-\tilde{x})(1-k_i)$. The quantity V is the required volume, l is the length, $\tilde{x}$ is the normalized axial location x/l and the k_i are the normalized axial locations of the restraints. The constants ν_i are determined by solving the 4×4 linear system resulting from the above expression applied at the four restraint locations.

This formulation is more attractive than simpler alternatives (*e.g.*, a cubic spline) because is generates a low-drag fuselage shape. Thus, in a fashion similar to the rules linking wing planform and thickness distribution, this formulation incorporates "good design practice" directly into the geometry definition.

Fig. 2.8 shows the fit obtained using this method to model the baseline's fuselage. The axial locations chosen for the restraint locations were selected to achieve a reasonable fit with the baseline's fuselage data. For cross-sections of the baseline's fuselage that are not circular, the radius shown in Fig. 2.8 produces the area of the actual cross-section.

2.6 — Mission Definition Parameters

Although not part of the aircraft geometry definition, the specification of a simple mission profile plays an important role in the design process. Three parameters are used to define an idealized cruise mission. One parameter is the mission
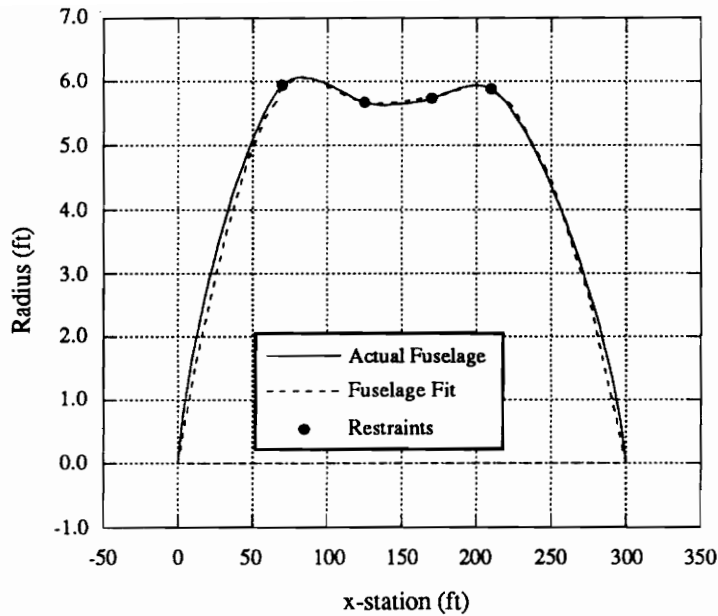
Fig. 2.8 — Parametric Fuselage Fit Compared to the Baseline Fuselage

fuel, and the other two specify the initial cruise altitude and the consant climb rate used in the range calculation (see Ch. 4).

2.7 — Design Variables

The design variables chosen to specify the initial aircraft design were based directly on the geometry definition methods described above. The original design variable values were chosen to define a configuration close to the baseline design. "Close", in this sense, meant first that the design derived from the design variables (*i.e.,* the initial design) appeared geometrically similar to the baseline configuration. Second, and more important, the initial design's performance was expected to be close to that predicted for the baseline.

It should be noted that the initial values for the mission fuel, the cruise-climb rate and the starting cruise altitude were chosen to (approximately) minimize the fuel required to maintain the specified range. Thus, the initial values of the mission

Table 2.1 Initial Wing-Alone Design Variables

Number	Value	Description
1	142.01	Wing root chord (ft)
2	99.65	LE break, x (ft)
3	28.57	LE break, y (ft)
4	142.01	TE break, x (ft)
5	28.57	TE break, y (ft)
6	138.40	LE of wing tip, x (ft)
7	9.30	Tip chord (ft)
8	67.32	Wing semi-span (ft)
9	0.50	Chordwise location of max. t/c
10	4.00	Airfoil LE radius parameter, I
11	2.96	Airfoil t/c at root (%)
12	2.36	Airfoil t/c at LE break (%)
13	2.15	Airfoil t/c at tip (%)
14	290,905	Mission fuel (lbs)
15	50,000	Starting cruise altitude (ft)
16	100.00	Cruise climb rate (ft/min)

definition variables were, if not precisely optimal, nevertheless reasonable.

Two basic types of design problems were considered, those in which only the wing planform and thickness were varied, and those in which the fuselage, the wing and the nacelle locations were varied. I refer to these two problem types as *wing-alone* and *wing-fuselage-nacelle* designs, respectively. For the wing-alone designs, the optimized wing is analyzed in the presence of the fuselage from the baseline. The spanwise locations of the engine nacelles on the wing-alone designs are fixed at the values found on the baseline, though the nacelles move axially with the wing's trailing edge (see Ch. 3). The initial values for the wing-alone designs are shown in Table 2.1, and those selected for the wing-fuselage-nacelle cases in Table 2.2.

As stated previously, an important comparison is the performance predicted by the methods outlined in Chapters 4 and 5 for the baseline configuration, and for the

Table 2.2 Initial Wing-Fuselage Nacelle Design Variables

Number	Value	Description
1	142.01	Wing root chord (ft)
2	99.65	LE break, x (ft)
3	28.57	LE break, y (ft)
4	142.01	TE break, x (ft)
5	28.57	TE break, y (ft)
6	138.40	LE of wing tip, x (ft)
7	9.30	Tip chord (ft)
8	67.32	Wing semi-span (ft)
9	0.50	Chordwise location of max. t/c
10	4.00	Airfoil LE radius parameter, I
11	2.96	Airfoil t/c at root (%)
12	2.36	Airfoil t/c at LE break (%)
13	2.15	Airfoil t/c at tip (%)
14	70.00	Fuselage restraint 1, x (ft)
15	6.00	Fuselage restraint 1, r (ft)
16	135.00	Fuselage restraint 2, x (ft)
17	5.80	Fuselage restraint 2, r (ft)
18	170.00	Fuselage restraint 3, x (ft)
19	5.80	Fuselage restraint 3, r (ft)
20	215.00	Fuselage restraint 4, x (ft)
21	6.00	Fuselage restraint 4, r (ft)
22	17.79	Nacelle 1, y (ft)
23	32.07	Nacelle 2, y (ft)
24	290,905	Mission fuel (lbs)
25	50,000	Starting cruise altitude (ft)
26	100.00	Cruise climb rate (ft/min)

two configurations defined by the initial design variables. Four key parameters—the aircraft range, the landing angle of attack, the take-off gross weight and the wing weight—are compared in Table 2.3. For all three configurations, the mission fuel, the starting cruise altitude and the cruise-climb rate were the same. In addition,

the wings for each were assumed to be metallic in construction. (The means of estimating the weights are presented in Chapter 5.)

Table 2.3 Performance Comparison for Baseline and Initial Designs

	Baseline	Initial W Design	Initial WFN Design
Range (*n. mi.*)	5,404	5,464	5517
Landing Angle of Attack	13.7°	13.7°	13.7°
Take-off Gross Weight (*lbs*)	558,962	559,962	560,138
Wing Weight (*lbs*)	68,181	69,124	69,138

The geometry definition methods described in sections 2.1 through 2.5 could easily be applied to more elaborate aircraft configurations than those presented here. In addition, the definition of individual design variables could be changed without requiring any change in the geometric modeling techniques. Thus, the methods presented in this chapter could be applied to a much broader range of configurations and design variables than are presented in this study.

The numerical optimization is performed using the NEWSUMT-A program.[30] The optimizer modifies the design variables to minimize the objective function, while satisfying the design constraints. NEWSUMT-A is an extended interior penalty function method, with Newton's method used for unconstrained minimization. Second derivatives of the penalty function are approximated from constraint first derivative data.

The primary computational cost of the optimization is not the evaluation of the objective function, but rather the estimation of aerodynamic performance. The numerical optimizer requires several thousand constraint evaluations to complete the optimization, and thus the direct use of the detailed analysis methods (described in the next chapter) is prohibitively expensive. To reduce this expense, a sequential approximate optimization technique is employed in which the overall design process is composed of a sequence of optimization *cycles*. At the beginning of each cycle, approximations to the detailed analyses are constructed. Optimization using the approximate analyses is performed with limits imposed on the allowed change in the design variables (*i.e.,* move limits) to avoid large errors. This approximate problem is converged and the process begins again with new approximations.

In the following sections, the different approximation methods employed in the optimization are described, the design variables are summarized, and the objective function and constraints used are listed. The analysis methods used in the optimization are discussed in Chs. 4 and 5.

3.1 — Approximation Methods

In the following, several approaches to the approximation of a scalar function f that depends on the vector of design variables, $\mathbf{x}$, are described. The function f stands for 4 different aerodynamic parameters used in the estimation of aircraft performance. For the estimation of supersonic wave drag, f represents the wave-drag

coefficient, C_{D_w}. In the calculation of supersonic drag due to lift, f represents two individual parameters: the supersonic lift-curve slope, C_{L_α}, and the leading-edge thrust parameter, C_T/C_L^2. In the estimation of landing performance, f represents the subsonic lift-curve slope at landing, $C_{L_\alpha}|_{ldg}$. Each of these parameters will be discussed in detail in the following chapter. Three approximations are considered: *linear, global-local* and *scaled.*

Linear Approximation. The linear approximation is simply a first-order Taylor series expansion in the design variables about the design point at the beginning of a cycle, $\mathbf{x}_0$, using the detailed analysis f_d,

$$f(\mathbf{x}) \approx f_d(\mathbf{x}_0) + \nabla f_d \cdot \Delta\mathbf{x}, \qquad (3.1)$$

where $\Delta\mathbf{x} = \mathbf{x} - \mathbf{x}_0$ and the gradient ∇f_d is evaluated at $\mathbf{x}_0$. The gradient of f_d is a row vector composed of elements $\partial f_d/\partial x_i$. These partial derivatives are estimated by forward differences; that is, $\partial f_d/\partial x_i \approx f_d(x_i + \Delta x_i)/\Delta x_i$. For smoother functions, the perturbation in the design variables is chosen small enough to obtain an adequate representation of the derivative without incurring excessive roundoff error (*e.g.,* 0.002 design variable perturbation). For noisy functions, small values of the perturbation produce large errors in the derivatives. To reduce this problem, the perturbation size is increased to values larger than the scale of some of the noise (*e.g.,* 0.15 design variable perturbation). These are absolute perturbations in the design variables but, as discussed in §3.2, the design variables are scaled to have values between 0.1 and 10. The noise found in the analyses is numerical in origin and is discussed in more detail in Chs. 4 and 5.

Global-Local Approximation (GLA). This approximation technique, introduced in Ref. 31, utilizes a simple model, f_s, in conjunction with a more detailed analysis, f_d. The approximation uses a linear-scaling technique whereby f is evaluated at $\mathbf{x}$ using

$$f(\mathbf{x}) \approx \sigma(\mathbf{x})f_s(\mathbf{x}), \qquad (3.2)$$

where the scaling parameter is evaluated at the design point at the beginning of a cycle, $\mathbf{x}_0$, as

$$\sigma(\mathbf{x}_0) = \frac{f_d(\mathbf{x}_0)}{f_s(\mathbf{x}_0)} \, . \tag{3.3}$$

The scaling parameter is approximated at $\mathbf{x}$ using a Taylor-series expansion

$$\sigma(\mathbf{x}) \approx \sigma(\mathbf{x}_0) + \nabla\sigma \cdot \Delta\mathbf{x} \, . \tag{3.4}$$

The gradient of σ at $\mathbf{x}_0$ involves differentiating Eq. (3.3) and requires the evaluation of the gradients of both the detailed and simple analyses. As for the linear approximation, forward finite differences were employed. Again, numerical noise in the analysis methods can cause errors in this approximation and the size of the design variable perturbation must be set to minimize this problem to the degree possible. These errors mandate the use of small move limits in the design variables and can increase the number of cycles required for a complete optimization.

Scaled Approximation. Effective simple analysis models produce trends similar to those predicted by the detailed method over a change in the design. Such models suggest the use of a constant scaling function for an approximation,

$$f(\mathbf{x}) \approx \sigma(\mathbf{x}_0) f_s(\mathbf{x}) \, , \tag{3.5}$$

where σ is given by Eq. (3.3).

Two related features of this approach make it appealing: it eliminates the dependence of the approximation function f on derivatives of the detailed analysis and, as a result, the CPU time required to set up the approximation at the beginning of each design cycle is dramatically reduced.

In spite of these advantages, the scaled approximation is of limited use because it does *not* incorporate detailed analysis derivatives. Thus, the optimization becomes almost entirely dependent upon the behavior of the simple analysis model(s). For this reason, the scaled approximation should be employed only when analysis noise makes the derivative-based approximations intractable, or when the detailed

analysis method is so expensive that the evaluation of finite-difference derivatives at the beginning of a design cycle incurs excessive computational cost.

Since the influence of the detailed analyses on the design optimization is determined largely by the derivatives evaluated at the beginning of a design cycle, the order of preference of the three approximation methods is first, the global-local approximation, second, linear approximation and last, scaled approximation. In Ch. 6, I present results obtained using the GLA method. Ref. 24 illustrates the use of all three approximation methods in the design of an HSCT wing.

Clearly, the scaled and global-local approximation methods depend upon reasonably accurate, simple analysis methods. The advantage of incorporating simple models into the approximations (as opposed to the linear approximation) is the larger move limits allowed by the larger (expected) region of accuracy in the design space. The use of simple models for these approximations is one of the two roles variable-complexity modeling plays in this research effort. The other is the use of a simple weight estimation model to represent the influence of structural considerations upon the design.

3.2 — Design Variables

The selection of design variables was based directly on the geometric parameterization methods described in Chapter 2. The variables used in the optimization were selected to model the baseline configuration and were presented in that chapter.

Recall that 16 design variables are required for for the wing-alone optimization cases, and 26 variables for the wing-fuselage-nacelle cases. As described previously, the design variables fall into five basic groups: wing planform, wing thickness, fuselage definition, nacelle placement and mission definition variables. For both wing-alone and wing-fuselage-nacelle sets, each of the design variables is scaled by a power of 10 in the computer implementation so that their magnitudes fall between 0.1 and 10.

3.3 — Objective Function

The objective function chosen for this work was the aircraft take-off gross weight (TOGW). This choice directly incorporates both aerodynamic and structural considerations, in that the structural weight directly affects aircraft empty weight, while aerodynamic performance dictates the mission fuel. In this sense, this objective function captures the multidisciplinary nature of aircraft design.

There are, however, alternatives to TOGW. For example, if fuel efficiency were considered to be of primary importance the mission fuel weight could be the objective function. More fundamentally, the life-cycle cost might be chosen as an appropriate figure of merit (see, for example, Ref. 32). Nevertheless, the TOGW is an important overall measure of aircraft performance and was selected as the objective function for the work presented here.

3.4 — Constraints

The optimization constraints ensure that the aircraft design meets appropriate performance requirements, and that it is geometrically reasonable. The constraints used in this design problem fall into three categories: performance/aerodynamic constraints, geometric constraints, and constraints implicit in the analysis or geometry definition formulation.

In the following sections, each of the constraints is discussed in detail. All that are shown apply to the wing-fuselage-nacelle optimization cases, but not all apply to the wing-alone designs. Constraints that apply only to the wing-fuselage-nacelle cases are labeled *WFN only*. For each constraint, the nominal value used in the optimization is noted.

3.4.1 — Performance/Aerodynamic Constraints

Range. If a minimum range were not enforced for the designs, the optimizer would immediately remove the mission fuel, thereby reducing the gross weight dramatically. The range calculation is described in the following chapter. The range was required to be at least 5,500 *n. mi.*

Landing Angle of Attack. The low-aspect ratio configurations required for efficient supersonic flight have such low values of the subsonic lift-curve slope that considerable effort in the design process must be directed towards limiting the angle of attack at landing to prevent tail scrape. Thus the maximum landing angle of attack (typically, 12°) becomes an important design constraint. The method of estimating landing angle is presented in the following chapter.

This constraint, as well as the other landing constraints, is evaluated at an (approximate) emergency condition. That is, the airport is assumed to be at an altitude of 5,000 *ft*, with an outside air temperature of 90 °*F*. The aircraft is assumed to be carrying 50% of its fuel, and to be landing at 145 *kts*.

Landing Lift Coefficient. A related landing consideration is the maximum lift the wing is capable of producing. A maximum lift coefficient (typically, 1.0) is enforced at the landing condition desribed above. The lift coefficient, C_L, is calculated from

$$C_L = \frac{W}{1/2\rho U_\infty^2 S_w},\tag{3.6}$$

where the wing area, S_w is known for a given configuration and the aircraft landing weight, W, and speed, U_∞, are known from the configuration and the landing conditions. The air density, ρ, is given by

$$\rho = \rho_s \frac{T_s}{T_{ldg}},\tag{3.7}$$

where ρ_s and T_s are the density and temperature (absolute) from the U.S. Standard Atmosphere (see, for example, Ref. 33) at the given airport altitude, and T_{ldg} is the actual air temperature (absolute) at landing.

Landing Wing-Section Lift Coefficients. The final landing-condition constraint limits the maximum section lift coefficient found on the wing (typically, $C_l \leq 2.0$). This constraint is a simple method of avoiding wing designs susceptible to partial wing stalling. Again, the landing conditions are as described above.

The section lift coefficient, C_l, is calculated assuming an elliptic spanwise lift

distribution, and is given by

$$C_l(\eta) = \frac{2C_L S_w}{\pi s c(\eta)} \sqrt{1 - \eta^2}, \tag{3.8}$$

where η is the spanwise y-location normalized by the semi-span, s, and c is the wing chord. The wing's lift coefficient is given by Eq. (3.6). This constraint is evaluated at each of the airfoil definition locations in the Craidon geometry. Thus, in the work presented here, 18 constraints are required to enforce this condition.

3.4.2 — Geometric Constraints

Wing Volume. The mission fuel is assumed to be carried entirely in the wing, and 50% of the total wing volume is assumed to be available for fuel storage. The wing volume is calculated from the Craidon geometry by summing the volumes of the individual prismatic elements defined by the numerical wing description.

Wing Chord. A minimum wing chord (typically, 7 *ft*) was enforced to prevent infeasible planform geometries. Since the leading and trailing edges of the wing are defined by separate blended linear equations, it is mathematically possible for the "leading" edge to be *behind* the "trailing" edge; this constraint prevents such a situation. As for the section lift coefficient limitation, this constraint is evaluated for each of the 18 airfoil definition locations in the Craidon geometry.

Planform Breaks. To ensure physically meaningful wing planforms, the planform breaks are required to be arranged sequentially on the wing. For example, the y-location of the leading-edge break must be less than the wing semi-span.

Thickness-to-Chord Ratios. Minimum thickness-to-chord ratios are enforced at three locations across the wing span: the wing root, the leading-edge break and the wing tip. The minimum value was typically 1.5%.

Fuselage Restraint Locations. As with the planform break locations, several constraints are employed to keep the fuselage restraint x-locations in sequential order. In addition, a minimum spacing between the points (typically, 10 *ft*) is enforced to prevent overlap when the design variables are perturbed during derivative calculations. There are no constraints placed on the fuselage diameter.

Engine Nacelle Spanwise Locations (WFN only). Several constraints are utilized to preserve the order of the nacelles on the wing. In addition, the spanwise location of the outboard engine nacelle is limited to some fraction of the side-of-body to wing-tip distance (typically, 50%). This constraint was employed to represent engine-out and flutter considerations that are not analyzed in the optimization procedure.

3.4.3 — Implicit Formulation Constraints

In several instances, it proved convenient to formulate constraints directly into the analysis or geometry-definition methods. These constraints are thus not part of the formal optimization procedure, in the sense that they do not appear among the constraints presented to the numerical optimizer. They include a maximum cruise altitude constraint, the required fuselage length and volume, a required wing mean-aerodynamic-chord location, and an axial nacelle location requirement.

Maximum Cruise Altitude. The maximum altitude allowed during the cruise mission is enforced as part of the range calculation (see the following chapter). This limitation is imposed to represent cabin depressurization safety considerations. Typically, the maximum altitude was limited to 70,000 *ft*.

Fuselage Volume and Length (WFN only). In an actual aircraft design, many constraints would be placed on the shape and dimensions of the fuselage. Passenger seating, for example, is somewhat difficult to incorporate into an optimization procedure since the seating arrangement, by nature, behaves discretely. As a first attempt at including reasonable geometric requirements, the fuselage volume and length are fixed to the values found on the baseline configuration (23,270 ft^3 and 300 *ft*, respectively).

Recall from Chapter 2 that the length and volume appear as parameters in the equations defining the fuselage cross-sectional area (Eq. 2.13). Thus, these geometric requirements appear directly in the fuselage definition.

Wing Mean Aerodynamic Chord (MAC) Location. The attentive reader may

have noticed that the wing planform design variables (see Ch. 2) completely define the planform shape, but do not specify the wing's axial location. The location is set to satisfy basic stability requirements by positioning its MAC quarter chord at the same axial position as the baseline configuration. The x-location of the wing-root leading edge, $x_{LE_{rt}}$, is given by

$$x_{LE_{rt}} = x_{\bar{c}/4} - \bar{c}/4 - \tilde{x}_{\bar{c}_{LE}} \,, \tag{3.9}$$

where $x_{\bar{c}/4}$ is the desired x-location of the MAC, $\bar{c}$ is the wing's MAC and $\tilde{x}_{\bar{c}_{LE}}$ is the x-location of the leading edge of the MAC relative to the wing root. The MAC is defined by

$$\bar{c} = \frac{2}{S_w} \int_0^{b/2} [c(y)]^2 \, dy \,, \tag{3.10}$$

where b is the wing span, and S_w the wing area.

The x-location of the MAC relative to the wing root is given by

$$\tilde{x}_{\bar{c}_{LE}} = \frac{2}{S_w} \int_0^{b/2} \tilde{x}_{LE}(y)c(y)dy \,, \tag{3.11}$$

where $\tilde{x}_{LE}$ is the wing's leading-edge x-location relative to the wing root. In practice, Eqs (3.10) and (3.11) are integrated numerically using the trapezoidal rule. The desired value of the MAC quarter-chord location, $x_{\bar{c}/4} = 147.3ft$, was taken from the baseline configuration.

Engine Nacelle Axial Location. As noted in Ch. 2, the engine nacelles are fixed axially by the location of the wing's trailing edge, to obviate the consideration of exhaust scrubbing and thermal effects. The nominal 25% overhang is based on the values found on the baseline. Note that, since the nacelles move with the wing's trailing edge, even in the wing-alone designs the nacelles can be positioned axially by the optimizer.

The constraints are summarized in Table 3.1. The nominal values of each of the constraints are indicated and, unless noted otherwise, are the values used in the optimization procedure. Only the optimization constraints are shown; the implicit formulation constraints are not included.

Table 3.1. Optimization Constraints

Number	Description
1	Range $\geq 5,500\,n.mi.$
2	Landing angle of attack $\leq 12°$
3	Landing $C_L \leq 1.0$
4-21	Landing section $C_l \leq 2.0$
22	Fuel volume $\leq$ half of wing volume
23-40	Wing chord $\geq 7.0\,ft$
41	LE break, y $\leq$ wing semi-span
42	TE break, y $\leq$ wing semi-span
43	Root $t/c \geq 1.5\,\%$
44	LE break $t/c \geq 1.5\,\%$
45	Tip $t/c \geq 1.5\,\%$
46	Fuselage: $x_{rest_1} + 10ft \leq x_{rest_2}$
47	Fuselage: $x_{rest_2} + 10ft \leq x_{rest_3}$
48	Fuselage: $x_{rest_3} + 10ft \leq x_{rest_4}$
49	Fuselage: $x_{rest_4} + 10ft \leq 300ft$
50	Nacelle 1, y $\geq$ side-of-body
51	Nacelle 1, y $\leq$ nacelle 2, y
52	Nacelle 1, y $\leq$ nacelle 2, y
53	Nacelle 2, y $\leq$ 50% wing semi-span

In this chapter, the aerodynamic analysis methods employed in the design optimization are described. As was discussed in Ch. 1, there is a heirarchy of analysis techniques that parallel the stages of design refinement; that is, analyses are often referred to as conceptual-design-level, preliminary-design-level or detailed-design-level methods. I denote the two levels of analysis used in this work as *detailed* and *simple* methods; terms which refer, respectively, to preliminary-design-level and conceptual-design-level analysis methods.

The aerodynamic methods presented in this chapter are founded upon linearized-potential theory and boundary-layer theory. Thus the aerodynamic lift forces are based upon the assumption that the wing is thin, and drag forces are assumed to be composed of three components: wave drag, drag due to lift and skin-friction. Linear-theory methods can be expected to produce reasonably accurate results for the slender fuselages and thin wings found in this class of aircraft. Moreover, the flight conditions of interest (cruise and landing) are not characterized by high levels of flow non-linearity for well-designed configurations.

Fundamentally, the basic flight characteristics of interest—range and landing angle of attack—are not aerodynamic quantities. Of course, the aerodynamic performance must be determined to estimate these characteristics, and so the first portion of this chapter is dedicated to the description of the methods used to analyze the aerodynamic behavior of the configuration. Specifically, the calculations contributing to the supersonic drag polar and subsonic lift curve are described. The second portion of the chapter deals with the estimation of range and landing angle of attack given this aerodynamic information.

4.1 — Aerodynamic Analysis Methods

The calculation of the aircraft range depends upon the relation between aircraft lift and drag; that is, the determination of the drag polar. Using the linear-theory

assumption, this calculation is broken down into three separate calculations: supersonic wave drag, drag due to lift, and skin friction drag. Each of the methods employed for these analyses is discussed separately. The estimation of the aircraft drag polar, which depends upon these calculations, simulates the effect of a proper wing-camber design and is described separately.

Subsonically, the analysis requirements were driven by the landing angle of attack calculation. Thus, lift vs. angle of attack information was necessary but a drag calculation was not. For the slender wing planforms found in this class of aircraft, non-linear vortex-lift effects were incorporated into the basic linear-theory method, as well as an empirical model for estimating the influence of ground effect.

4.1.1 — Supersonic Wave Drag

In Ref. 35, the far-field wave drag, D_w, of a slender body of revolution with unit length and cross-sectional area S is given by

$$\frac{D_w}{q} = -\frac{1}{\pi} \int_0^1 S''(x)dx \int_0^x S''(x_1) \ln(x - x_1)dx_1 \,, \tag{4.1}$$

where $x = 0$ corresponds to the nose of the body and $x = 1$ to the base (or tail), and q is the dynamic pressure. The derivation of Eq. (4.1) requires that $S'(0) = S'(1) = 0$.

In 1936, von Kármán observed that upon setting $\Gamma = U_\infty S'(x)$, Eq. (4.1) becomes identical to the expression for the vortex drag of a lifting wing. This remarkable feature suggests the introduction of a Glauert-like transformation, $x = (1 - \cos\theta)/2$, similar to the one utilized in lifting-line theory. The first derivative of the cross-sectional area may then be expressed by the Fourier series

$$S'(x) = \sum_{n=1}^{\infty} A_n \sin(n\theta) \,. \tag{4.2}$$

The cross-sectional area, obtained by integrating Eq. (4.2), may be expressed as

$$S(x) = N + \frac{A_1\theta}{4} + \frac{1}{4}\sum_{n=1}^{\infty} \frac{1}{n}(A_{r+1} - A_{r-1})\sin(n\theta) \,, \tag{4.3}$$

where $N = S(0)$ is the area at the nose of the body, and $A_0 \equiv 0$. The wave drag is then expressed as

$$\frac{D_w}{q} = \frac{\pi}{4} \sum_{n=1}^{\infty} n A_n^2 . \tag{4.4}$$

In Ref. 36, Eminton and Lord citing an expression similar to Eq. (4.1) remark, "The development of this result has aroused interest in two problems: the derivation of the optimum area distribution for minimum wave drag under certain specified conditions and the numerical evaluation of the wave drag of a specified area distribution. These apparently distinct problems have hitherto been treated separately, but it is shown here how an attempt to solve the first problem has led to a practical method of solving the second."

Thus, the method of Eminton and Lord, which has become the classical technique for estimating slender-body wave drag, finds the shape of the body passing through M area *restraint* locations which minimizes wave drag. Formally,

$$\text{minimize:} \quad \frac{D_w}{q} = \frac{\pi}{4} \sum_{n=1}^{\infty} n A_n^2$$

$$\text{such that:} \quad S(x_1) = N + \frac{A_1 \theta_1}{4} + \frac{1}{4} \sum_{n=1}^{\infty} \frac{1}{n} (A_{r+1} - A_{r-1}) \sin(n\theta_1) \tag{4.5}$$

$$\vdots$$

$$S(x_M) = N + \frac{A_1 \theta_M}{4} + \frac{1}{4} \sum_{n=1}^{\infty} \frac{1}{n} (A_{r+1} - A_{r-1}) \sin(n\theta_M) .$$

This problem may be solved by application of the theory of constrained minimization using Lagrange multipliers (see, for example, Ref. 37), but it is complicated by the presence of the infinite series.

In Ref. 38, Eminton develops a closed-form equivalent to this infinite series and derives the following expression for the wave drag,

$$\frac{D_w}{q} = \frac{4}{\pi} (B - N)^2 + \pi \sum_{i=1}^{M} \sum_{j=1}^{M} \lambda_i \lambda_j p(x_i, x_j) , \tag{4.6}$$

where B is the area of the body at the base and x_i are the locations at which $S(x_i)$ are specified. The constants (Lagrange multipliers) λ_i are determined from the solution of the M linear equations developed from the requirement of a minimum-wave-drag body,

$$\sum_{i=1}^{M} \lambda_i p(x_i, x_j) = (S_j - N) - (B - N)u(x_j) \quad \text{for } j = 1, 2, \ldots, M,\qquad (4.7)$$

where $S_j \equiv S(x_j)$. The functions u and p are given by

$$u(x) = \frac{1}{\pi} \left[\cos^{-1}(1 - 2x) - 2(1 - 2x)\sqrt{x(1 - x)} \right],\qquad (4.8)$$

and

$$p(x, y) = -\frac{1}{2}(x - y)^2 \ln\left[\frac{x + y - 2xy + 2\sqrt{xy(1 - x)(1 - y)}}{x + y - 2xy - 2\sqrt{xy(1 - x)(1 - y)}} \right] + \\ 2(x + y - 2xy)\sqrt{xy(1 - x)(1 - y)}.\qquad (4.9)$$

Eqs. (4.6) and (4.7) relate the supersonic wave drag of an axi-symmetric body to its cross-sectional area, but they are not directly applicable to the estimation of a general aircraft configuration's wave drag. The supersonic *area rule* relates an aircraft to a family of *equivalent* axi-symmetric bodies. The wave drags of these equivalent bodies may then be evaluated by Eqs. (4.6) and (4.7).

Following Harris,[39] each equivalent body of revolution is determined by passing a series of parallel cutting planes through the aircraft configuration. The cutting planes are inclined with respect to the aircraft axis at the Mach angle. The area of the equivalent body at each station is the projection onto a plane normal to the aircraft axis of the area intercepted by the cutting plane.

Since the cutting planes are inclined with respect to the aircraft axis, the projected normal area depends on both the axial location and on the roll angle of the cutting plane; see Fig. 4.1. It is this roll angle dependence that mandates that an aircraft be represented by a collection of equivalent bodies, and not a single one.

Given this family of bodies, the wave drag of each is calculated and the wave drag of the aircraft is then taken to be the average of the equivalent-body drags,

$$\left(\frac{D_w}{q}\right)_{avg} = \frac{1}{2\pi} \int_0^{2\pi} \frac{D_w(\theta)}{q} d\theta, \tag{4.10}$$

where θ is the cutting-plane roll angle.
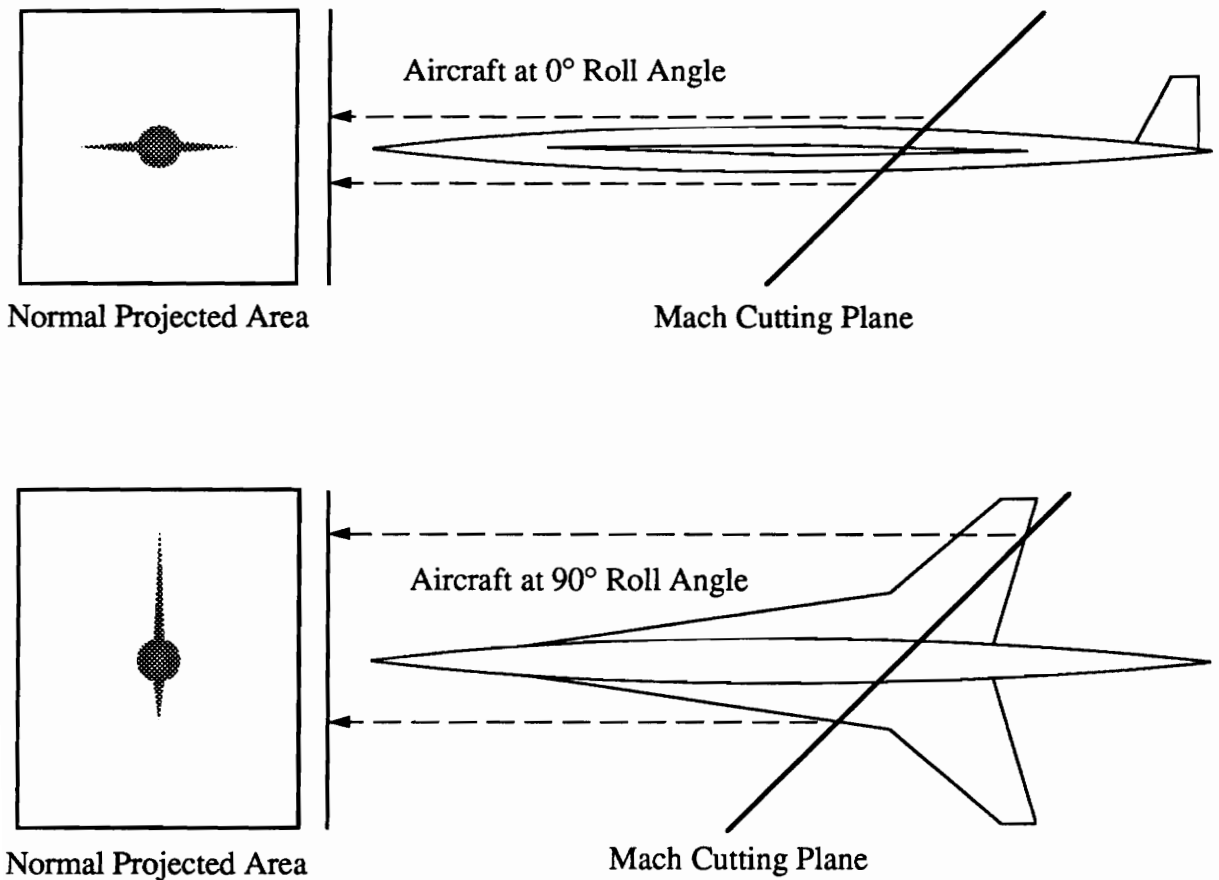
Fig. 4.1 — Mach Cutting Plane and Normal-Area Projection for Two Cutting-Plane Roll Angles

The numerical implementation of this method was developed by Boeing for NASA during the US Supersonic Transport Program. It is known as the Harris code, and has become a de-facto standard;[39] this program serves as the detailed analysis

method for the design optimization. It was modified only as required to mesh with the optimization and performance evaluation modules; no changes were made to the central computational portions of the code. Dr. Eric Unger implemented the interface between the Harris code and the other analysis modules.

One of the equivalent-body area distributions generated by the Harris code for the baseline configuration is shown in Fig. 4.2. This equivalent body was for $\theta = -90°$ and $M = 2.4$. In Ch. 5, I present the methodology developed for a simple wave-drag model that depends upon a geometric approximation to the supersonic area rule. One measure of the success of the simple model will be a comparison with area distributions similar to that shown in the figure.
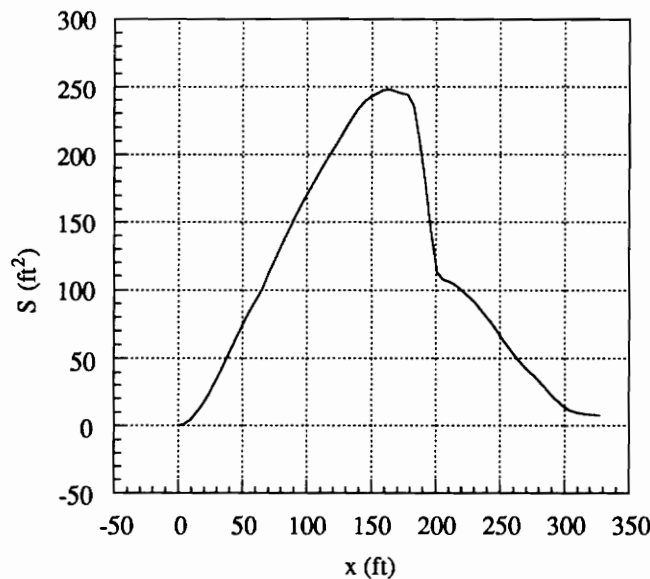
Fig. 4.2 — Equivalent-Body Area Distribution Derived from Baseline Configuration (Harris Code, $\theta = -90°$, $M = 2.4$)

Fig. 4.3 illustrates the variation of equivalent-body wave drag with cutting plane roll angle. The configuration was again the baseline, and the Mach number was 2.4.
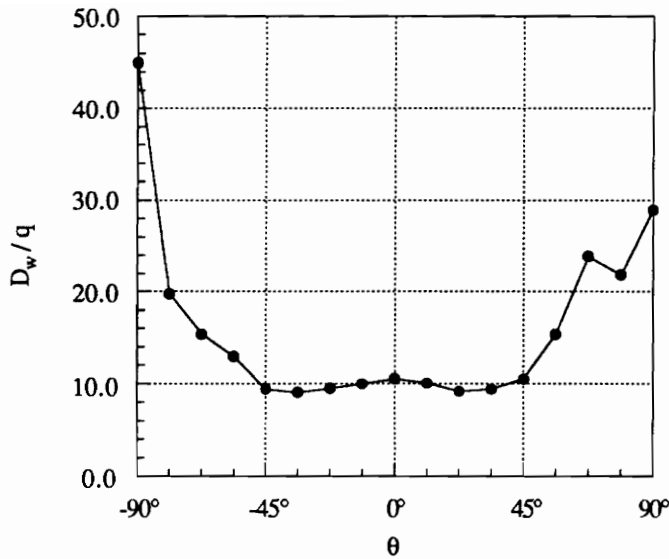
Fig. 4.3 — Variation of Wave Drag with Cutting-Plane Roll Angle for Baseline Configuration (Harris Code, M = 2.4)

4.1.2 — Supersonic Drag due to Lift

The drag due to lift of the entire aircraft configuration is assumed to be given by the drag due to lift of the wing only; see Fig. 4.4. Further, the drag is assumed to be well approximated by a thin wing with linearized boundary conditions and, thus, linearized potential theory is applied.

For a wing of zero thickness lying essentially in the $z = 0$ plane, the linearized-potential theory problem definition may be stated as

$$\beta^2 \phi_{xx} - \phi_{yy} - \phi_{zz} = 0 \quad \text{with boundary conditions:}$$
$$\phi_z(x, y, 0) = U_\infty \frac{\partial z_c}{\partial x}(x, y) \text{ on the wing,}$$
$$\phi_x(x, y, 0) = 0 \text{ off the wing,} \tag{4.11}$$
$$\phi \to 0 \text{ far upstream from the wing,}$$

where ϕ is the perturbation velocity potential, the perturbation velocity components are given by $\nabla\phi = (u, v, w)$, and $\beta = \sqrt{M^2 - 1}$. The first boundary condition ensures flow tangency on the wing, and the second implies that aerodynamic

Note: leading and
trailing edges are
projected to centerline

Actual Configuration — Wing Used for Drag-Due-to-Lift Calculation
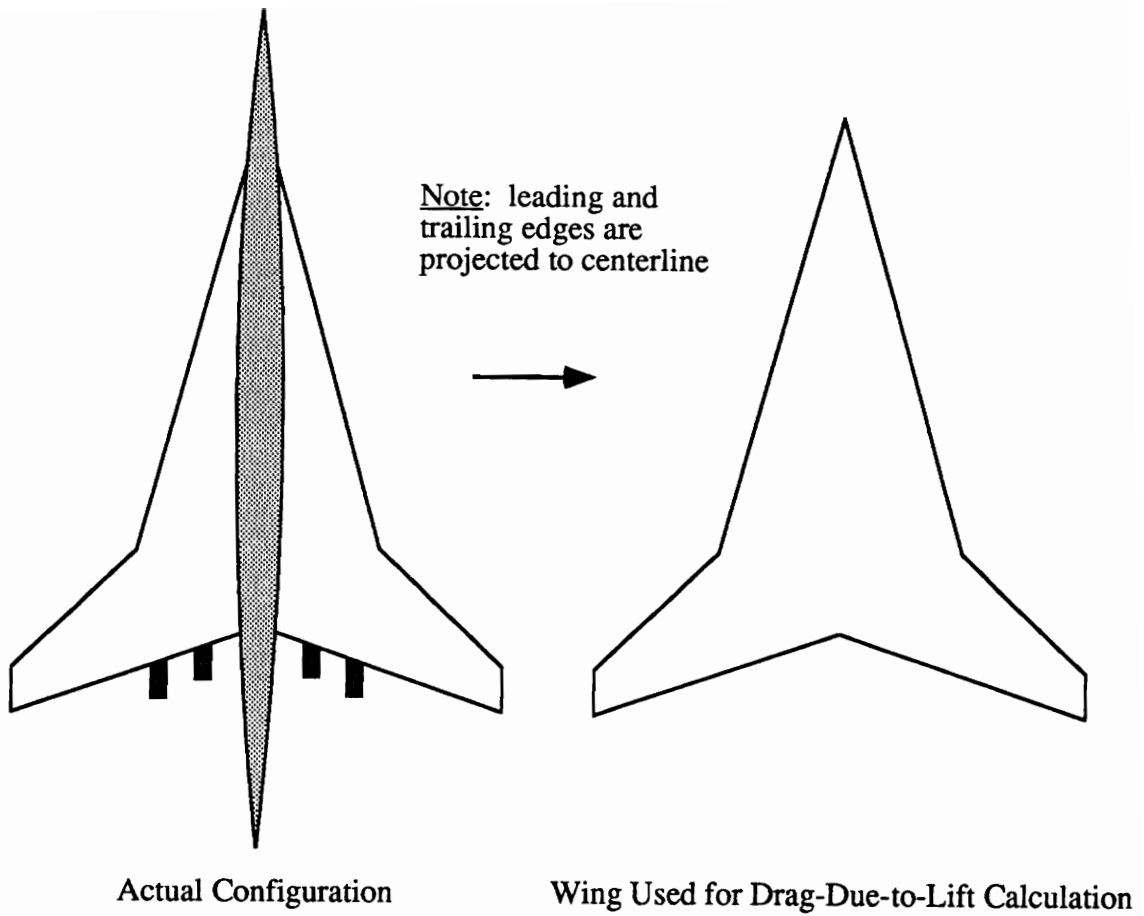
Fig. 4.4 — Wing Only, used for Supersonic Drag due to Lift Calculation

loads (*i.e.*, pressures) can only be carried by the wing and not off the wing. This second condition is obvious when the linearized form of the pressure coefficient, $C_p(x, y) = -(2/U_\infty)u = -(2/U_\infty)\phi_x$, is recalled. Note that both surface boundary conditions are enforced in the $z = 0$ plane, which is consistent with the linearization of the problem. The final condition simply ensures that the perturbation potential vanishes in the far field.

The solution to the problem posed by Eq. (4.11), developed in Ref. 40, is given

by

$$\Delta C_p(x,y) = -\frac{4}{\beta}\frac{\partial z_c}{\partial x}(x,y) + \frac{16}{\beta\pi}\iint\limits_{\tau}\frac{(x-\xi)\Delta C_p(\xi,\eta)\,d\eta\,d\xi}{(y-\eta)^2\sqrt{(x-\xi)^2-\beta^2(y-\eta)^2}} \qquad (4.12)$$

where $\beta = \sqrt{M^2-1}$ and z_c is the wing's camber surface. The hash marks in the integral signs indicate the use of the Cauchy principle-value theorem at singular points (see Ref. 37). The region of integration, τ, extends over the wing planform within the forward Mach cone from the field point (x,y); see Fig. 4.5.
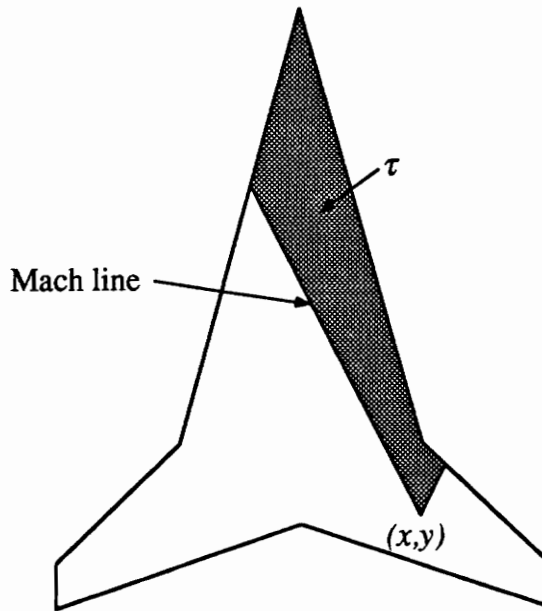
Fig. 4.5 — Region of Integration for Drag-due-to-Lift Solution

To estimate the supersonic drag due to lift of the wing, a panel code based directly on the methods of Carlson, *et al.*[41,42,43] was developed. The solution method numerically evaluates the integral solution given by Eq. (4.12). As described in Ref. 41, the method depends upon a simple rectangular paneling scheme for the numerical solution, with partial panels used to approximate the leading and trailing edges of the wing. An example of a wing and the panels used to model it are

shown in Fig. 4.6. This particular solution technique has been employed in similar programs known collectively as "Mach-box" methods. In an actual solution, many more panels would be employed; for example, 40 spanwise panels were used in the present work.
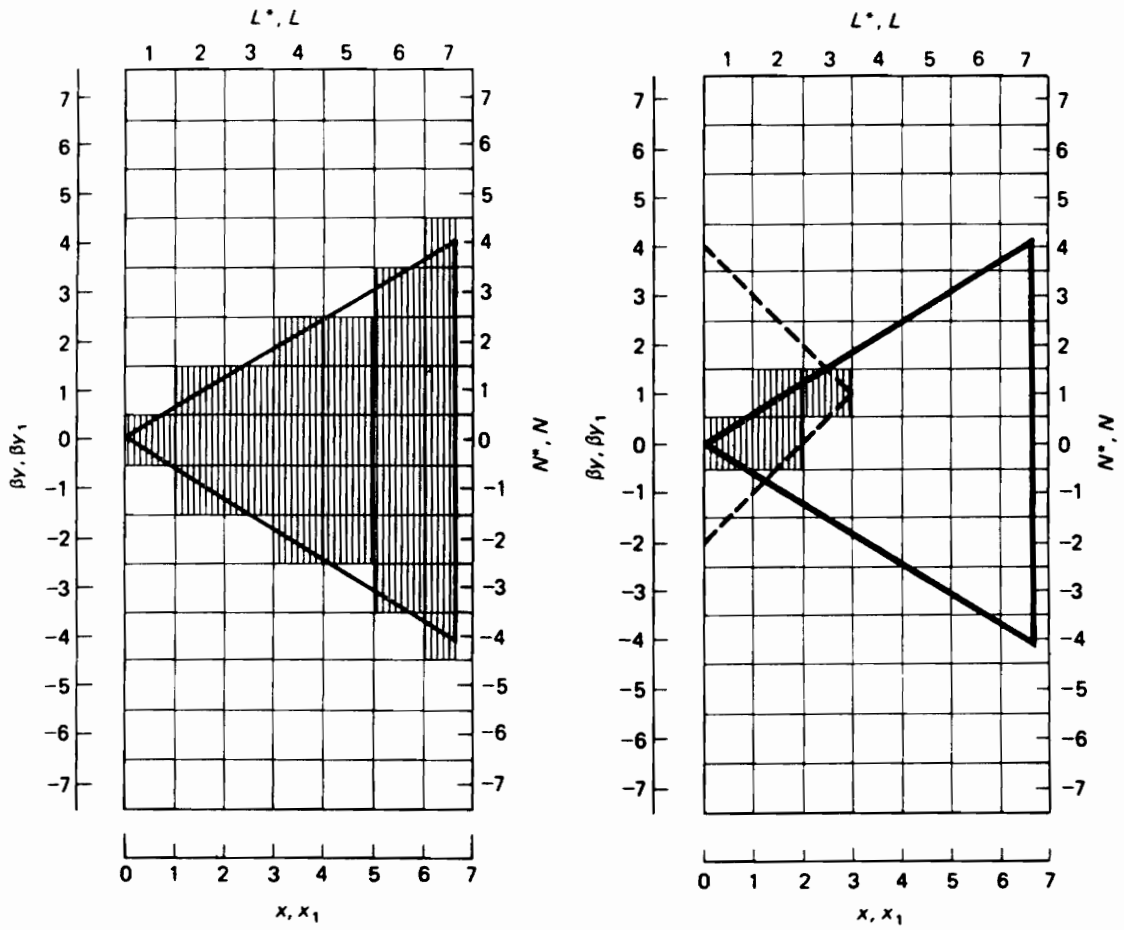
Fig. 4.6 — Paneling Scheme for Supersonic Drag-due-to-Lift Analysis (from Ref. 41)

This simple paneling method, which is an intimate part of the solution scheme, changes the number of panels with changes in wing planform. For example, if the leading edge of the planform shown in Fig. 4.6 were swept forward, the number

of panels modeling the wing would increase. This behavior, and the accompanying small variations in the flow solution, has little effect on the estimation of single-point design performance (the role for which the panel method was originally conceived), but presents difficulties in the optimization procedure, where analysis solutions are assumed to vary continuously. This issue is discussed further in the following chapter.

To verify the general validity of the method implementation, I have compared the results predicted by the panel code with analytic solutions for wings of simple planform. These analytic solutions were derived from conical-flow theory using the methods of Ref. 44. Two cases were considered, a simple delta wing with subsonic leading edges, and a clipped delta wing with supersonic leading edges. These two planforms are shown in Fig. 4.7. For comparison with the panel code, the ΔC_p distributions at several spanwise stations were examined. For the subsonic-LE delta wing, the flow is conically self-similar and, thus, only the 50% semi-span station was investigated. For the supersonic-LE clipped delta wing, the 30% and 60% semi-span locations were examined. For both cases, the Mach number was $M = \sqrt{2}$.

The calculated and analytic pressure distributions are presented in Figs. 4.8, 4.9, and 4.10. In Fig. 4.8 the agreement is quite good, with the panel code capturing the pressure singularity at the leading edge quite well. For the supersonic-LE clipped-delta results shown in Figs. 4.9 and 4.10, the agreement is less favorable. Some minor oscillations in the numerical solution occur at the leading edge, and there is some smearing of the data near the Mach lines (linearized shocks). Nevertheless, the panel code is in reasonable agreement with the analytic solutions and may be expected to produce reasonable aerodynamic estimates.

For the calcuation of drag, integration of the normal pressure forces over the wing planform produces drag estimates in excess of actual values. This discrepancy may be explained by recalling that the thin-wing approximation is simply the limiting case of an actual wing with thickness reduced to zero. In this limit, for leading
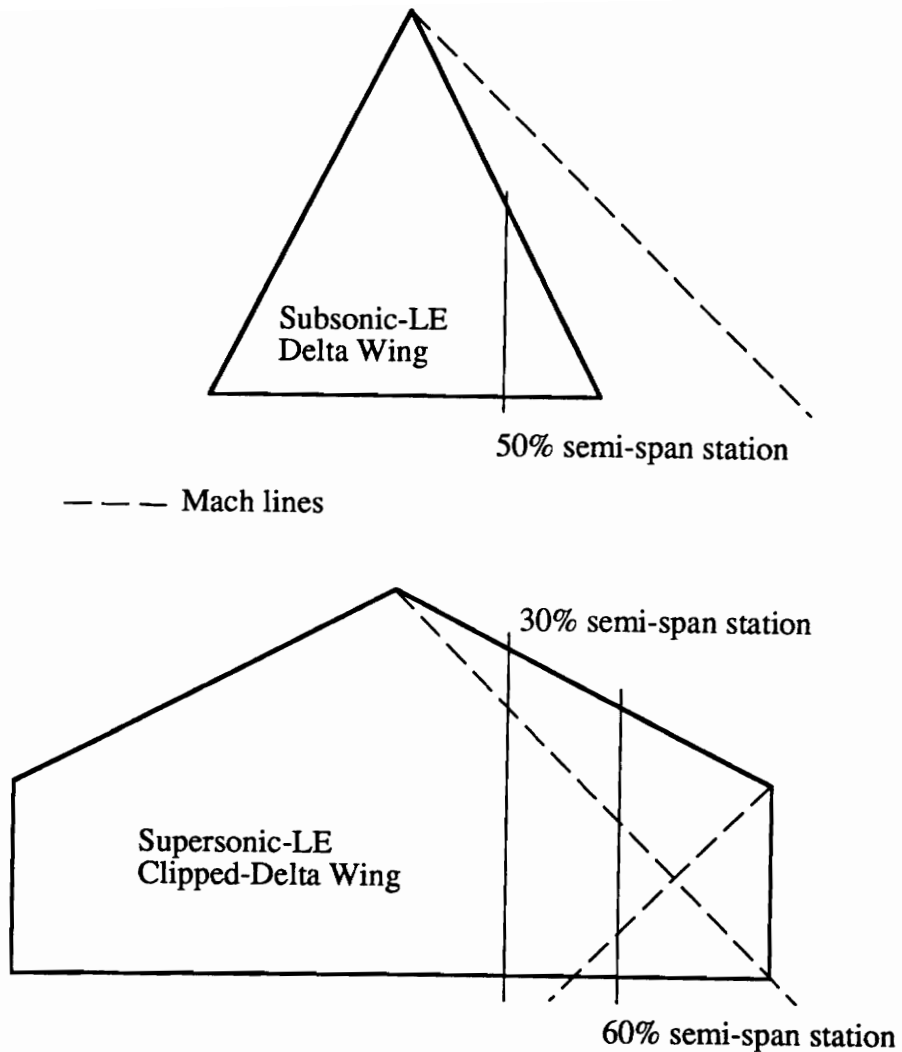
Fig. 4.7 — Wing Planforms for Comparing Analytic Solution and Supersonic Panel Code Predictions

edges of the wing with subsonic flow normal to the edge, the high velocity due to the upwash around the leading edge becomes a velocity singularity. Similarly, ΔC_p at the leading edge increases while the area upon which it acts decreases until, in the limit, an infinite pressure acts upon zero area (see Fig. 4.8 for an example of this pressure singularity). The result is a finite contribution to the drag force that must be added to the result obtained by the surface pressure integration. This finite
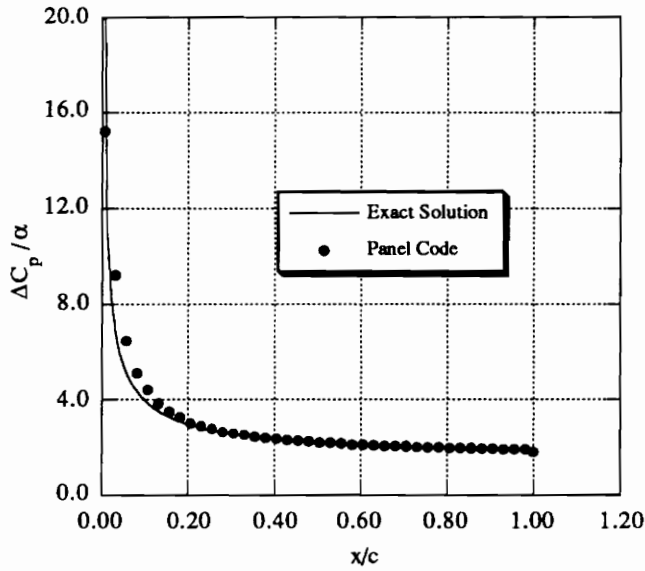
Fig. 4.8 — Pressure Distribution at 50% Semi-Span Location of Subsonic-LE Delta Wing of Fig. 4.7
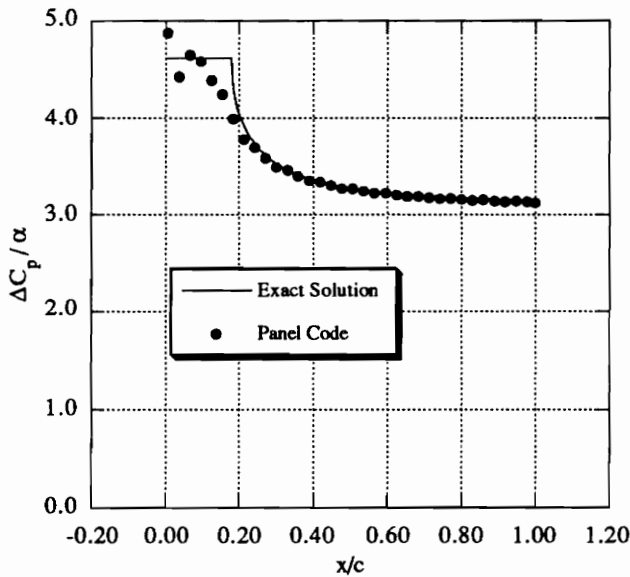
Fig. 4.9 — Pressure Distribution at 30% Semi-Span Location of Supersonic-LE Clipped-Delta Wing (see Fig. 4.7)

force is referred to as *leading-edge suction* (LES), and the component parallel to the drag force is known as the *leading-edge thrust* since it tends to reduce the overall
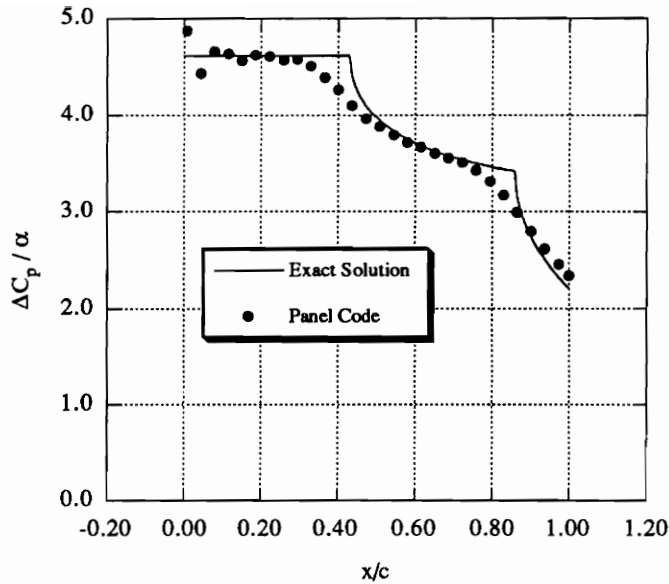
Fig. 4.10 — Pressure Distribution at 60% Semi-Span Location of Supersonic-LE Clipped-Delta Wing (see Fig. 4.7)

planform drag.

Thus, for flat thin wings at small angle of attack, the drag due to lift in coefficient form is given by

$$C_{D_i} = \alpha\, C_L - C_T, \tag{4.13}$$

where α is the angle of attack, C_L is the lift coefficient and C_T is the leading-edge thrust coefficient. Recalling that, for flat wings, $C_L = \alpha\, C_{L_\alpha}$ (where C_{L_α} is the lift-curve slope), Eq. (4.13) may be rewritten as

$$C_{D_i} = \left(\frac{1}{C_{L_\alpha}} - \frac{C_T}{C_L^2} \right) C_L^2. \tag{4.14a}$$

The parameters C_{L_α} and C_T/C_L^2 are not functions of C_L for a given planform and, thus, $1/C_{L_\alpha} - C_T/C_L^2$ completely determines $C_{D_i}(C_L)$. While this is true in linearized theory, Eq. (4.14a) is not generally applicable to actual wing planforms because the full theoretical values of leading-edge thrust are not observed experimentally. For this reason, a modified form of Eq. (4.14a) may be written as

$$C_{D_i} = \left(\frac{1}{C_{L_\alpha}} - k_T \frac{C_T}{C_L^2} \right) C_L^2, \tag{4.14b}$$

where k_T is a factor describing the fraction of C_T actually expected and has values between 0 and 1. The factor k_T depends on many variables; for example, it varies with flow Reynolds number, leading-edge radius and C_L. Carlson has examined this dependence in detail and in the present work, k_T is estimated using his "attainable leading-edge suction" method.[43] Fig. 4.11 shows the variation of k_T with lift for the baseline configuration.
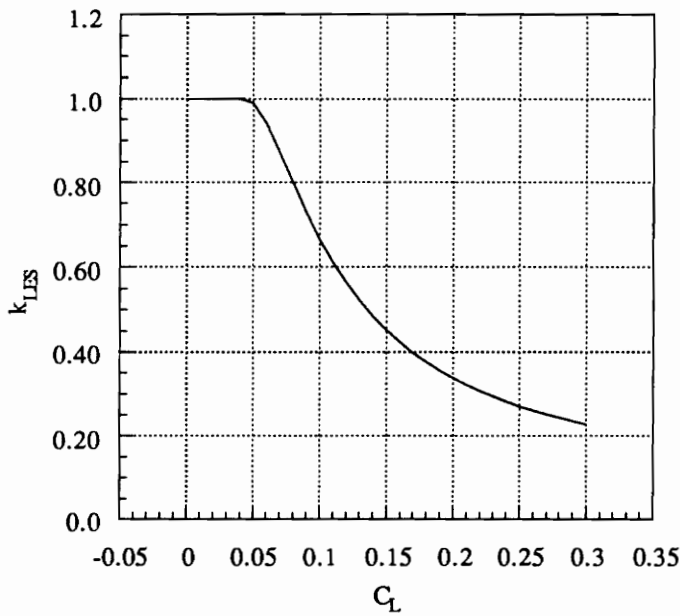
Fig. 4.11 — Variation of Attainable LES Factor, k_T, with Lift
for Baseline Configuration

The panel code developed from Refs. 41, 42, and 43 calculates C_L, k_T and C_T for a given value of α. It is, therefore, a simple matter to estimate C_{L_α} and C_T/C_L^2 for a given configuration.

4.1.3 — Supersonic Skin Friction Drag

The skin friction on the aircraft is estimated using standard algebraic estimates. The boundary layer is assumed to be turbulent and the van Driest II method is utilized to estimate the drag on flat plates with wetted area equal to that of the aircraft components. To account for the effects of body curvature, the resultant

drag estimates are multiplied by empirical form factors derived from the geometric characteristics of the aircraft components (*e.g.*, slenderness ratio is used to estimate the fuselage form factor). Finally, the individual component drags are summed to estimate the total friction drag on the aircraft.

Van Driest II Formulation. The van Driest II equation for the skin friction on a flat plate in compressible flow was developed assuming turbulent flow and a von Kármán mixing-length model. This method produces reasonably accurate results[45] from a relatively simple, closed-form expression.

From Ref. 46, the van Driest II formulation may be written as

$$\frac{0.242}{\sqrt{\bar{C}_F}} = \log_{10}(\bar{R}_e \bar{C}_F), \tag{4.15a}$$

where the equation terms are given by

$$
\begin{aligned}
\bar{R}_e &= \frac{F_\theta}{F_c} R_e, \\
F_\theta &= \sqrt{T_e/T_w} \left[\frac{1 + (122/T_w) \times 10^{-5/T_w}}{1 + (122/T_e) \times 10^{-5/T_e}} \right], \\
F_c &= \frac{rm}{\sigma^2}, \\
m &= \frac{\gamma - 1}{2} M^2, \\
\sigma &= \sin^{-1}\left(\frac{2a^2 - b}{\sqrt{4a^2 + b^2}} \right) + \sin^{-1}\left(\frac{b}{\sqrt{4a^2 + b^2}} \right), \\
a &= \sqrt{\frac{rm}{T_w/T_e}}, \text{ and} \\
b &= \frac{1 + rm}{T_w/T_e} - 1.
\end{aligned}
\tag{4.15b}
$$

In these expressions, M is the free-stream Mach number, R_e is the Reynolds number based on a given reference length, and T_w is the wall temperature. The wall is assumed to be adiabatic, thus $T_w = T_e(1 + rm)$, where the recovery factor $r = P_r^{1/3} \approx 0.88$ and the boundary layer edge temperature is assumed to be $T_e = 222\,K$ (an approximation to the atmospheric temperature found at typical aircraft cruise

altitudes). Finally, the ratio of specific heats is assumed to be $\gamma = 1.4$. Eq. (4.15) is solved numerically using Newton's method with an initial guess of $\bar{C}_F = 0.074/\bar{R}_e^{0.2}$.

The skin friction is given by $C_F = \bar{C}_F/F_c$. Thus the skin friction drag (per unit dynamic pressure) on one side of a flat plate of area A is simply given by $D_f/q = AC_F$.

Fuselage Skin Friction. The fuselage skin friction calculation takes place in 3 steps: first, the wetted area of the fuselage (less the region covered by the wing root) is calculated, second, the drag on a flat plate of equivalent area, $(C_F)_{eq}$, is calculated from Eq. (4.15), and finally, the drag multiplied by a form factor correction. That is,

$$\left(\frac{D_f}{q}\right)_{fuse} = f_{fuse}(S_{wet})_{fuse}(C_F)_{eq}. \tag{4.16}$$

The characteristic length used to calculate Reynolds number for the equivalent flat plate drag is the fuselage length. The form factor correction[47] is given by

$$f_{fuse} = 1 + 1.5 \left(\frac{d}{L}\right)_{fuse}^{1.5} + 7 \left(\frac{d}{L}\right)_{fuse}^{3}, \tag{4.17}$$

where d is the maximum fuselage depth and L is the fuselage length.

Wing Skin Friction. The wing skin friction is calculated in a similar manner, but the calculation is decomposed into multiple pieces. For a wing described at N spanwise stations in the Craidon geometry, there are $N - 1$ equivalent-flat-plate-drag calculations. That is, the wetted area between stations i and $i+1$ is calculated to form the equivalent flat plate area. The total wing drag is then given by

$$\left(\frac{D_f}{q}\right)_{wing} = f_{wing} \sum_{i=1}^{N-1} (S_{wet})_i (C_F)_{eq_i}. \tag{4.18}$$

The reference length used in Eq. (4.15) is the average chord length of the region of interest, $(c_i+c_{i+1})/2$. The form factor correction[47] accounting for thickness effects is given by

$$f_{wing} = 1 + 1.8 \left(\frac{t}{c}\right) + 50 \left(\frac{t}{c}\right)^4, \tag{4.19}$$

where t/c is the maximum wing thickness-to-chord ratio.

Engine Nacelle Skin Friction. The friction acting on the engine nacelles is calculated in a manner similar to the fuselage drag calculation. That is, the drag of a nacelle is given by

$$\left(\frac{D_f}{q}\right)_{nac} = f_{nac}(S_{wet})_{nac}(C_F)_{eq} . \tag{4.20}$$

Again, $C_{f_{eq}}$ is the drag acting on a flat plate of equivalent wetted area. The characteristic length used for estimating $C_{f_{eq}}$ is the nacelle length. The form factor correction is the same as for the fuselage,

$$f_{nac} = 1 + 1.5 \left(\frac{d}{L}\right)_{nac}^{1.5} + 7 \left(\frac{d}{L}\right)_{nac}^{3} . \tag{4.21}$$

Here, L is the nacelle length and d is the maximum nacelle diameter.

Control Surface Skin Friction. The drag acting on the control surfaces (*i.e.*, fins, canards and horizontal stabilizers) is estimated simply by calculating their wetted area and determining the equivalent-flat-plate drag,

$$\left(\frac{D_f}{q}\right)_{surf} = (S_{wet})_{surf}(C_F)_{eq} . \tag{4.22}$$

The control surfaces are assumed to be thin, thus no form factor correction is applied. Since the control surfaces are trapezoidal in the Craidon geometry description, the reference length used for the Reynold's number in Eq. (4.15) is the average of the root and tip chords, $(c_{root} + c_{tip})/2$.

The overall friction drag on the aircraft configuration is estimated by summing the individual component drags,

$$C_{D_f} = \frac{1}{S_w} \left[\left(\frac{D_f}{q}\right)_{fuse} + \left(\frac{D_f}{q}\right)_{wing} + \sum_{i=1}^{N_{nac}} \left(\frac{D_f}{q}\right)_{nac_i} + \sum_{i=1}^{N_{surf}} \left(\frac{D_f}{q}\right)_{surf_i} \right] , \tag{4.23}$$

where N_{nac} is the number of engine nacelles, N_{surf} is the number of control surfaces, and S_w is the reference wing area.

4.1.4 — Generation of the Drag Polar

Given the wave drag, the friction drag and the drag-due-to-lift characteristics of a configuration, a drag polar could be constructed as $C_D = C_{D_w} + C_{D_f} + (1/C_{L_\alpha} - k_T C_T/C_L^2)C_L^2$. However, this expression is only valid for flat wings and not for cambered wings. In this work, wing camber is not specified, but the effects of a proper camber design are estimated by an approximate technique. In the following, I describe the method developed to estimate the aircraft drag polar from the drag parameter calculations described in the previous sections.

Ideally, the drag due to lift of a wing would exhibit the full theoretical leading-edge thrust predicted by linearized potential theory. However, as was discussed in §4.1.2, this behavior is not observed experimentally and the actual fraction of theoretical leading-edge thrust is generally less than one. One strategy for designing wing camber is to replace the concentrated leading-edge suction force with distributed low pressures over the curved leading edge of a cambered wing, thus recovering the benefit of the theoretical flat-wing thrust. This strategy assumes a desired design lift coefficient, at which the cambered wing with the attainable leading-edge suction (LES) matches the drag polar of a flat wing with full LES. The camber design incurs a penalty for lift coefficients other than the design value, relative to the flat wing polar, giving rise to the term zero-lift *camber drag*. The simplified approach presented here models this strategy and its effects.

To reduce the terminology used, the drag-polar shape factor predicted by the full theoretical leading-edge thrust is denoted $K_{full} = (1/C_{L_\alpha} - C_T/C_L^2)$. Similarly, the shape factor predicted from the attainable LES method is given as $K_{att} = (1/C_{L_\alpha} - k_{att}C_T/C_L^2)$. The flat-wing zero-lift drag is composed of the configuration wave drag and friction drag, and the design lift coefficient is abbreviated C_{L_D}. The flat-wing, full LES drag polar is then given by

$$C_{D_{full}} = C_{D_w} + C_{D_f} + K_{full}C_L^2 . \qquad (4.24)$$

The cambered-wing drag polar has shape factor K_{att} and has vertex at (C_{L_m}, C_{D_m});

that is,

$$C_D = C_{D_m} + K_{att}(C_L - C_{L_m})^2 \, . \tag{4.25}$$

The constants C_{L_m} and C_{D_m} are determined by enforcing tangency of the two polars at the design lift coefficient, C_{L_D}. They are given by

$$
\begin{aligned}
C_{L_m} &= C_{L_D}\left(1 - \frac{K_{full}}{K_{att}}\right), \text{ and} \\
C_{D_m} &= C_{D_w} + C_{D_f} + K_{full}C_{L_D}^2 - K_{att}(C_{L_D} - C_{L_m})^2 \, .
\end{aligned}
\tag{4.26}
$$

An example of the two polars for the baseline configuration is shown in Fig. 4.12. For this figure, I used a calculated value of $k_{LES} = 0.427$ and $C_{L_D} = 0.1$. Both of these values are higher than those typically employed; they were used to increase the difference between the two polars. Note the ~ 0.0005 increment in zero-lift drag—the simulated effect of camber drag.
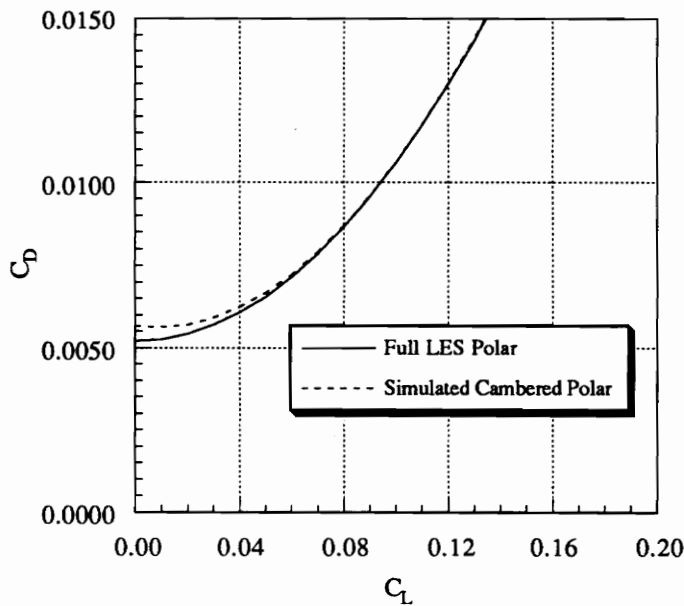
Fig. 4.12 — Flat-Wing Full LES and Approximate Cambered Drag Polars for Baseline Configuration

Using this method, the configuration's drag polar is defined by 6 parameters:

C_{D_w} the wave drag coefficient,

C_{D_f} the friction drag coefficient,

C_{L_α} the supersonic lift-curve slope

C_T/C_L^2 the supersonic leading-edge-thrust parameter,

k_T the attainable leading-edge thrust factor, and

C_{L_D} the design lift coefficient.

As was shown in Fig. 4.11, the attainable LES factor, k_T is a function of C_L and gives the approximate cambered-wing drag polar a non-parabolic shape. For the purposes of this study, however, I assumed a constant value of k_T for each design cycle in the optimization procedure. The value of k_T was that determined for the design at the beginning of a design cycle for an approximate cruise lift coefficient (typically, $0.05 \leq C_L \leq 0.1$). The design lift coefficient, C_{L_D} was selected at the beginning of the optimization and had a fixed value of $C_{L_D} = 0.05$. The remaining parameters—C_{D_w}, C_{D_f}, C_{L_α} and C_T/C_L^2—are determined from the aerodynamic analyses. This approach produces drag estimates that are accurate for typical cruise lift coefficients.

To evaluate the the above methods, it was desirable to compare with test data for a known configuration. Unfortunately, the baseline configuration for this study has not, as of this writing, been tested in a wind tunnel and there is no data available for comparison. However, the baseline configuration of Ref. 24 has been tested, and the above methods are assessed in Figs. 4.13 through 4.18.

For all of these polars, I used $C_{L_D} = 0.02$. For each of the Mach numbers shown, the agreement between the calculated and measured values of the drag is quite good for the typical range of cruise lift coefficients, $0 \leq C_L \leq 0.1$. The calculated drag polar underestimates the drag at the higher lift coefficients for all of the data shown. This is the expected tendency, since I assume a *fixed* value of the attainable LES factor, k_T, calculated at a low value of C_L. At the higher lift coefficients, the true value of k_T decreases (see Fig. 4.11) and the drag increases. Based on the agreement between the analytic results and the experimental data,
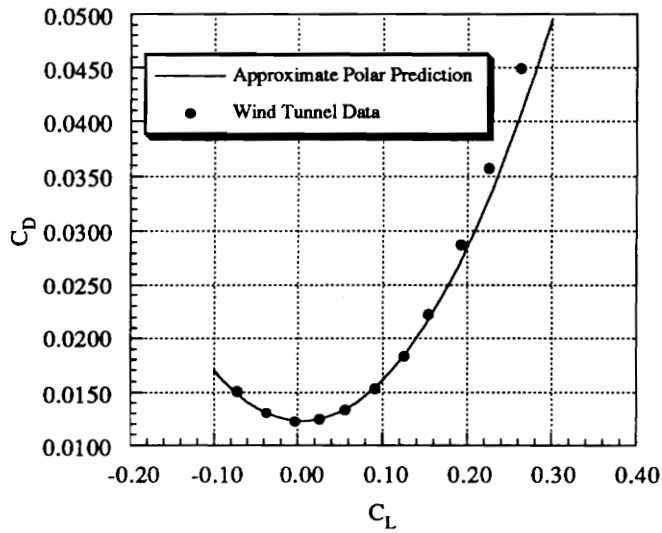
Fig. 4.13 — Comparison of Approximate Cambered Polar and Wind Tunnel Data for Baseline Configuration of Ref. 24 ($M = 1.6$)
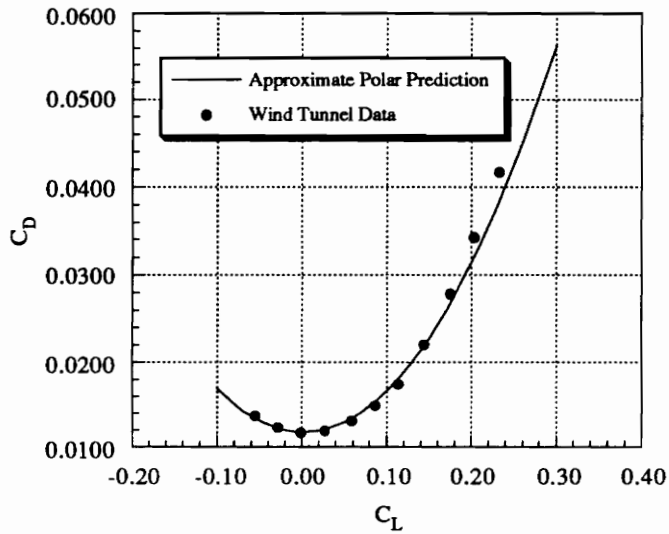
Fig. 4.14 — Comparison of Approximate Cambered Polar and Wind Tunnel Data for Baseline Configuration of Ref. 24 ($M = 2.0$)
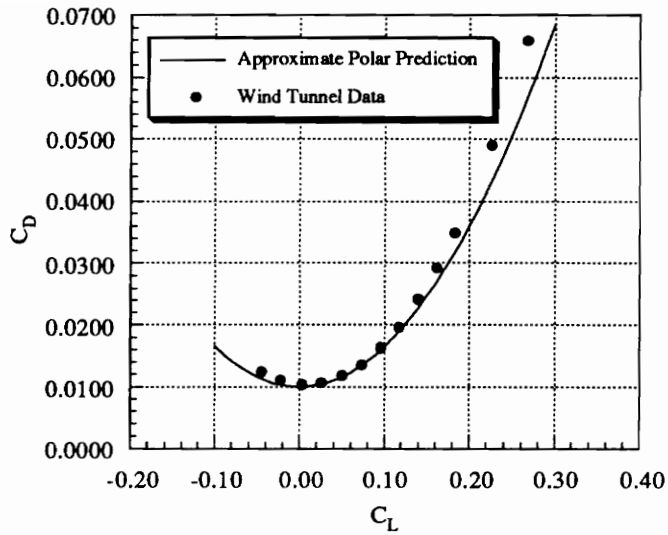
Fig. 4.15 — Comparison of Approximate Cambered Polar and Wind Tunnel Data for Baseline Configuration of Ref. 24 ($M = 2.8$)
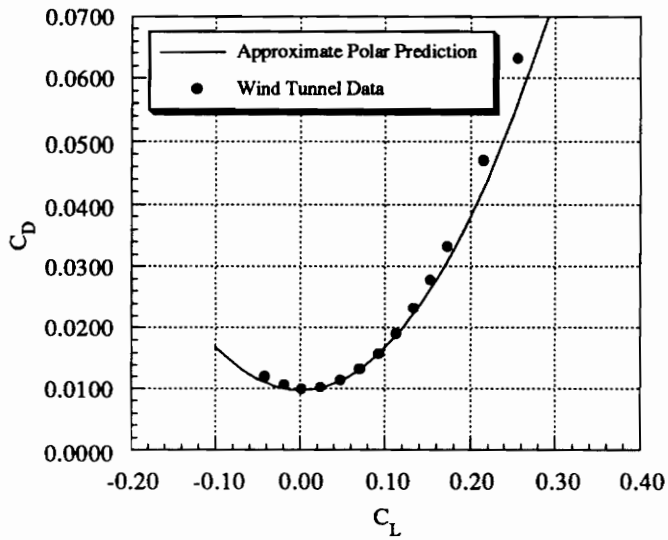
Fig. 4.16 — Comparison of Approximate Cambered Polar and Wind Tunnel Data for Baseline Configuration of Ref. 24 ($M = 3.0$)
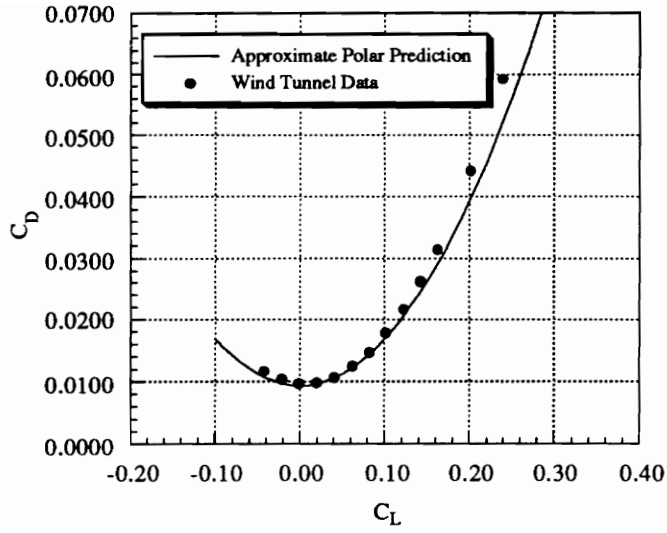
Fig. 4.17 — Comparison of Approximate Cambered Polar and Wind Tunnel Data for Baseline Configuration of Ref. 24 ($M = 3.2$)
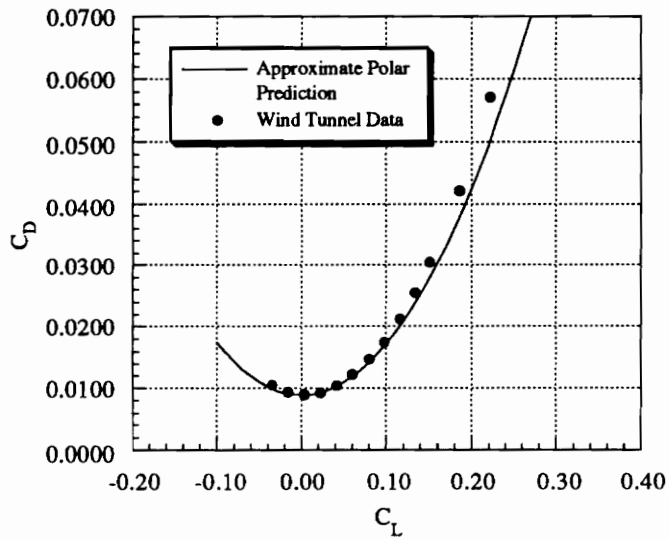
Fig. 4.18 — Comparison of Approximate Cambered Polar and Wind Tunnel Data for Baseline Configuration of Ref. 24 ($M = 3.6$)

this method of generating a drag polar for use in the range calculation appears to be sufficient for the low values of C_L encountered in cruise.

4.1.5 — Low-Speed Lift

As stated previously, the low-aspect-ratio configurations required for efficient supersonic flight have such low values of the subsonic lift-curve slope that considerable effort in a traditional design process must be directed towards limiting the angle of attack at landing to prevent tail scrape. In the context and terminology of design optimization, the landing angle-of-attack constraint is usually active. Thus, the optimizer works hard to take advantage of any gain possible in this constraint and, therefore, the calculation of landing angle must be both robust and accurate.

The information required to estimate landing angle is the variation of lift with angle of attack, $C_L(\alpha)$. A method has been devised to define $C_L(\alpha)$ in a manner analogous to the drag polar calculation described in the previous section. That is, the overall behavior of $C_L(\alpha)$ is estimated based on the calculation of the *subsonic* lift-curve slope at $C_L = 0$, C_{L_α} (not to be confused with the supersonic lift-curve slope used to estimate drag due to lift). In the following discussion, I describe the methods used to define subsonic $C_L(\alpha)$, and then describe an approximate method used to estimate the influence of ground effect.

The low values of the lift-curve slope for these planforms would be a formidable obstacle in the design were it not for the ameliorating effect of vortex lift. The Concorde, for example, is only viable because it was designed to exploit vortex lift for landing.[48] The separation of flow along the leading edge of highly swept wings and the resulting spiral vortex adds significantly to the lift predicted by potential flow methods alone. The most widely used method of accounting for this effect is the Polhamus leading-edge-suction analogy.[49] Polhamus defines an expression which incorporates potential and vortex flow terms,

$$C_L = K_p \sin \alpha \cos^2 \alpha + K_v \sin^2 \alpha \cos \alpha \,, \tag{4.27}$$

where K_p is the normal force slope given by potential-flow lifting-surface theory,

K_v is a parameter accounting for vortex lift, and α is the angle of attack. I assume that K_p is given accurately by the lift-curve slope, C_{L_α}.

The analysis model used to estimate C_{L_α} is a vortex lattice method (VLM).[50] The VLM represents the aircraft wing by a collection of horseshoe vortices of strength $_i$ on the wing's camber surface. The velocity induced by each vortex element is determined from the Biot-Savart Law assuming a flat wake. The flow over the wing is calculated by enforcing flow tangency on selected *control points* on the wing, with the number of control points equal to the number of horseshoe vortices. The bound vortex is located at the panel quarter chord and the control point at the panel three-quarter chord. The vortex strengths are calculated from the following system of linear equations,

$$[\mathbf{A}]\{\Gamma\} = \{V_c\},\tag{4.28}$$

where $[\mathbf{A}]$ is an aerodynamic *influence matrix* determined by the problem geometry, $\{\Gamma\}$ is the vector of unknown vortex strengths, and $\{V_c\}$ are the required flow velocities at the control points. Upon solving Eq. (4.28) for $\{\Gamma\}$, the total lift on the wing, L, is given by the Kutta-Joukowski theorem,

$$L = \rho_\infty U_\infty \sum_{i=1}^{N_v} \Gamma_i \Delta y_i,\tag{4.29}$$

where N_v is the number of vortex panels used in the problem and Δy_i is the spanwise width of panel i. For a more complete discussion of the VLM , see Ref. 50. In the work presented here, only the flow over the wing is calculated and the wing is assumed to be flat.

The lift-curve slope, C_{L_α}, is calculated by a forward difference. Since the wing is assumed to be flat, this step requires only one flow evaluation and, given the linear flow assumption of the VLM, produces the exact value of C_{L_α}. Typically, the wing is represented by 105 panels on each half of the wing, with 15 panels in the spanwise direction and 7 panels in the chordwise direction.

For the vortex term in Eq. (4.27), a version of the Polhamus suction analogy is employed.[49] Polhamus presents the following expression for delta-wing planforms:

$$K_v = \left(\frac{\partial C_T}{\partial \alpha^2}\right) \frac{1}{\cos \Lambda_{LE}}$$

where C_T is the leading-edge thrust coefficient from the potential-flow solution, and Λ_{LE} is the delta wing's leading-edge sweep angle. The situation for wings of arbitrary planform is complicated by non-constant Λ_{LE}; hence, this equation does not strictly apply. It's simplicity, however, led to the development of an approximation for wings of arbitrary planform that has proven quite satisfactory.

To approximate the $\cos \Lambda_{LE}$ term in the equation, an area-weighted average is used to form an *equivalent* term,

$$(\cos \Lambda_{LE})_{eq} = \frac{2}{S_w} \sum_{i=1}^{N} c_i \frac{\Delta y_i^2}{\sqrt{\Delta y_i^2 + \Delta x_{LE_i}^2}}, \tag{4.30}$$

where N is the number of spanwise stations used to describe the wing in the Craidon geometry, c_i is the wing chord at station i, Δy_i is the spanwise distance between adjacent stations, Δx_{LE_i} is the difference in x-location of the leading edge at adjacent stations, and S_w is the wing area.

A simple expression for $\partial C_T / \partial \alpha^2$ may be derived using results from linearized-potential theory. The induced drag C_{D_i} of a wing in subsonic flow, as for supersonic flow, may be expressed as

$$C_{D_i} = \left(\frac{1}{C_{L_\alpha}} - \frac{C_T}{C_L^2}\right) C_L^2 \equiv \frac{C_L^2}{\pi e A},$$

where e is the span efficiency and A is the wing aspect ratio. Solving for C_T and recalling that the lift coefficient in linearized flow for a flat wing is given by $C_L = \alpha C_{L_\alpha}$ produces,

$$C_T = \alpha^2 \left(C_{L_\alpha} - \frac{C_{L_\alpha}}{\pi e A}\right)$$

and

$$\frac{\partial C_T}{\partial \alpha^2} = C_{L_\alpha} - \frac{C_{L_\alpha}}{\pi e A}.$$

Thus, an expression for K_v is given by

$$K_v = \left(C_{L_\alpha} - \frac{C_{L_\alpha}}{\pi e A} \right) \frac{1}{(\cos \Lambda_{LE})_{eq}}, \qquad (4.31)$$

which depends only on the value of C_{L_α} estimated by the VLM code and easily determined planform parameters. The span efficiency, e, could be determined from the VLM code as well, but it was found that a constant value of $e = 0.8$ produces results consistent a more detailed analysis (see below).

These values of K_p and K_v are then used in Eq. (4.27) to produce $C_L(\alpha)$. To summarize, the subsonic behavior of $C_L(\alpha)$, including non-linear vortex effects, is determined by a single VLM flow solution to produce the parameter C_{L_α}, and simply determined geometric quantities.

To check the validity of the above procedure, the results predicted by this method were compared with those produced by Lamar's VLM program.[51] This program includes a detailed calculation of the leading-edge-suction analogy for vortex separation. Fig. 4.19 compares the $C_L(\alpha)$ behavior predicted by the above procedure, and that estimated by Lamar's program for the baseline configuration. As can be seen, the agreement is quite favorable, particularly for the angles of attack of interest for the calculation of landing performance ($\alpha \leq 20°$).

In addition to the effects of vortex lift, the influence of ground effect can play an important role in the behavior of $C_L(\alpha)$ in the landing phase of flight. An empirical method due to Küchemann[52] accounts for ground effect by reducing the angle of attack necessary to produce a given C_L. This angle of attack decrement, $\Delta\alpha$, is given by

$$\Delta\alpha = \frac{0.09 C_L}{\pi A} \left(\frac{b}{h} \right)^{1.4}, \qquad (4.32)$$

where A is the wing's aspect ratio, b is the span and h is the height above the ground. For the work presented here, $h = 75$ ft. Fig. 4.20 illustrates the influence of ground effect by comparing $C_L(\alpha)$ calculated with and without the contribution of Eq. (4.32) for the baseline configuration.
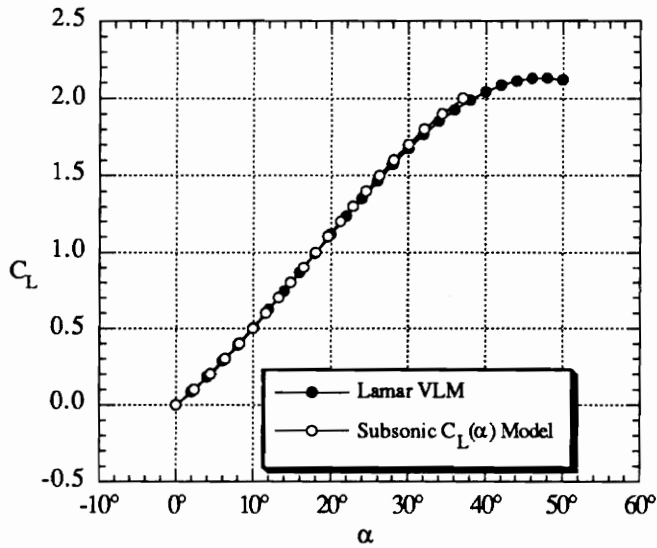
Fig. 4.19 — Comparison of $C_L(\alpha)$ Estimation Method with Lamar's VLM Code for Baseline Configuration
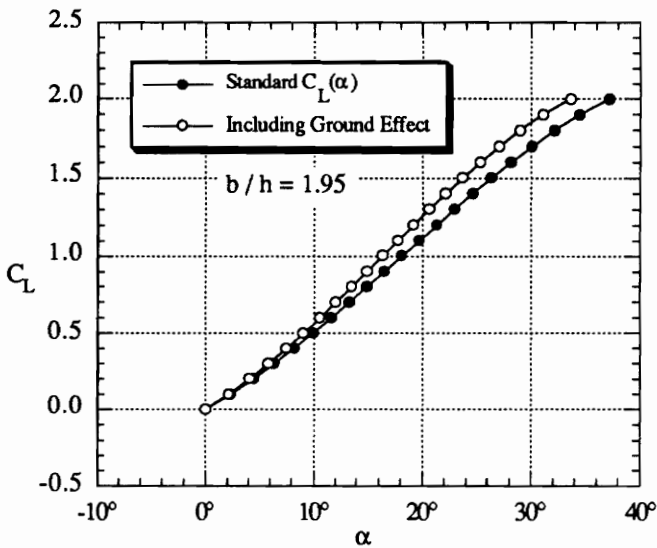
Fig. 4.20 — The Influence of Ground Effect on $C_L(\alpha)$ for the Baseline Configuration

To summarize, the aerodynamic estimation methods are driven by the requirements of the mission analysis; namely, the supersonic drag polar and the subsonic lift curve. The methods used to derive the polar and lift curve rely principally on the following key aerodynamic parameters:

C_{D_w} the wave drag coefficient,

C_{D_f} the friction drag coefficient,

$(C_{L_\alpha})_{sup}$ the supersonic lift-curve slope,

C_T/C_L^2 the supersonic leading-edge-thrust parameter,

$(C_{L_\alpha})_{sub}$ the subsonic lift-curve slope.

Recall that the attainable LES parameter k_{LES} is calculated at the beginning of a design cycle and held constant, and that the design lift coefficient C_{L_D} is fixed for the design. Finally, several geometric parameters (*e.g.,* aspect ratio, average leading-edge sweep) are also required for the calculations, but the computational effort required to estimate these is negligible.

4.2 — Performance Analysis Methods

The two basic flight characteristics of interest, range and landing angle of attack, depend on the drag polar and lift curve generated by the aerodynamic analysis. The range and landing-angle calculations will be described separately.

4.2.1 — Range Calculation

The aircraft range is calculated at the cruise Mach number ($M = 2.4$ for this work) for the available mission fuel. I assume that 85% of the mission fuel is used in cruise, with the remaining 15% held as reserve. This figure was selected as an approximate representation of the fuel consumed during the cruise leg of a more detailed definition of this aircraft's flight profile. As mentioned previously, the assumed mission is a very simple one; the mission begins at an initial altitude (takeoff and climb to this altitude are ignored), followed by a linear cruise-climb to the final altitude.

The initial altitude and the climb rate are specified by design variables. As

noted in Ch. 3, one of the formulation constraints is the maximum allowable cruise altitude, h_{max}. The altitude h is given by

$$h = \begin{cases} h_0 + \dot{h}t, & \text{if } h \le h_{max} \\ h_{max}, & \text{otherwise,} \end{cases}$$

where $\dot{h}$ is the cruise-climb rate and t is time; for this work, $h_{max} = 70,000 \, ft$. Two basic profiles are possible using this definition, as shown in Fig. 4.21, depending on the values of the initial altitude and climb rate.
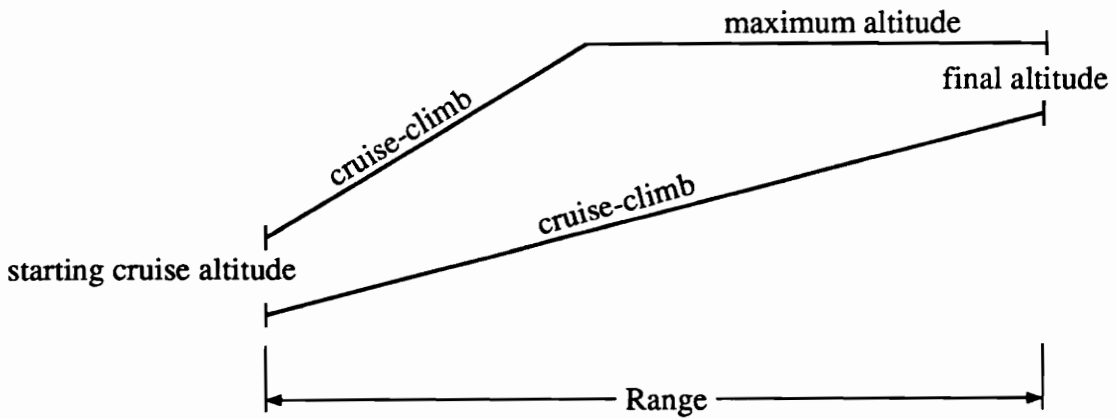
Fig. 4.21 — Cruise Profile Possibilities

The range, R, is calculated using

$$R = \int_{W_1}^{W_0} \frac{V \, dW}{\left(D + W\dot{h}/V\right) S_f}, \tag{4.33}$$

where W is the aircraft weight, V is its velocity, and D is the drag. The terms W_0 and W_1 represent the weight of the aircraft at the beginning and end of cruise, respectively. The $W\dot{h}/V$ term accounts for the additional engine thrust required to obtain the desired cruise-climb rate. For typical values of the lift-to-drag ratio and cruise-climb rate (see Ch. 6), this term increases required engine thrust by 5–7%.

Given the assumption on the mission profile, W_0 is the gross weight and $W_1 = W_0 - 0.85W_{fuel}$. The thrust specific fuel consumption, S_f, is the rate of weight

decrease (normalized by the thrust, T) and, thus, the time t (used to calculate altitude) is given by

$$t = \int_W^{W_0} \frac{dW}{TS_f}.$$

A constant value of $S_f = 1.3\,lb/lb \cdot s$ is assumed—a value taken from the baseline's engine data for typical cruise conditions.

The velocity is given by $V = Ma_\infty$, where a_∞, the local speed of sound, is given by the U.S. Standard Atmosphere (see Ref. 33) and is a function only of the altitude. The drag is given by $D = 1/2\rho_\infty V^2 S_w C_D$, where the air density ρ_∞ is also defined by the U.S. Standard Atmosphere. The drag coefficient, C_D, is determined from Eq. (4.25) with $C_L = W/(1/2\rho_\infty V^2 S_w)$. In practice, Eq.(4.33) is integrated numerically using about 10 intervals.

4.2.2 — Landing Angle of Attack Calculation

The calculation of landing angle of attack begins with the estimation of the landing lift coefficient, given by Eq. (3.6), at the emergency condition defined in §3.4. Given this value of C_L, the angle of attack α is determined by solving Eq. (4.27) numerically. Newton's method was employed, and the solution is typically found in about 5 iterations. The initial guess for the calculation is $\alpha = \left(-K_p + \sqrt{K_p^2 + 4K_v C_L}\right)/(2K_v)$, the solution to the quadratic expression derived from Eq. (4.27) by expanding for small α.

If the influence of ground effect is to be included, the angle of attack is given by $\alpha_{GE} = \alpha - \Delta\alpha$, where α is the angle determined by the above iterative procedure and $\Delta\alpha$ is given by Eq. (4.32). For all the results presented here, ground effect was included.

In the previous chapter, it was shown that the range calculation depends upon the estimation of 4 key aerodynamic parameters: the supersonic wave drag, C_{D_w}, the supersonic friction drag, C_{D_f}, the supersonic lift-curve slope, $(C_{L_\alpha})_{sup}$ and the leading-edge-thrust parameter, C_T/C_L^2. Similarly, the landing angle-of-attack calculation depends principally upon the estimation of the subsonic lift-curve slope, $(C_{L_\alpha})_{sub}$.

The estimation of each of these paramaters is the function of the detailed analysis methods used in this work. The approximate CPU times required to calculate them are shown in Table 5.1. Note that supersonic C_{L_α} and C_T/C_L^2 are grouped together, since only one run of the supersonic panel code is required to estimate both. Note also that the time required to calculate skin friction drag, C_{D_f}, is less than 1/20 of that required for the next fastest analysis.

Table 5.1. CPU Times (Silicon Graphics 4D/340 VGX Workstation)

for Detailed Analyses

Parameter	CPU Time (sec)
C_{D_w}	4.41
C_{D_f}	0.06
$(C_{L_\alpha}, C_T/CL^2)_{sup}$	1.69
$(C_{L_\alpha})_{sub}$	1.23

Although these computational times are quite reasonable, the numerical optimization procedure requires many hundreds of constraint evaluations, and thus the computational cost rapidly increases. Furthermore, one of the research goals of this project has been to explore methods for coupling simple and detailed analysis models through the variable-complexity approach. The analysis methods used in this work are preliminary-design-level techniques, but in the future it would be desirable to incorporate detailed-design-level methods such as Euler or Navier-Stokes

analysis. For such advanced analysis tools, the CPU times required to evaluate the aircraft performance would increase several orders of magnitude, and the variable-complexity strategy would be a necessity for design optimization. For these reasons, the variable-complexity approach was investigated for the estimation of C_{D_w}, $(C_{L_\alpha})_{sup}$, C_T/C_L^2, and $(C_{L_\alpha})_{sub}$. Since the calculation of C_{D_f} is so inexpensive relative to the other analyses, and since the calculation is quite straightforward already, there was no investigation into further approximation for C_{D_f}.

Recall that there are two aspects to the variable-complexity strategy employed in this work: the first couples simple and detailed analysis parameters using the methods of §3.1 to reduce the cost of the aerodynamic analyses, and the second utilizes a simple weight estimation method to represent the influence of structural considerations on the aircraft design. In this chapter, I first describe the simple models developed to estimate the aerodynamic performance parameters, and then discuss the weight estimation model.

5.1 — Simple Wave-Drag Model

One of the challenges faced in this research project was the development of a simple wave-drag model that successfully captured the interacting influence of the geometries of the wings, fuselage and nacelles. A model based on classical wave-drag theory which utilizes an approximate supersonic area-ruling technique has been developed. Although the absolute drag values predicted by the model are not especially accurate, it does predict trends for differing designs accurately. Since the simple model results are combined with the detailed model (*i.e.*, the Harris code) results in the approximations used in the optimization, only the trend (*i.e.*, derivatives) estimation accuracy is critical.

Recall from Ch. 4 that Eqs.(4.6) and (4.7) relate the supersonic wave drag of an axi-symmetric body to its cross-sectional area distribution, and that the supersonic area rule relates an aircraft to a family of *equivalent* axi-symmetric bodies. The supersonic area rule determines the equivalent-body area distributions by passing

a series of inclined, parallel cutting planes through the aircraft configuration. The area of the equivalent body at each station is the projection onto a plane normal to the aircraft axis of the area intercepted by the cutting plane.

The computational cost of evaluating the wave drag of each equivalent body is small compared to that required to determine the area distribution of the equivalent bodies. Consequently, there is no approximation to the drag evaluation method, but only to the supersonic area rule, which determines the equivalent areas.

The aircraft's wave drag is assumed to be governed principally by the cross-sectional area distribution of the fuselage, wing and engine nacelles, and by the relative location of each of these components. There are two steps to the approximate area rule: first, a simplified representation of the aircraft geometry is generated and, second, the intersection of the Mach cutting planes with this simplified representation is approximated.

To represent the aircraft, the fuselage, wing and engine nacelles are replaced by a collection of *representative* axi-symmetric bodies. These representative bodies are not to be confused with the wave-drag equivalent bodies; they serve only to approximate the aircraft configuration's volumetric distribution. These representative bodies are related to the actual aircraft components by cross-sectional area or volumetric requirements. Many more data points are required than are stored in the Craidon geometry description to estimate the equivalent-body area distributions of the approximate area rule. Thus, to avoid repetitive interpolation, it is advantageous to define the area distribution of each representative body as a function of the axial location (*e.g.*, a cubic spline).

Each of the engine nacelles is modeled by a representative body. I calculate the axial area distribution (subtracting out the capture area of the inlet) of the nacelle and spline the data as a function of the x-location. Each body representing a nacelle is located in the same position as the nacelle it models.

The fuselage is modeled by a single body of revolution. The cross-sectional

area of the fuselage is calculated and splined to form the representative body. As discussed previously, in this study the fuselage is axi-symmetric and is already defined analytically by the design variables. Although for this particular case, it is redundant to redefine the fuselage as a splined body, this approach isolates the approximate analysis method from the geometry definition and is, therefore, more generally applicable.

The wing is not represented by a single body, but by a collection of bodies of specified volume. In the Craidon description of the aircraft, the wing is defined at a number of spanwise locations where the airfoil cross-sections are prescribed. One representative body is constructed for each region *between* these consecutive spanwise wing section locations. Since I attempt to model the volumetric distribution of the wing, each representative body is a Sears-Haack body,[35] a minimum wave-drag body of revolution with given volume and length, with volume equal to that between consecutive wing-section locations. Each body has length given by the average of the length of the consecutive wing sections, and the nose of each representative body is positioned at the average leading-edge location of the consecutive wing sections.

Thus the aircraft geometry is approximated by a collection of representative bodies whose cross-sectional areas are known functions of the axial station. Fig. 5.1 illustrates an actual configuration and the collection of bodies representing it.

Even with this simplified representation, the calculation of the area intercepted by the inclined Mach cutting planes would be somewhat involved. It is here that the second step of the approximate area rule comes into play. I assume that the normal projection of the intercepted area on a representative body may be approximated by the body's *cross-sectional* area at the location where the cutting plane passes through its axis. Since this assumption eliminates the intercepted area calculation, there is a significant computational savings. The actual normal projected area for one such body and the approximation to it is illustrated in Fig. 5.2.
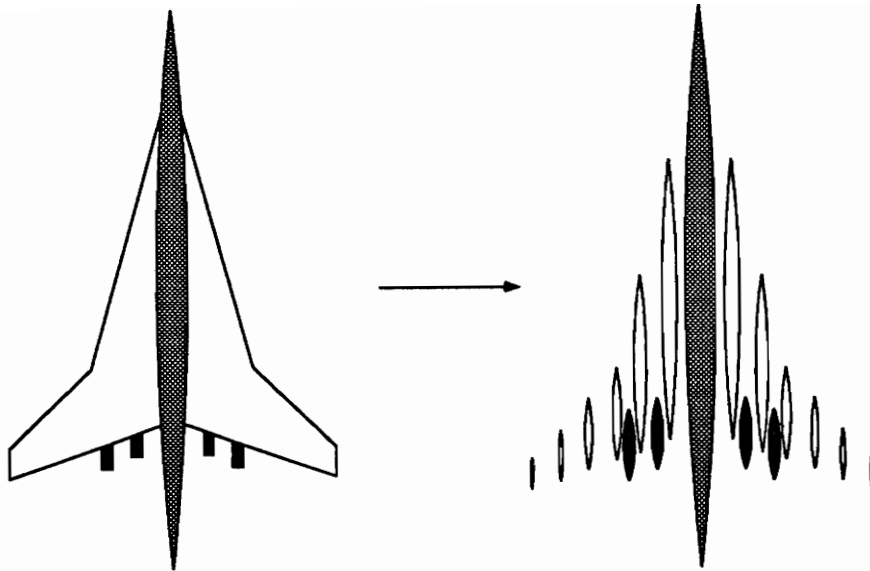
Fig. 5.1 — Aircraft and Collection of Representative Bodies

Given these two steps, the generation of the wave-drag equivalent bodies necessary to evaluate the aircraft's wave drag is straightforward. The area of the wave-drag equivalent body at a given x-station is determined by the sum of the cross-sectional areas of the bodies intercepted by the Mach cutting plane. Each of these cross-sectional areas is calculated for the axial station where the Mach cutting plane passes through the axis of the body. Since these areas are given by analytic functions of x, this summation is computationally inexpensive.

One measure of the success of the approximate area rule is to compare the equivalent body area distributions produced by the Harris code and the simple model at different cutting-plane roll angles. Figs. 5.3, 5.4, and 5.5 compare the area distributions generated from the baseline configuration with $M = 2.4$ at $\theta = -90°$, $\theta = 0°$, and $\theta = 90°$, respectively. As these figures illustrate, the approximate area-rule method captures the basic interrelation between aircraft components that forms the equivalent-body distribution.

Actual Normal Projected Area
(non-circular)

Inclined Mach Cutting Plane

Approximate Normal Projected Area
(circular)

Inclined Mach Cutting Plane
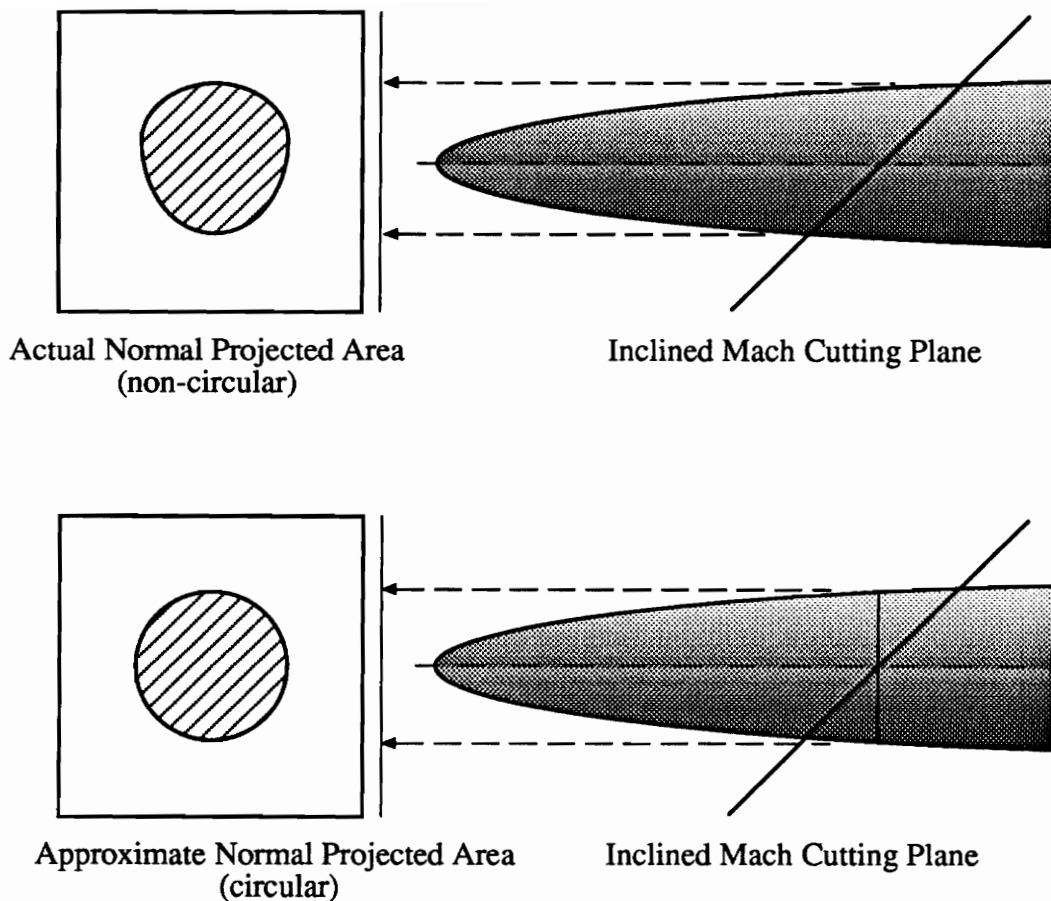
Fig. 5.2 — Actual and Approximate Normal-Area Projections
of Intersection of Mach Cutting Planes with Representative Body

A second measure of the simple model's performance is its ability to capture wave-drag variation with the cutting-plane roll angle. Fig. 5.6 compares the wave drag, D_w/q, variation with the roll angle, θ, produced by the Harris code and the simple model. Again, the simple model captures much of the behavior of the detailed analysis.

The most important evaluation for design purposes is the comparison of the models' performance over a broad range in the aircraft design. Fig. 5.7 compares the wave drag estimated by the two models for a number of different designs. Using

Fig. 5.3 — Equivalent Body Area Distributions for $\theta = -90°$ Generated by Harris Code and Simple Wave-Drag Model ($M = 2.4$)

the parametric models described in Ch. 2, the configuration is defined using a vector of design variables, $\mathbf{x}$. The wave drag data was calculated at different values of $\mathbf{x}$, varied between the two points $\mathbf{x}_0$ and $\mathbf{x}_1$ in the design space ($\mathbf{x}_0$ and $\mathbf{x}_1$ correspond respectively to the initial design and one final design, WFN_{m12}, described in the next chapter) as a function of the relative design change parameter ξ in the expression

$$\mathbf{x} = \mathbf{x}_0 + \xi(\mathbf{x}_1 - \mathbf{x}_0), \quad 0 \le \xi \le 1. \tag{5.1}$$

Although the magnitude of the simple wave-drag estimate is quite different from the Harris program results, the simple model displays similar trends over a large range of design. Since the simple model is used in a variable-complexity approach (see Ch. 3), only the derivatives of the wave drag are important.

Recall from Ch. 3 that three approximation methods are available for use during the optimization procedure: scaled, linear, and global-local approximations. These three approximation models are compared with the Harris code results in Fig. 5.8.
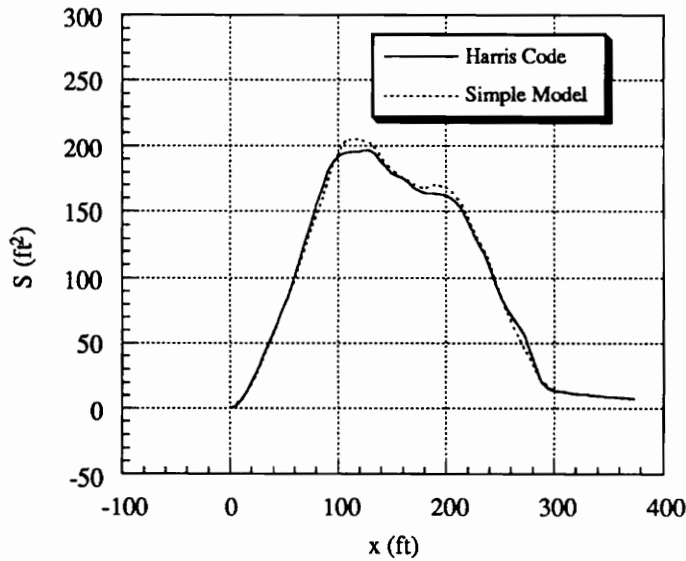
Fig. 5.4 — Equivalent Body Area Distributions for $\theta = 0°$ Generated by Harris Code and Simple Wave-Drag Model ($M = 2.4$)

The results are again presented as a function of the design change parameter ξ. Note that the two variable-complexity approximate models (*i.e.*, the scaled and global-local approximations) predict the wave drag more accurately over the design change than does the linear approximation.

5.2 — Simple Drag-Due-to-Lift Model

In Ch. 4, the methodology for estimating the drag due to lift of thin wings was described, and it was shown how the calculation could be reduced to the estimation of the parameters C_{L_α} and C_T/C_L^2. For the simple drag-due-to-lift model, I have turned to the results of Ref. 53, where analytical expressions for wings with cranked leading edges are presented. In the following sections, I describe the closed-form solution available for wings of this particular planform, outline the method used to relate a general wing planform to this type of wing, and finally present some results comparing the simple model with the panel code predictions.

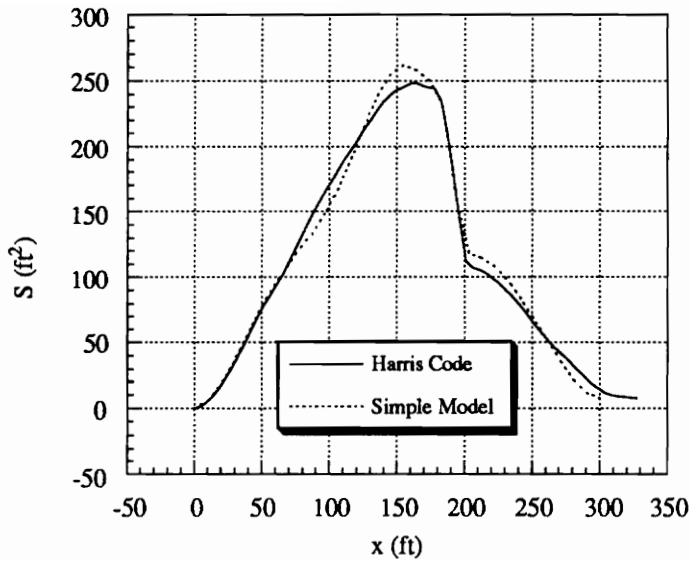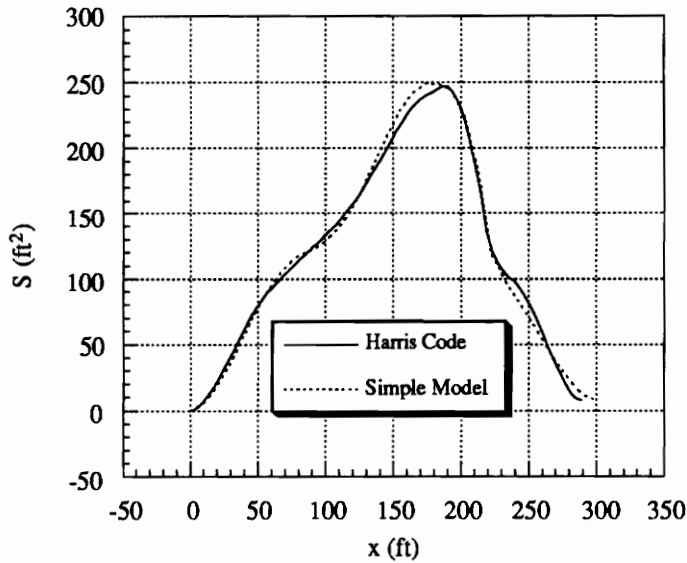**Fig. 5.5** — Equivalent Body Area Distributions for $\theta = 90°$ Generated by Harris Code and Simple Wave-Drag Model ($M = 2.4$)

5.2.1 — Analytic Solutions

For wings of the planform shown in Fig. 5.9, Cohen and Friedman[53] develop analytic expressions similar to the following for C_{L_α} and C_T/C_L^2,

$$C_{L_\alpha} = \frac{4}{\beta S_w}\left(\beta\frac{m_2 - m_1}{m_2 + m_1}\frac{s_1^2}{E\left(\pi/2, k\right)}\left\{\frac{\pi}{2}\left[1 + \Lambda_0\left(\phi, k\right)\right]\sqrt{\frac{m_2^2 - 1}{m_2^2 - m_1^2}} + \frac{1}{m_2}\left[\frac{m_2^2}{m_1^2}E\left(\pi/2, k\right) - K\left(\pi/2, k\right)\right]\right\} + \frac{m_2 c_0^2}{\beta} - \frac{2c_0 c_1}{\beta}\left(m_2 - m_1\right) - \frac{m_2}{\beta}\left(c_0 - c_2\right)^2\sqrt{\frac{m_2}{m_2 - 1}}\right),$$

(5.2)

and

$$\frac{C_T}{C_T^2} = \frac{\pi}{S_w}\left[\frac{s_1}{C_{L_\alpha}E\left(\pi/2, k\right)}\right]^2\sqrt{1 - m_1^2},$$

(5.3)

where $\beta = \sqrt{M_\infty^2 - 1}$, and S_w is the wing area. The parameters m_1 and m_2 are given by $m_1 = \beta s_1/c_1$ and $m_2 = \beta\left(s - s_1\right)/\left(c_2 - c_1\right)$. The geometric parameters
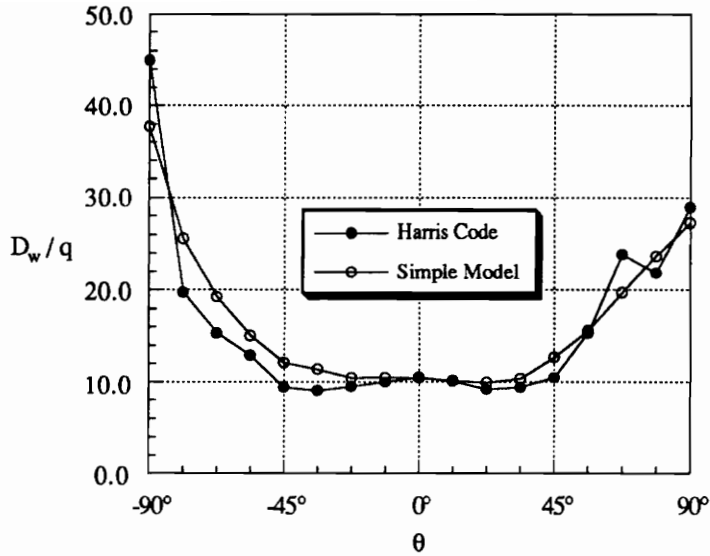
Fig. 5.6 — Comparison of Wave-Drag Variation in Cutting-Plane Roll Angle Predicted by the Harris Code and the Simple Wave-Drag Model

c_0, c_1, c_2, s_1 and s are defined in Fig. 5.9. The functions $K(\phi, k)$ and $E(\phi, k)$ are the elliptic integrals of the first and second kind, respectively, with $k = \sqrt{1 - m_1^2}$. The function $\Lambda_0(\phi, k)$ is also an elliptic function, given by

$$\Lambda_0(\phi, k) = \frac{2}{\pi} \left\{ K\left(\pi/2, k\right) E\left(\phi, m_1\right) - \left[K\left(\pi/2, k\right) - E\left(\pi/2, k\right)\right] K\left(\phi, m_1\right) \right\},$$

where $\phi = \sin^{-1}(1/m_2)$. Note that the expression reported in Ref. 53 for C_{L_α} is incorrect with all the β terms omitted except for that appearing in the $4/\beta S_w$ term. The correct placement of the β terms in Eq. (5.2) has been determined by a careful examination of the equation for limiting values of m_1, m_2, c_1 and c_2 where the solution approached those known for simpler planforms.

Eqs. (5.2) and (5.3) are exact solutions which depend on several assumptions: the inboard portion of the leading edge is subsonic (*i.e.*, $m_1 < 1$), the outboard portion is supersonic (*i.e.*, $m_2 > 1$), the Mach line from the apex of the wing passes through the trailing edge of the wing and, finally, that the trailing edge is unswept.
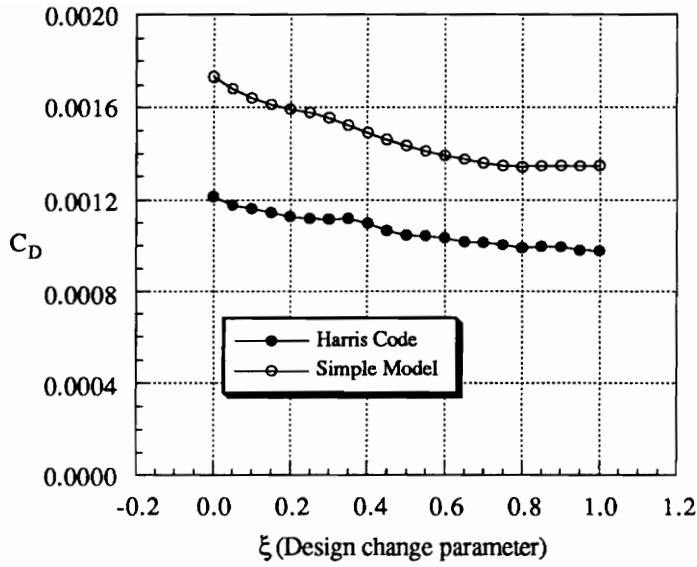
Fig. 5.7 — Simple Wave-Drag Model Predictions, from Intitial Design to WFN_{m12} Design
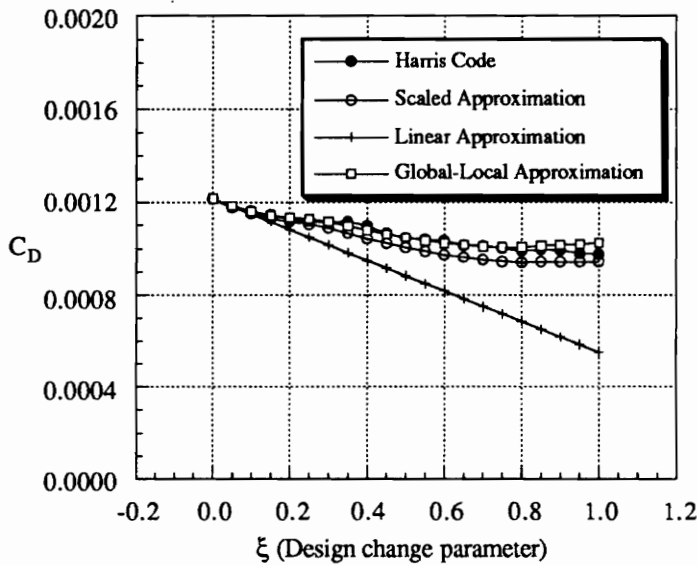
Fig. 5.8 — Wave-Drag Predictions for Three Approximation Methods, from Intitial Design to WFN_{m12} Design
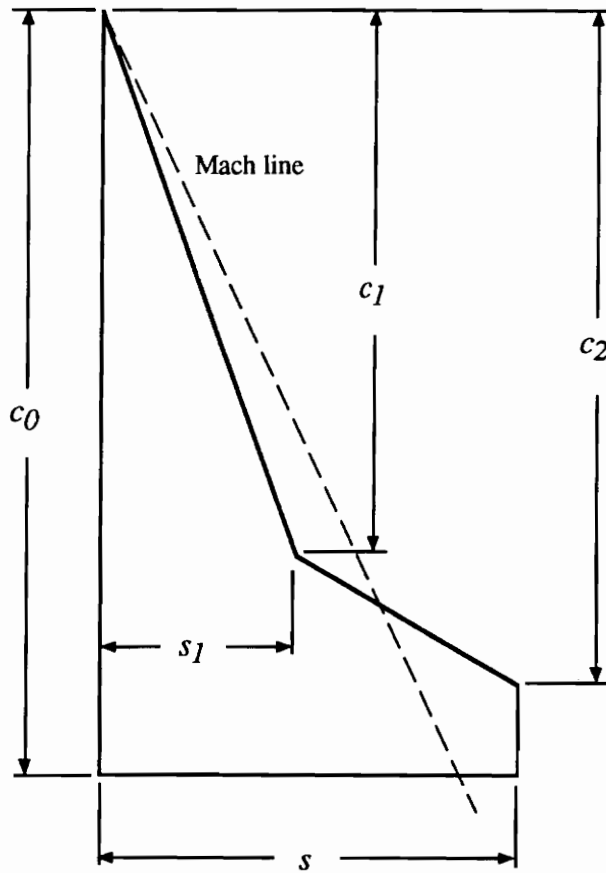
Fig. 5.9 — Cranked-Wing Planform

Fig. 5.10 compares the C_{L_α} and C_T/C_L^2 obtained from Eqs. (5.2) and (5.3) and the supersonic panel code for cranked wings with $c_0 = 100$, $c_1 = 60$, $c_2 = 90$, $s_1 = 15$ and $50 \leq s \leq 70$. Recall from Ch. 4 that the simple paneling scheme used in the numerical analysis varies discretely with changes in the wing planform. For this reason, and because C_T/C_L^2 is determined solely by the numerical solution in the vicinity of the leading edge, the numerical C_T/C_L^2 results are seen to vary in a nonlinear fashion. Although the basic trend is correct, the values are off by as much as 25%. By contrast, the C_{L_α} values are predicted within an accuracy of about 2%. Since C_{L_α} is a quantity determined by integration over the entire surface of the

wing, it is much less sensitive to the variation in the number of panels. Fortunately, the parameter $1/C_{L_\alpha} - C_T/C_L^2$ is governed primarily by the value of C_{L_α} and thus the drag polar predictions are more accurate than the C_T/C_L^2 results might suggest.
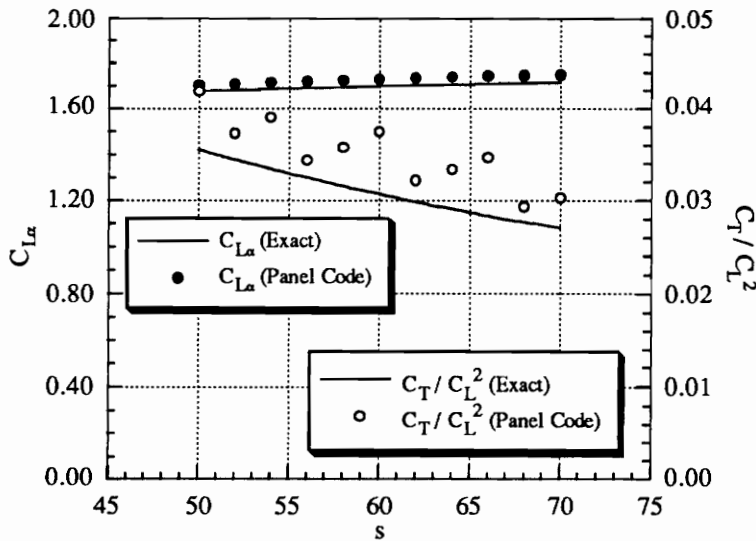
Fig. 5.10 — Comparison of Analytic Solution and Panel Code Results for Cranked Wing; Results Shown for Varying Wing Span

Fig. 5.11 compares C_{L_α} and C_T/C_L^2 for wings with $c_0 = 100$, $c_2 = 90$, $s_1 = 15$, $s = 50$ and $34 \leq c_1 \leq 60$. Again, the panel code predicts C_{L_α} more accurately than C_T/C_L^2, although the errors in C_T/C_L^2 are less apparent than they were in the previous figure.

5.2.2 — Equivalent Cranked Wing

The linear potential solution for a simple cranked wing with an unswept trailing edge, Fig. 5.9, is given by Eqs. (5.2) and (5.3). In order to apply this solution to more general planforms, an *equivalent cranked wing* has been developed.

Investigation of the behavior of Eqs. (5.2) and (5.3) indicates that the leading edge of the planform dictates much of the wing's performance. Consequently, the first step in defining the equivalent cranked wing is to define its leading edge. The
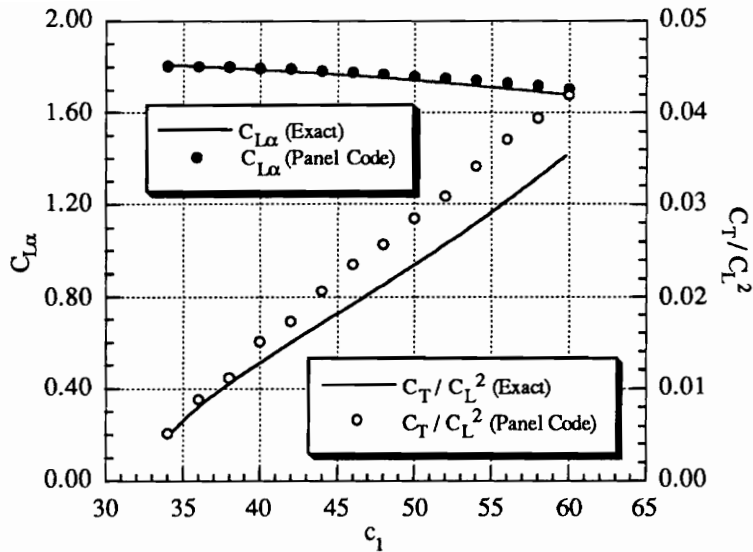
Fig. 5.11 — Comparison of Analytic Solution and Panel Code Results for Cranked Wing; Results Shown for Varying Crank Axial Location

equation defining the leading edge, in the terminology of Fig. 5.9, is given by

$$y_{eq}(x) = \begin{cases} \left(\frac{s_1}{c_1}\right) x, & \text{if } x \leq c_1 \\ \frac{(s-s_1)x+s_1c_2-sc_1}{c_2-c_1}, & \text{if } x > c_1. \end{cases} \tag{5.4}$$

In the Craidon description of the aircraft geometry, the leading edge of the actual wing is defined by M coordinates, (x_{w_i}, y_{w_i}), where X_{w_1} is the x-coordinate of the wing root and is defined to be zero. The sum of the squares of the error between the equivalent cranked wing and the actual wing is given by

$$E_w = \sum_{i=1}^{M} [y_{eq}(x_{w_i}) - y_{w_i}]^2 . \tag{5.5}$$

I define c_2 of the equivalent cranked wing to be the x-coordinate of the actual wing's leading-edge tip, $c_2 = x_{w_M}$. For a given c_1, s_1 and s are given by

$$s_1 = c_1 \frac{\sum_{i=1}^{M_1} x_{w_i} y_{w_i}}{\sum_{i=1}^{M_1} x_{w_i}^2} \tag{5.6}$$

and

$$s = (c_2 - c_1)\frac{\sum_{i=M_1+1}^{M}(x_{w_i} - c_1)y_{w_i}}{\sum_{i=M_1+1}^{M}(x_{w_i} - c_1)^2} - s_1\frac{\sum_{i=M_1+1}^{M}(c_2 - x_{w_i})(x_{w_i} - c_1)}{\sum_{i=M_1+1}^{M}(x_{w_i} - c_1)^2}, \quad (5.7)$$

where M_1 refers to the largest value of i for which $x_{w_i} \leq c_1$. The value of c_1 is determined to minimize the total least-squares error, E_w. This one-dimensional minimization problem is solved using a golden-section search algorithm.

Finally, c_0 is determined to give the equivalent cranked wing the area of the actual wing, S_w. That is,

$$c_0 = \frac{1}{2}\left(\frac{S_w - s_1c_2}{s} + c_1 + c_2\right). \quad (5.8)$$

If this expression yields a value of $c_0 < c_2$, I use $c_0 = c_2$, and the actual wing area is not equal to the equivalent wing's area.

The performance of the approximate model is assessed in Figs. 5.12 and 5.13. Fig. 5.12 compares the value of C_{L_α} predicted by the simple model with that predicted by the supersonic panel code. Fig. 5.13 compares the simple and detailed analysis values of C_T/C_L^2. Again, the results are presented as a function of the design change parameter ξ in Eq. (5.1). As in the previous section, $\mathbf{x}_0$ and $\mathbf{x}_1$ represent two vectors of design variables, the initial and WFN_{m12} designs. The agreement between the detailed and simple models is quite favorable, given the broad range in design space between these two planforms; in the optimization process, this design change would be composed of many design cycles. The simple model is more accurate at $\xi = 0$ (the initial design) than at $\xi = 1$ (the WFN_{m12} design), since the initial design planform is very close to a simple cranked-wing planform and the final design is less so (see Ch. 6). In addition, it should be noted that at the beginning of each design cycle the global-local approximation has a value equal to that predicted by the detailed analysis.

Figs. 5.14 and 5.15 show approximations to C_{L_α} and C_T/C_L^2 for the three different methods available in the optimization: scaled, linear and global-local approximations. Note that there are small-scale oscillations in the panel-code predictions
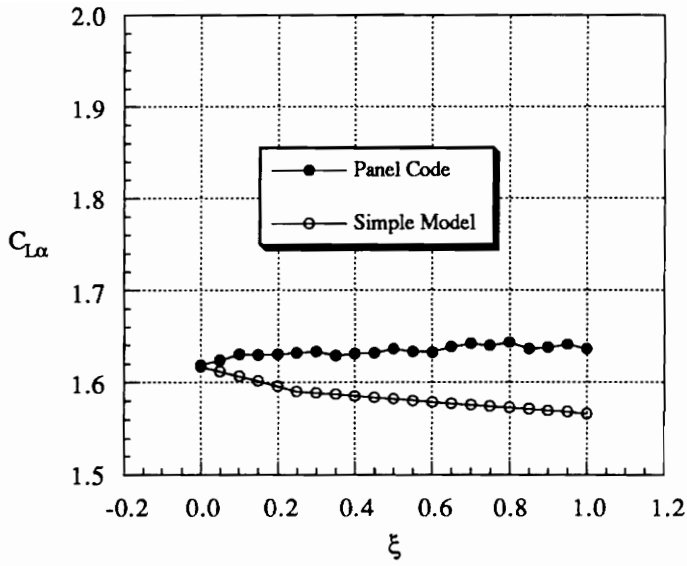
Fig. 5.12 — Equivalent-Cranked-Wing Estimate of C_{L_α}, from Initial Design to WFN_{m12} Design
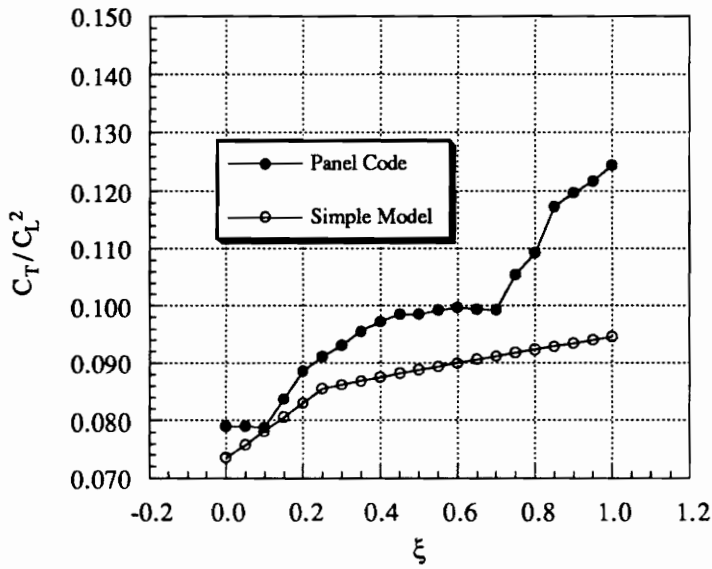
Fig. 5.13 — Equivalent-Cranked-Wing Estimate of C_T/C_L^2, from Initial Design to WFN_{m12} Design

for C_{L_α} in Fig. 5.14 due primarily to the paneling discretization scheme. The variations are much more apparent in the C_T/C_L^2 values shown in Fig. 5.15. This noise in the analysis makes the calculation of finite-difference derivatives for use in the linear and global-local approximations unreliable. To combat this problem, large perturbations were made in the design variables to estimate the derivatives (*e.g.*, $\Delta x = 0.15$ for design variables scaled to have values between 0.1 and 10) so as to span the scale of the noise. In theory, the truncation error associated with large values of variable perturbation contaminates the value of the estimated derivative, but because of the noise, small perturbations are impractical and thus the point is purely academic.

The result of this strategy is most apparent in Fig. 5.15, where the two derivative-based approximations are not tangent to the detailed analysis results at $\xi = 0$. In spite of these difficulties, the approximations show reasonable agreement with the detailed analysis results for small values of ξ. Since, in an optimization process, the design change represented by $\xi = 0$ to $\xi = 1$ would actually take place in a number of design cycles, the accuracy of the approximations is of interest primarily in the region of $\xi = 0$.

5.3 — Landing Angle of Attack, Three Models

Recall from Ch. 4 that the estimation of landing angle of attack is governed principally by the subsonic lift-curve slope, C_{L_α}. (Note that I use the same notation as for the supersonic lift-curve slope; although they refer to the same quantity, the magnitude and the methods used in the analysis for the two flight regimes are quite different.) Three simple models for estimating C_{L_α} are presented: the equivalent-arrow-wing model, a method based on the technique of Nicolai, and a third model derived from the method of Diederich. Each of these models is discussed separately. In addition, some preliminary optimization results are presented that illustrate the hazard of using only a simple analysis model for the estimation of the landing angle of attack.
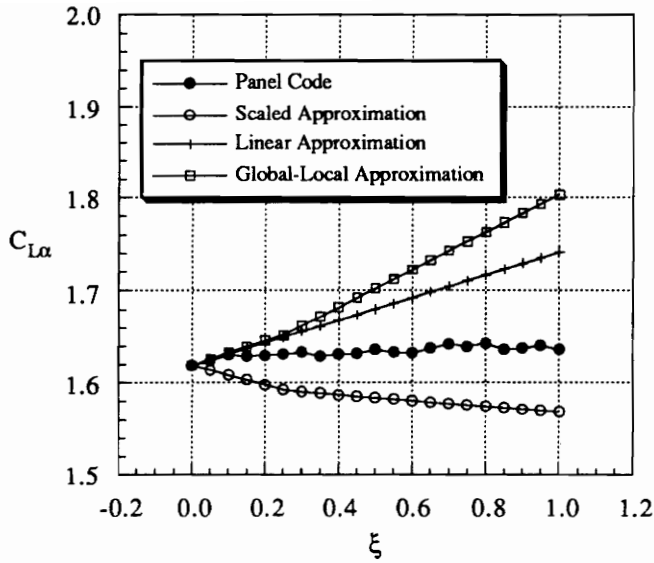
Fig. 5.14 — Supersonic C_{L_α} Predictions for Three Approximation Methods, from Initial Design to WFN_{m12} Design
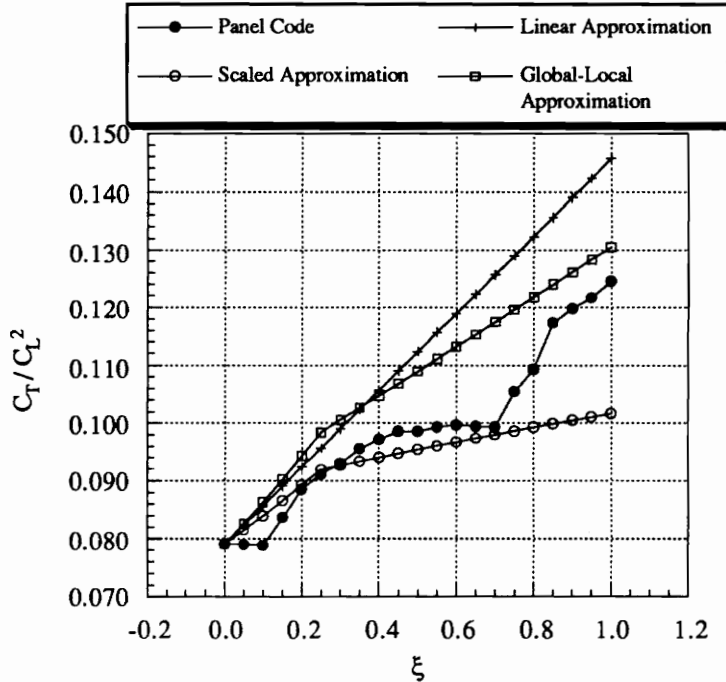
Fig. 5.15 — Supersonic C_T/C_L^2 Predictions for Three Approximation Methods, from Initial Design to WFN_m Design

5.3.1 — Equivalent-Arrow-Wing Model

This model is based upon the work of Ref. 54, in which Ericsson and Reding present a C_{L_α} expression for slender wings with swept trailing edges in subsonic flow. In the terminology used here, their relation may be written as

$$C_{L_\alpha} = \frac{3.4}{\theta_{LE}} \left[\frac{A(1 - \tan\theta_{LE}\tan\Lambda_{TE})}{4} \right]^{3/2}, \tag{5.9}$$

where A is the aspect ratio, Λ_{LE} and Λ_{TE} are the leading and trailing-edge sweep angles of the equivalent arrow wing and $\theta_{LE} \equiv \pi/2 - \Lambda_{LE}$. These angles are defined by span-weighted averages of the actual wing's leading and trailing edges,

$$\Lambda_{LE} = \frac{1}{s}\sum_i \Delta y_i \tan^{-1}\left(\frac{\Delta x_{LE_i}}{\Delta y_i}\right) \quad \text{and}$$

$$\Lambda_{TE} = \frac{1}{s}\sum_i \Delta y_i \tan^{-1}\left(\frac{\Delta x_{TE_i}}{\Delta y_i}\right), \tag{5.10}$$

where Δx_i and Δy_i are the differences in x and y of adjacent wing definition points used in the Craidon geometry, and s is the wing semi-span. Dr. Eric Unger developed this strategy for defining the equivalent arrow wing.

Fig. 5.16 compares the values of C_{L_α} predicted by the VLM code and the simple model for the same design change as was used in the previous sections. Note that the general trend of the simple model matches that indicated by the VLM analysis, even though the magnitude differ by 8-10%.

Fig. 5.17 compares the C_{L_α} predictions over the same design change from the three approximation methods available during the optimization. The agreement is quite favorable, especially in the important region near $\xi = 0$. Note in particular that, for ξ less than about 0.2, the derivative-based approximations (*i.e.*, linear and global-local) are more accurate than the scaled approximation.

5.3.2 — Nicolai Model

A second simple model is found in Ref. 55. Nicolai presents the following expression for the lift-curve slope

$$C_{L_\alpha} = \frac{\pi A}{\sqrt{4 + A^2(1 + \tan^2\Lambda_{3c/4})}}. \tag{5.11}$$

Fig. 5.16 — Subsonic C_{L_α} Predicted by Equivalent-Arrow-Wing Model, from Initial Design to WFN_{m12} Design

Fig. 5.17 — Subsonic C_{L_α} Predicted by Three Approximate Methods (using Equivalent-Arrow-Wing Model for Simple Analysis), from Initial Design to WFN_{m12} Design

Again, A is the aspect ratio. Here I must provide an estimate for $\tan^2 \Lambda_{3c/4}$ ($\Lambda_{3c/4}$

refers to the sweep of the wing's three-quarter chord) from the actual configuration. I chose an area-weighted average given by

$$(\tan^2 \Lambda_{3c/4})_{eq} = \frac{2}{S_w} \sum_i c_i \Delta y_i \left(\frac{\Delta x_{3c/4_i}}{\Delta y_i} \right)^2, \tag{5.12}$$

where c_i is the chord of the wing at the given wing definition location and S_w is the wing area.

Figs. 5.18 and 5.19 compare the results predicted by Eq.(5.11) and the three approximate models, respectively, with those from the VLM code. In Fig. 5.19, note that the derivative-based approximations are much more accurate than the scaled approximation for small values of ξ.
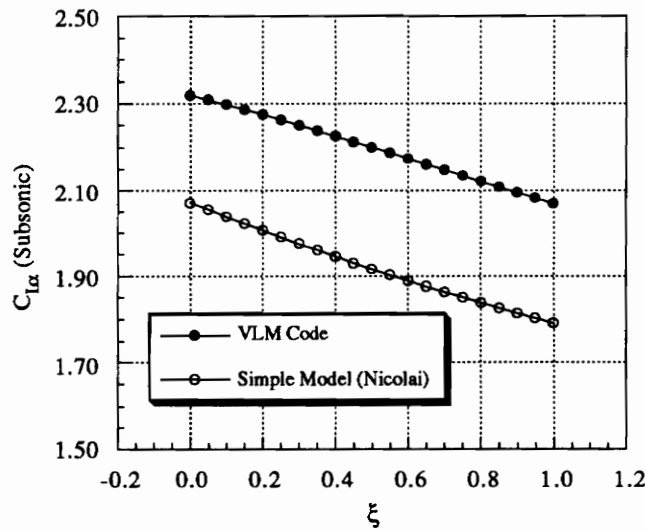
Fig. 5.18 — Subsonic C_{L_α} Predicted by Nicolai Model, from Initial Design to WFN_{m12} Design

5.3.3 — Diederich Model

A third model is given by Diederich.[56] It provides yet another method of estimating C_{L_α}, given by

$$C_{L_\alpha} = \frac{2\pi A \cos \Lambda_{c/4}}{\sqrt{A^2 + 2A \cos \Lambda_{c/4} + 4 \cos^2 \Lambda_{c/4}}}, \tag{5.13}$$
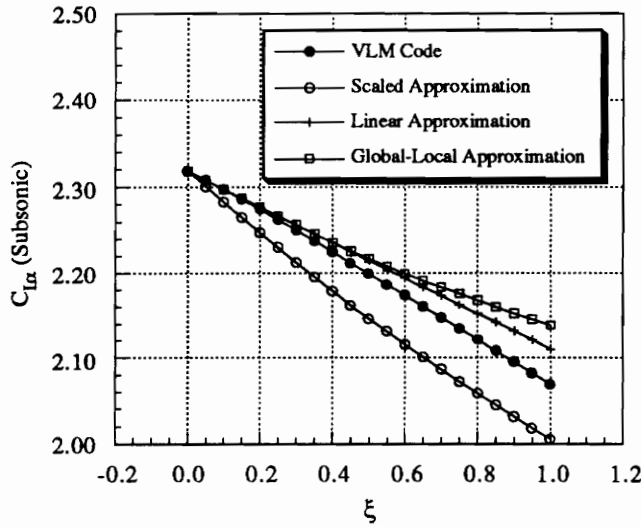
Fig. 5.19 — Subsonic C_{L_α} Predicted by Three Approximate Methods (using Nicolai Model for Simple Analysis), from Initial Design to WFN_{m12} Design

where $\Lambda_{c/4}$ refers to the sweep of the wing's quarter-chord line. Here, $\cos\Lambda_{c/4}$ must be estimated, and again an area-weighted average is used,

$$(\cos\Lambda_{c/4})_{eq} = \frac{2}{S_w} \sum_i c_i \frac{\Delta y_i^2}{\sqrt{\Delta y_i^2 + \Delta x_{c/4_i}^2}}, \qquad (5.14)$$

where $x_{c/4}$ refers to the x-location of the quarter chord.

Figs. 5.20 and 5.21 compare the results predicted by Eq. (5.13) and the three approximate models, respectively, with those from the VLM code. As shown in Fig. 5.20, the derivative-based methods are again more accurate than the scaled approximation for small values of ξ.

5.3.4 — Optimization using Simple Landing Models

With regard to simple models, design optimization differs from the traditional design process in at least one important aspect: numerical optimizers are ignorant of the limitations inherent in a given analysis method. Conceptual-level analysis methods work well in the traditional process because the predicted performance
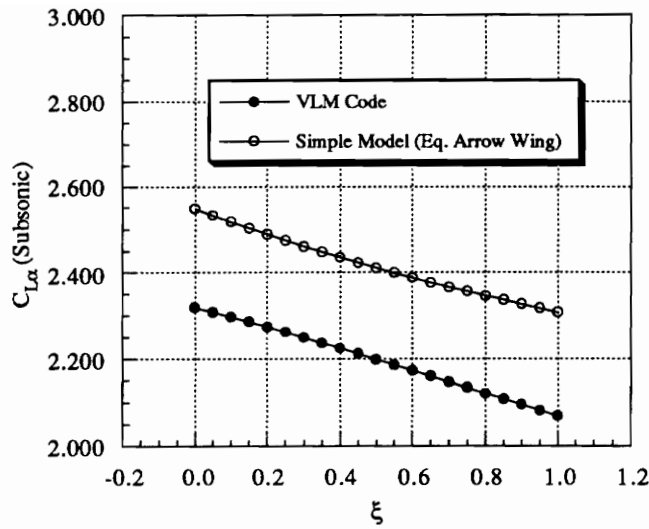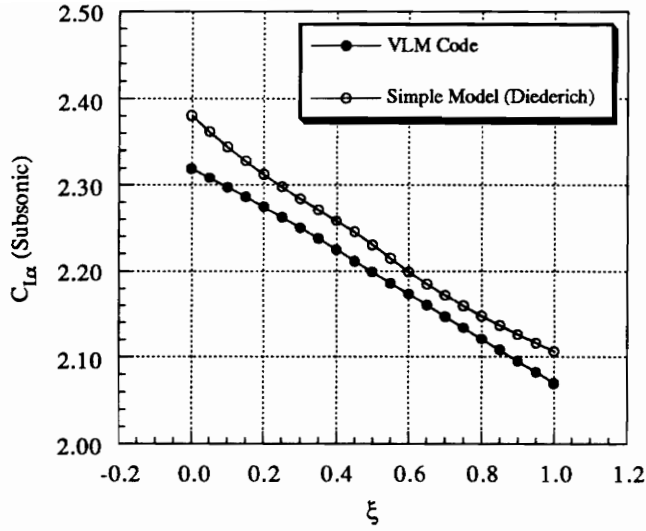
Fig. 5.20 — Subsonic C_{L_α} Predicted by Diederich Model, from Initial Design to WFN_{m12} Design

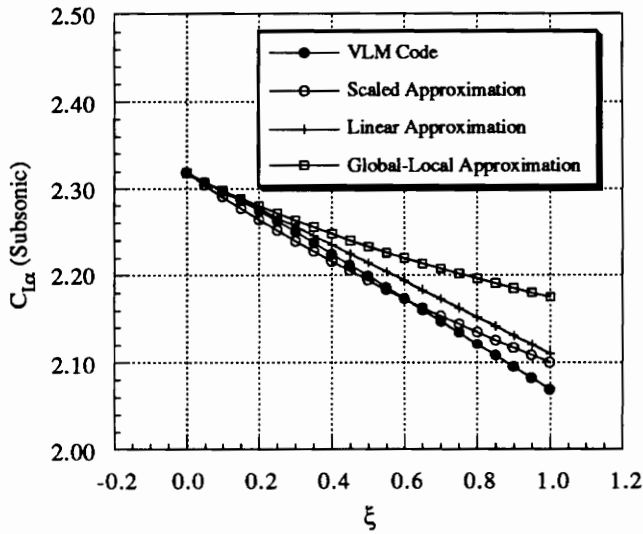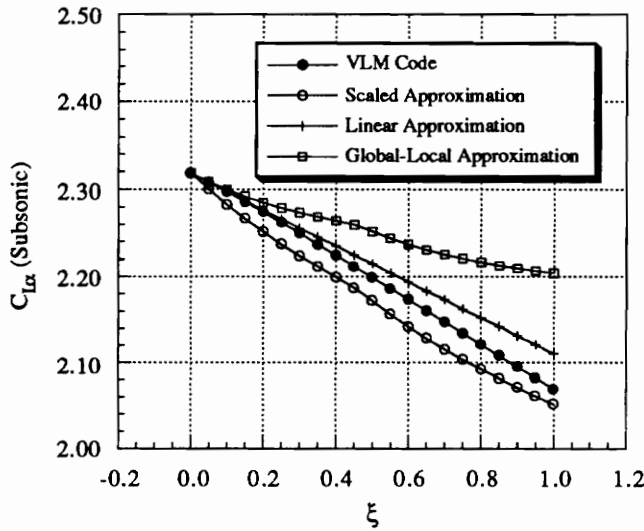**Fig. 5.21** — Subsonic C_{L_α} Predicted by Three Approximate Methods (using Diederich Model for Simple Analysis), from Initial Design to WFN_m Design

results are balanced against the design engineer's experience to determine what is

possible and reasonable. In numerical optimization, however, the optimizer only sees the effects of the analysis that it has in hand. Optimizers are designed to work very hard to take advantage of any gains to be had in the available analysis. Unfortunately, an optimizer, unlike a human designer, is unable to distinguish between real performance gains and apparent gains existing simply because the analysis method has been pushed beyond its limits of applicability.

An illustration comes from some experience with the landing angle of attack constraint. Initially, only the equivalent arrow-wing model was used to estimate the landing performance. The planform that resulted from a design optimization (wing alone) using the equivalent arrow-wing model for landing angle of attack is shown in Fig. 5.22. The first indication of a problem came when the results obtained from the approximate model were compared with those predicted by Lamar's program; see Fig. 5.23. Obviously, the simple model was breaking down for this highly swept planform. Stated another way, the optimizer had successfully exploited a weakness in the conceptual-level model and produced a wing well away from the design space used to develop the simple model. Note in particular that the approximate model was unsuccessful in estimating the basic linear theory portion of the lift-curve slope for small angles of attack; this is significant because C_{L_α} dominates the calculation of the landing angle.

Thinking that the problem lay only in the choice of an appropriate model, Nicolai's method was implemented. The design resulting from 10 cycles of an optimization (it was stopped at this point) is shown in Fig. 5.24. Again, the results of this model were compared with Lamar's vortex lattice method (see Fig. 5.25) and again it was concluded that the optimizer had found a weakness in the approximate model.

Finally, an optimization was attempted using the Diederich model. The design resulting from this optimization is shown in Fig. 5.26, and an evaluation of the approximate model's accuracy in Fig. 5.27.
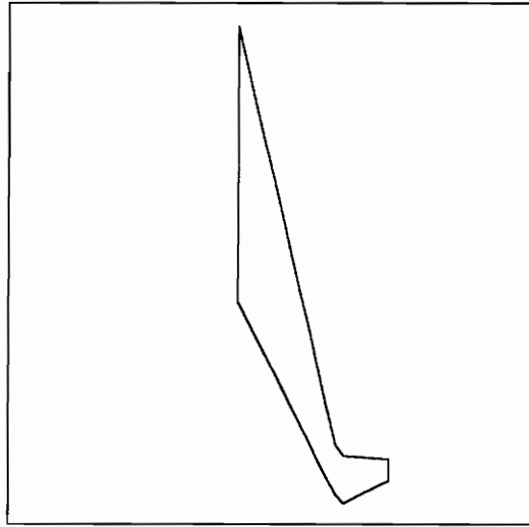
Fig. 5.22 — Wing Planform Obtained using Equivalent-Arrow-Wing Landing Model
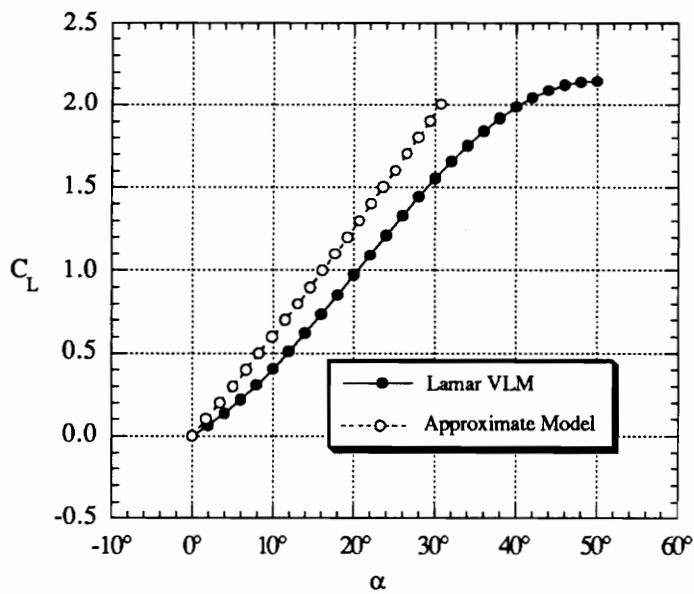
Fig. 5.23 — Final Design, Subsonic Lift Curve using Equivalent-Arrow-Wing Model Compared to Lamar VLM
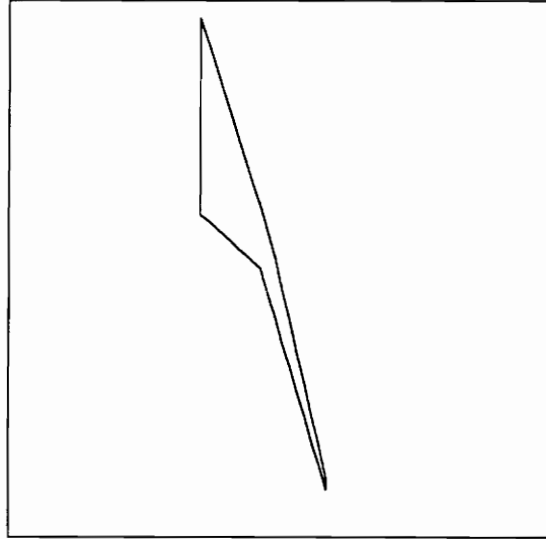
Fig. 5.24 — Wing Planform Obtained using Nicolai Landing Model
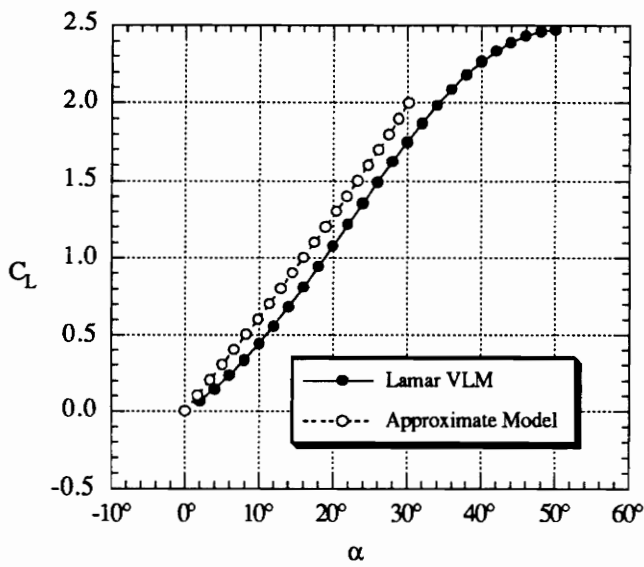
Fig. 5.25 — Final Design, Subsonic Lift Curve using Nicolai Model Compared to Lamar VLM
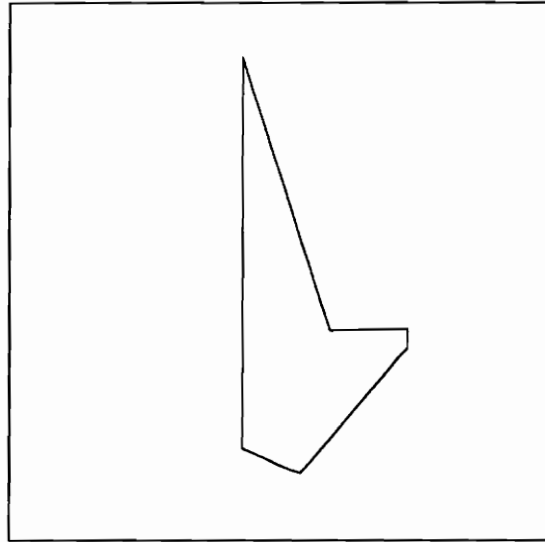
Fig. 5.26 — Wing Planform Obtained using Diederich Landing Model
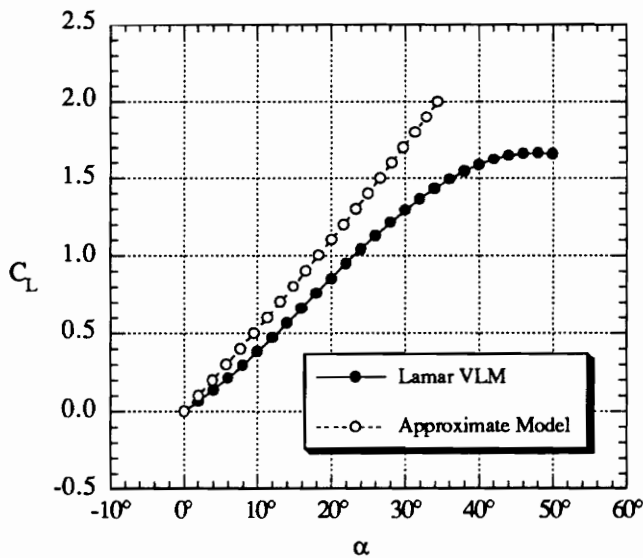
Fig. 5.27 — Final Design, Subsonic Lift Curve using Diederich Model Compared to Lamar VLM

The performance of the approximate models in these three cases forced the implementation of the more sophisticated vortex lattice method described in Ch. 4 to estimate C_{L_α}. It is important to remember that the *only* difference between the three very different planforms obtained from the optimizations was in the model used to predict landing angle of attack. In all three cases the optimizer successfully exploited weaknesses in the models to achieve reductions in the objective function.

The implementation of variable-complexity modeling used for the calculation of landing angle of attack solved the problem. Using the VLM in conjunction with one of the simple models in the global-local approximation to estimate landing performance produced reasonable wing planforms with reliable estimates for the angle of attack. Fig. 5.28 compares $C_L(\alpha)$ for one of the optimized designs (the WFN_{m12} case, see Ch. 6) predicted by the detailed landing-angle-of-attack model with the results from Lamar's VLM program. The agreement is quite favorable. The variable-complexity approach was sufficiently robust to prevent the optimizer from taking advantage of perceived but not actual performance gains.

5.4 — Weight Estimation

There are two aspects to the variable-complexity strategy employed in this research effort. The first is the coupling of simple and more detailed analysis models to reduce the computational cost of the optimization. The second is the use of a simple model to represent the influence of an entire discipline upon the design. For this work, statistical weight equations are employed to model the effects of structural considerations. Most notably, the wing weight equation is directly affected by such geometric parameters as thickness-to-chord ratio and sweep angle.

The weight equations described here were developed by L. A. McCullers of ViGYAN Research Associates in Hampton, Virginia. They are implemented in his conceptual-sizing code, FLOPS,[57] but have not been published as of this writing. For this reason, the civil-transport weight relations used in this work will be described. These equations were developed as empirical models, with the constants
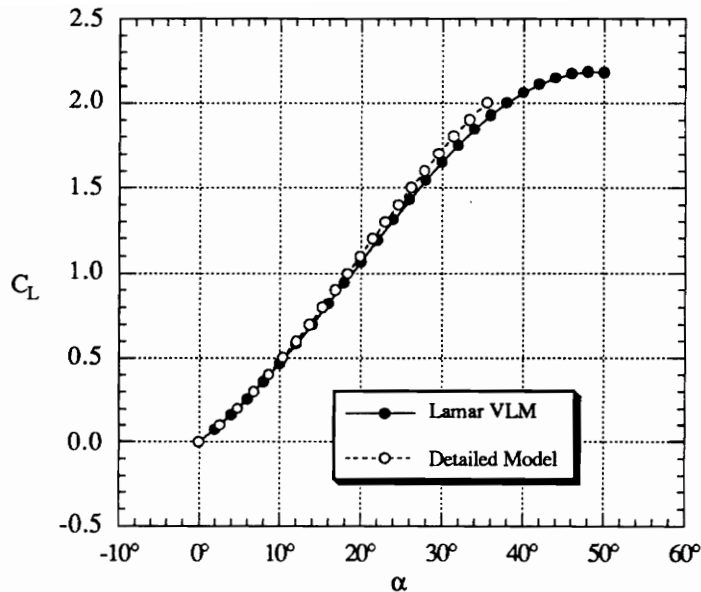
Fig. 5.28 — Subsonic Lift Curve of WFN_{m12} Design Predicted by Detailed Analysis Compared to Lamar VLM

determined to fit data for known aircraft.

The equations are presented as a function of a number of geometric and flight parameters. To avoid needless repetition, these parameters are listed in Table 5.2. If the value of a given parameter is fixed for the analysis, its value is indicated in the table; otherwise, its value is calculated from the Craidon geometry description and is denoted in the table as "calc".

The zero-fuel weight of the aircraft is composed of the individual weights of the following five *groups*: the structures, propulsion, systems and equipment, operating-items, and payload groups. The gross weight is the sum of these, plus the mission fuel; thus,

$$W_{gross} = W_{str} + W_{prop} + W_{sys} + W_{op} + W_{payld} + W_{fuel}. \qquad (5.15)$$

Each of the group weights is, in turn, composed of a number of *component* weights. Each of the groups will be discussed separately.

Table 5.2. Weight Equation Parameters

Parameter	Description	Value
b	Wing span (ft)	calc
d_{fus}	Maximum fuselage depth (ft)	calc
d_{nac}	Maximum nacelle diameter (ft)	calc
f_{cargo}	Cargo aircraft factor	0
f_{ldg}	Fraction of fuel remaining at landing	0.1
f_{sweep}	Variable-sweep wing factor	0
f_{ult}	Ultimate load factor $(g\text{'s})$	3.75
L_{fus}	Length of fuselage (ft)	calc
L_{mlg}	Length of main landing gear (in)	180
L_{nac}	Length of nacelle (ft)	calc
L_{nlg}	Length of nose landing gear (in)	168
L_{pc}	Length of passenger compartment (ft)	206
M	Cruise Mach number	2.4
N_{cen}	Number of engines on centerline	0
N_{ef}	Number of engines on fuselage	0
N_{eng}	Number of engines	4
N_{flcr}	Number of flight crew	2
N_{fus}	Number of fuselages	1
N_{galcr}	Number of galley crew	1
N_{pass}	Number of passengers	$N_{pf} + N_{pt}$
N_{pf}	Number of first-class passengers	0
N_{pt}	Number of tourist-class passengers	251
N_{stew}	Number of stewardesses	6
N_{tank}	Number of fuel tanks	17
N_{vt}	Number of vertical tails	1
p_{hyd}	Hydraulic system pressure (psi)	5,000
R	Aircraft range $(n.\ mi.)$	5,500
s_{eng}	Engine scaling parameter	1.081
S_{flap}	Area of wing used for flaps and controls (ft^2)	$0.1312 S_w$
S_{ht}	Area of horizontal tail (ft^2)	0
S_{vt}	Area of vertical tail (ft^2)	calc
S_w	Wing area (ft^2)	calc

Table 5.2 (cont'd). Weight Equation Parameters (cont'd)

Parameter	Description	Value
t	Wing thickness (ft)	calc
T	Engine thrust (lbs)	39,000
T_{ref}	Reference engine thrust (lbs)	65,482
W_{cargo}	Weight of cargo (lbs)	2,545
w_{fus}	Maximum fuselage width (ft)	calc
$W_{ref\,eng}$	Weight of reference engine (lbs)	17,424
Λ	Average wing sweep	calc
λ_{ht}	Horizontal-tail taper ratio	0
Λ_{ld}	Load-path sweep angle	calc
λ_{vt}	Vertical-tail taper ratio	calc

5.4.1 — Structures Group Weight (W_{str})

The structures group is composed of the individual weights of the wing, horizontal tail, vertical tail, fuselage, landing gear, and nacelles. Thus,

$$W_{str} = W_{wing} + W_{ht} + W_{vt} + W_{fuse} + W_{lg} + W_{nac} . \qquad (5.16)$$

The wing weight is given by

$$W_{wing} = \frac{W_{gross}K_e W_{wing_1} + W_{wing_2} + W_{wing_3}}{1 + W_{wing_1}} . \qquad (5.17)$$

The terms contributing to the above relation are given by the following expressions,

$$K_e = 1 - \left(\frac{B_{te}}{B_t}\right)\left(\frac{W_{pod}}{W_{gross}}\right) ,$$

$$W_{wing_1} = K f_{ult} b(1 - 0.4 f_{comp})(1 - 0.1 f_{aert})\left[1 + f_{sweep}\left(\frac{0.96}{\cos\Lambda_{ave}} - 1\right)\right] ,$$

$$W_{wing_2} = 0.68(1 - 0.17 f_{comp}) S_{flap}^{0.34} W_{gross}^{0.6} ,$$

$$W_{wing_3} = 0.035(1 - 0.3 f_{comp} S_w^{1.5} , \quad \text{and}$$

$$K = (8.8 \times 10^{-6})\left(1 + \sqrt{6.25/b}\right) B_t .$$

The term B_t accounts for the material in the wing structure required to support

the distributed bending loads,

$$B_t = \frac{1}{P\left[1 + (f_{aert}/2)\sin^2\Lambda_{ave} + 0.03K_a(1 - f_{aert}/2)\sin\Lambda_{avg}\right]} \times$$
$$\int_0^{b/2} \frac{dy}{t(y)\cos\Lambda_{ld}(y)} \int_{b/2}^y \frac{p(y_1)c(y_1)(y_1 - y)\,dy_1}{\cos\Lambda_{ld}(y_1)},$$

where

$$K_a = \begin{cases} A - 5, & \text{if } A > 5 \\ 0, & \text{otherwise,} \end{cases}$$

where A is the aspect ratio. The function $p(y)$ represents a chord-normalized loading (I assume an elliptic distribution). The bending material term is normalized by the total load, thus

$$P = \int_0^{b/2} p(y)c(y)\,dy.$$

Since the load is normalized, the load factor does not enter this expression, but is only seen in the equation for W_{wing_1}.

Similarly, B_{te} accounts for the inertial-relief provided by engines located on the wings,

$$B_{te} = \int_0^{b/2} \frac{dy}{t(y)\cos\Lambda_{ld}(y)} \int_{b/2}^y \frac{\delta(\eta_{e_i})(y_1 - y)\,dy_1}{\cos\Lambda_{ld}(y_1)},$$

where $\delta(\eta_{e_i})$ represents the point loads at the different engine locations across the wing span. The magnitude of the loads at these points (accounted for in the K_e expression) is somewhat greater than the engine weights alone since some of the weight of the nacelles, engine controls, *etc.* are included; this collection is referred to as an engine *pod* and has weight given by

$$W_{pod} = \frac{1}{N_{eng}}(W_{eng} + W_{thr} + W_{start} + 0.25W_{ec} + 0.11W_{in}+$$
$$0.13W_{elec} + 0.13W_{hyd} + 0.25W_{fs}) + \frac{W_{nac}}{N_{eng} + N_{cen}/2}.$$

The components of this equation are defined subsequently. Finally, the average load-path sweep angle, $\Lambda_{ld_{avg}}$ is given by

$$\Lambda_{avg} = \frac{b}{2}\int_0^{b/2} y\,\Lambda_{ld}(y)\,dy.$$

The load-path is assumed to follow the three-quarter-chord-line of the wing.

The composite-material and aeroelastic-tailoring factors, f_{comp} and f_{aert}, serve to model the influence of material choice and structural design on the wing weight; they are assigned values between 0 and 1 to represent the fraction of composites and aeroelastic tailoring used in the wing. In the next chapter, these factors are set to different values for different design problems.

The remaining component weights are considerably less involved to estimate. They are given by

$$W_{ht} = 0.53 S_{ht} W_{gross}^{0.2} (\lambda_{ht} + 0.5), \tag{5.18}$$

$$W_{vt} = 0.32 W_{gross}^{0.3} (\lambda_{vt} + 0.5) N_{vt}^{0.7} S_{vt}^{0.85}, \tag{5.19}$$

$$W_{fus} = 1.35 \left[L_{fus} \left(\frac{w_{fus} + d_{fus}}{2} \right) \right]^{1.28} (1 + 0.05 N_{ef}) \cdot$$
$$(1 + 0.38 f_{cargo}) N_{fus}, \tag{5.20}$$

$$W_{lg} = 0.048 W_{ldg}^{0.67} L_{nlg}^{0.43} + 0.0117 W_{ldg}^{0.95} L_{mlg}^{0.43}, \quad \text{and} \tag{5.21}$$

$$W_{nac} = 0.25 \left(N_{eng} + \frac{N_{cen}}{2} \right) d_{nac} L_{nac} T^{0.36}, \tag{5.22}$$

where the approximate landing weight, W_{ldg}, is given by

$$W_{ldg} = W_{gross} - (1 - f_{ldg}) W_{fuel}.$$

5.4.2 — Propulsion Group Weight (W_{prop})

The propulsion group weight is composed of the individual weights of the engines, thrust reversers, starters, engine controls and the fuel system. Thus,

$$W_{prop} = W_{eng} + W_{thr} + W_{start} + W_{ec} + W_{fs}. \tag{5.23}$$

The individual component weights are given by

$$W_{eng} = N_{eng} W_{ref\,eng} \left(\frac{T}{T_{ref}} \right)^{s_{eng}}, \tag{5.24}$$

$$W_{thr} = 0.034 T \left(N_{eng} + \frac{N_{cen}}{2} \right), \tag{5.25}$$

$$W_{start} = 11 N_{eng} M^{0.32} d_{nac}^{1.6}, \tag{5.26}$$

$$W_{ec} = 0.26 N_{eng} T^{0.5}, \quad \text{and} \tag{5.27}$$

$$W_{fs} = 1.07 W_{fuel}^{0.58} M^{0.34} N_{eng}^{0.43}. \tag{5.28}$$

5.4.3 — Systems-and-Equipment-Group Weight (W_{sys})

The systems-and-equipment-group weight is composed of the individual weights of the surface controls, auxiliary power unit, instruments, hydraulics, electrical system, avionics, furnishings and cabin equipment, air conditioning, and anti-icing equipment. Thus,

$$W_{sys} = W_{sc} + W_{apu} + W_{in} + W_{hyd} + W_{elec} + W_{av} + W_{furn} + W_{ac} + W_{ai}. \tag{5.29}$$

The individual component weights are given by

$$W_{sc} = 1.1 M^{0.52} S_{flap}^{0.6} W_{gross}^{0.32}, \tag{5.30}$$

$$W_{apu} = 54 (N_{fus} L_{fus} w_{fus})^{0.3} + 5.4 N_{pass}^{0.9}, \tag{5.31}$$

$$W_{in} = 0.48 (N_{fus} L_{fus} w_{fus})^{0.57} M^{0.5} (10 + 2.5 N_{flcr} + N_{ew} + 1.5 N_{ef}), \tag{5.32}$$

$$W_{hyd} = 0.57 (N_{fus} L_{fus} w_{fus} + 0.27 S_w)(1 + 0.03 N_{ew} + 0.05 N_{ef}) \cdot$$
$$\left(\frac{3000}{p_{hyd}} \right)^{0.35} (1 + 0.04 f_{sweep}) M^{0.33}, \tag{5.33}$$

$$W_{elec} = 92 L_{fus}^{0.4} w_{fus}^{0.14} N_{fus}^{0.27} N_{eng}^{0.69} (1 + 0.044 N_{flcr} + 0.0015 N_{pass}), \tag{5.34}$$

$$W_{av} = 15.8 R^{0.1} N_{flcr}^{0.7} (N_{fus} L_{fus} w_{fus})^{0.43}, \tag{5.35}$$

$$W_{furn} = 127 N_{flcr} + 112 N_{pf} + 44 N_{pt} + 2.6 L_{pc} (w_{fus} + d_{fus}) N_{fus}, \tag{5.36}$$

$$W_{ac} = \left[3.2 (N_{fus} L_{fus} w_{fus} d_{fus})^{0.6} + 9 N_{pass}^{0.83} \right] M + 0.075 W_{av}, \quad \text{and} \tag{5.37}$$

$$W_{ai} = \frac{b}{\cos \Lambda} + 3.8 d_{nac} N_{eng} + 1.5 w_{fus}. \tag{5.38}$$

5.4.4 — Operating-Items Group Weight (W_{op})

The operating-items group weight is composed of the crew and their baggage, the unusable fuel, the engine oil, the passenger service, and the cargo/baggage

containers. Thus,

$$W_{op} = W_{crew} + W_{uf} + W_{oil} + W_{serv} + W_{con} .\qquad(5.38)$$

The individual component weights are given by

$$W_{crew} =225N_{flcr} + 155N_{stew} + 200N_{galcr} ,\qquad(5.39)$$

$$W_{uf} =11.5N_{eng}T^{0.2} + 0.07S_w + 1.6N_{tank}W_{fuel}^{0.28} ,\qquad(5.40)$$

$$W_{oil} =0.082N_{eng}T^{0.65} ,\qquad(5.41)$$

$$W_{serv} =(5.164N_{pf} + 2.529N_{pt}) \left(\frac{R}{M}\right)^{0.225} , \quad \text{and}\qquad(5.42)$$

$$W_{con} =175 \left\lfloor \frac{W_{cargo} + W_{bagg}}{950} + 0.99 \right\rfloor ,\qquad(5.43)$$

where the quantity in the braces represents the number of containers and is rounded down to the nearest integer.

5.4.5 — Payload Group Weight (W_{payld})

The payload group weight is composed of the weights of passengers, passenger baggage and cargo; thus,

$$W_{payld} = W_{pass} + W_{bagg} + W_{cargo} .\qquad(5.44)$$

The individual weights are given by

$$W_{pass} =165N_{pass} ,\qquad(5.45)$$

$$W_{bagg} = \begin{cases} 35N_{pass} , & \text{if } R \le 900 \ n.\ mi. \\ 40N_{pass} , & \text{if } 900 < R \le 2900 \ n.\ mi. \\ 44N_{pass} , & \text{if } R > 2900 \ n.\ mi. \end{cases}\qquad(5.46)$$

and the cargo weight, W_{cargo}, is input directly (see Table 5.2 for value).

Since W_{gross} depends on each of the above component weights, and since a number of those components in turn depend on W_{gross}, the computation is implicit and is performed numerically. A fixed-point iteration scheme was employed, with

an initial value of $W_{gross_0} = 500,000 \, lbs$. The calculation typically converges in just 5 or 6 iterations.

Table 5.3 lists the CPU times required for each of the simple analysis methods described in this chapter. Those analyses shown in the table having CPU-times of less than 0.001 sec are denoted < 0.001. It can be seen that the execution time for the simple models is much less than for the corresponding detailed-model times listed at the beginning of the chapter.

Table 5.3. CPU Times (Silicon Graphics 4D/340 VGX Workstation) for Simple Analyses

Analysis	CPU Time (sec)
Wave Drag	0.302
Drag Due to Lift	0.003
Eq. Arrow Wing Ldg. Model	< 0.001
Nicolai Ldg. Model	< 0.001
Diederich Ldg. Model	< 0.001
Weight Estimation	0.102

Several optimization case studies are presented in this chapter that illustrate the capability of the methods and strategies employed. The cases are divided into two groups: aircraft designs with metallic-structure wings and those with composite-structure, aeroelastically-tailored wings. Recall from Ch. 5 that the structural material in the wings is modeled with empirical factors in the wing weight equation. In spite of the model's simplicity, the effect these factors have upon the resulting configurations illustrate the interdisciplinary nature of HSCT design considerations.

In the metallic-wing group, three problems are considered: a wing-alone optimization case, a wing-fuselage-nacelle case, and a second wing-fuselage-nacelle case with a more stringent requirement on landing angle of attack. The wing-alone case illustrates the first level of design-optimization capability (the wing design problem was the first investigated in this research program[24,34]). The wing-fuselage-nacelle cases demonstrate the advantages accrued by simultaneously designing the entire configuration. Finally, the additional wing-fuselage-nacelle case illustrates the significant impact that off-design considerations (here, the maximum landing angle of attack) can have on configuration design. For the composite-wing group, three cases are presented: two wing-alone, and a wing-fuselage-nacell case; all three with the nominal (12°) landing-angle requirement.

I refer to the wing-alone and wing-fuselage-nacelle designs as W and WFN designs, respectively. To indicate metallic or composite-wing cases, I use the subscripts m or c. Finally, the landing angle-of-attack limitation is given as a subscript indicating the value of the constraint in degrees. The nominal value of the constraint was 12°, and for the more stringent metallic-wing case was 11°. Thus, the 6 cases considered are denoted W_{m12}, WFN_{m12}, WFN_{m11}, W_{c12}, W_{c12_2} and WFN_{c12}. At the end of the chapter, the starting and ending design variables for each of the designs are listed.

The global-local method was used to approximate the wave drag, drag due to lift and subsonic lift-curve slope for all the results presented. Somewhat arbitrarily, the Diederich model was used as the simple model for subsonic lift-curve slope estimation.

As will be seen, all the gross weight convergence histories display significant oscillation in the convergence. These oscillations are due to errors in the drag approximation used in each design cycle for the range calculation. These errors may, in turn, be attributed largely to difficulties in estimating the derivatives of the supersonic drag-due-to-lift parameters because of the panel code's noisy behavior for small design changes. Recall that at the beginning of a design cycle, the global-local approximation produces a drag estimate that is equal to that predicted by the detailed analyses. Throughout the design cycle, the range is estimated using only the drag approximation and, thus, a range of 5,500 $n.\ mi.$ is always predicted at the end of a given cycle by the *approximate* analysis. If, at the beginning of the next cycle (when the drag on the design is predicted by the detailed analyses), the range is different from this value, the optimizer immediately compensates for this error. The most direct means is the addition or deduction of mission fuel, thereby increasing or decreasing both range and gross weight.

A related issue is the selection of design-variable move limits. Recall that the maximum change allowed in a design variable during a design cycle is prescribed at the beginning of the cycle. Move limits prevent excessive performance estimation errors resulting from the approximate optimization strategy employed in each cycle. Of the two key performance parameters—range and landing angle of attack—the approximate landing-angle calculation was usually well-behaved and the range was not. That is, it was the range error that dictated the size of the move limits. Typically, at the beginning of an optimization, I would use relatively large move limits (7%) for a few cycles, provided the range error at the start of the next cycle did not exceed approximately 200 $n.\ mi.$ (3.6% of the constraint value). As the

design progressed, I would reduce the move limits to keep the range error to less than 100 *n. mi.* until, as the design neared convergence, I would further reduce the limits to ensure that the range requirement was satisfied nearly exactly.

The measure of convergence was the objective function, the gross weight. Once the gross weight reached a relatively constant value, provided the performance constraints were satisfied, the design was presumed to have converged. Computationally, the wing-alone cases required about 6 CPU-minutes per cycle on a Silicon Graphics 4D/340 VGX workstation. The wing-fuselage-nacelle cases required about 12 CPU-minutes per cycle on the same machine.

6.1 — Metallic-Wing-Structure Optimization Cases

In Ch. 5, I presented the equations used to estimate the aircraft's component weights. In Eq. (5.17), the wing weight is presented as a function of, among other things, the composite-material factor, f_{comp}, and the aeroelastic-tailoring factor, f_{aert}. To represent a metallic-structure wing, both of these factors are set to $f_{comp} = f_{aert} = 0$. In the following discussion, I will briefly describe the 3 metallic-wing cases separately, and then make some general comments on comparisons between them.

Table 6.1. Move Limits Used for W_{m12} Case

Design Cycle	Design Variable Move Limits
1-20	7%
21-40	3%
41-56	2%

6.1.1 — Wing-Alone Case (W_{m12})

For this design, the fuselage and spanwise nacelle locations were not varied. As was shown in Ch. 2 (see Table 2.1), 16 design variables are employed to define the problem. The constraints used are described in Ch. 3; the nominal values of the constraints were utilized. The initial design for the W_{m12} case was the parametric model corresponding to the baseline configuration. This case converged in 56 design
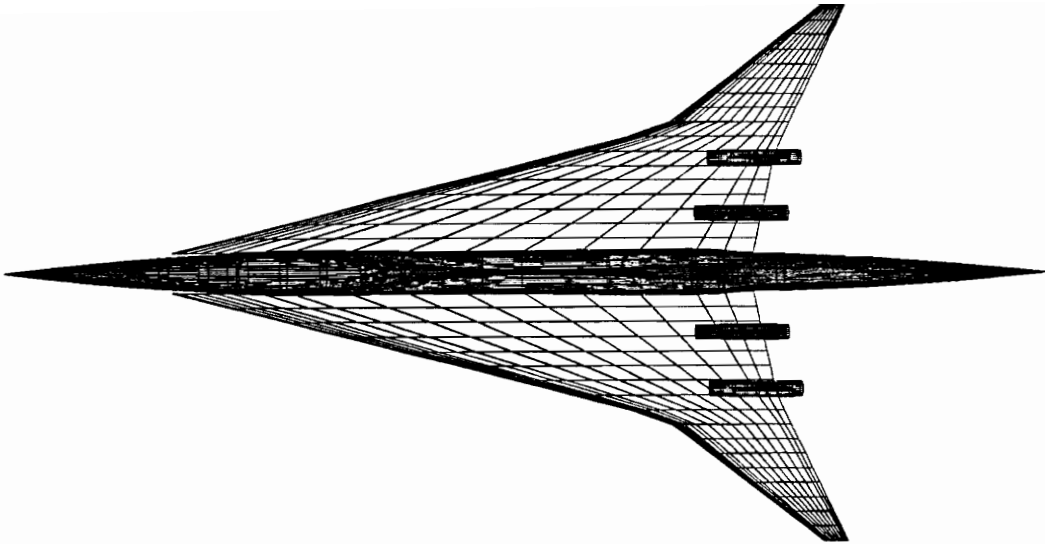
Fig. 6.1 — Metallic-Wing Wing-Alone Design (W_{m12})

cycles and is shown in Fig. 6.1. The move limits used for the different cycles are shown in Table 6.1.

Convergence histories of the gross weight, the range and the landing angle of attack are shown in Figs. 6.2 and 6.3, respectively. The oscillations in the results are quite noticable. Note that the oscillations in the gross weight and range are synchronized; when the range goes down, so does the gross weight. The degree of oscillation closely follows the size of the move limits; that is, reduction of the size of the move limits clearly reduces the magnitude of the oscillations.

6.1.2 — Wing-Fuselage-Nacelle Case (WFN_{m12})

For this design, the full set of 26 design variables defining the wing, fuselage and nacelle locations was employed (see Ch. 2). The constraint values used in the design were again the nominal values outlined in Ch. 3. For reasons explained later, the initial design for the WFN_{m12} case combined the W_{m12} wing design variables with the fuselage and nacelle variables from the baseline configuration. Given this
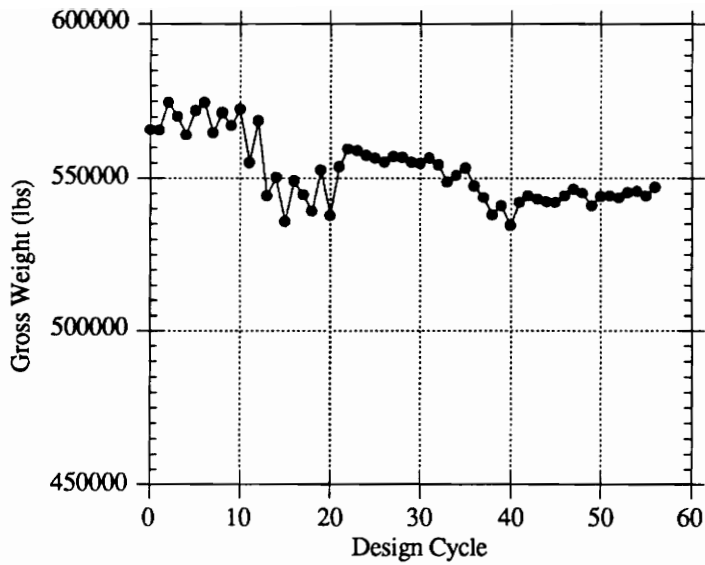
Fig. 6.2 — Gross Weight Convergence History for W_{m12} Case
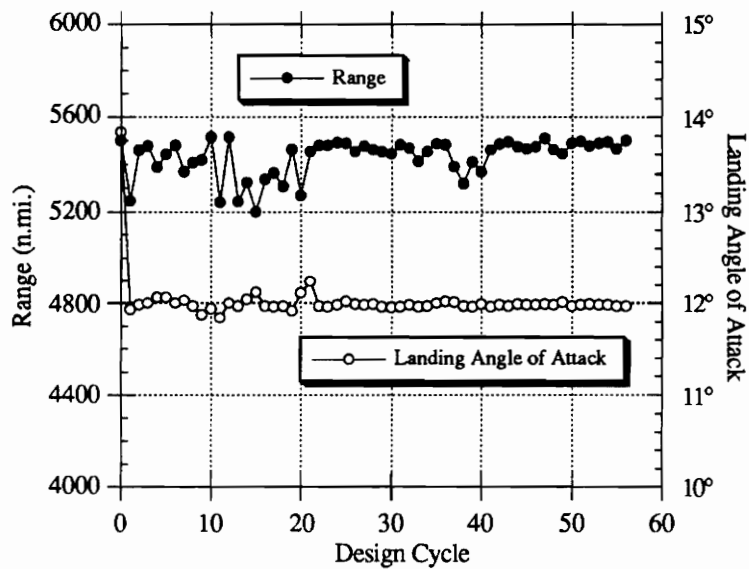
Fig. 6.3 — Range and Landing-Angle-of-Attack Convergence History for W_{m12} Case

good starting point, this case converged in 34 cycles and is shown in Fig. 6.4. The move limits are summarized in Table 6.2.
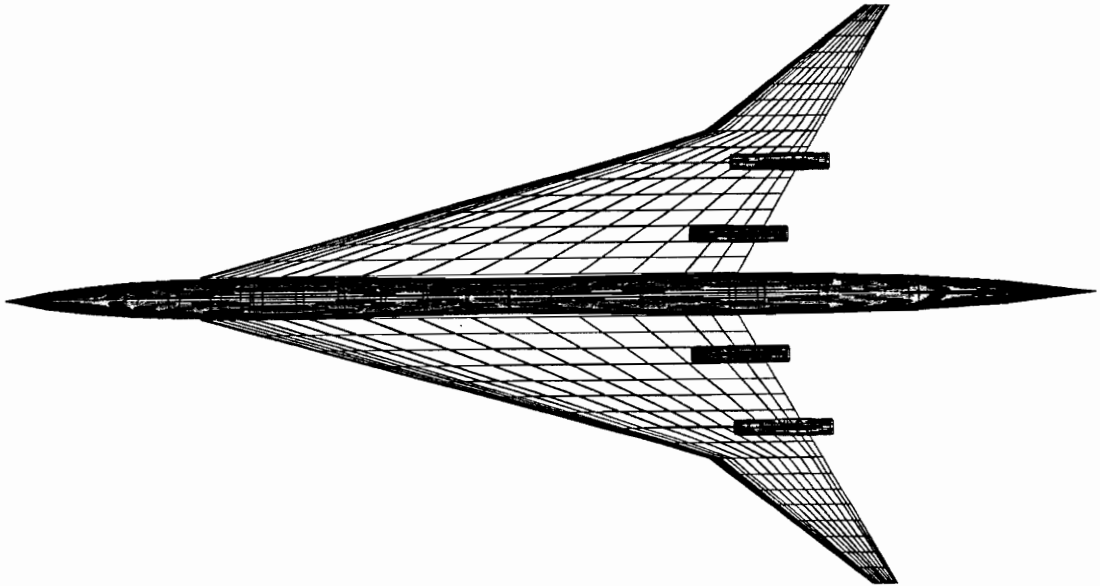
Fig. 6.4 — Metallic-Wing Wing-Fuselage-Nacelle Design (WFN_{m12})

Table 6.2. Move Limits Used for WFN_{m12} Case

Design Cycle	Design Variable Move Limits
1-10	7%
11-20	5%
21-30	3%
31-34	2%

Convergence histories of the gross weight, the range, and the landing angle of attack are shown in Figs. 6.5 and 6.6. The oscillations are again apparent, but are significantly less severe than for the W_{m12} case. This may be due partly to starting from a converged wing design, thus allowing the optimizer to make minimal changes to the wing planform (thereby eliminating much of the noise associated with the

supersonic panel code) while modifying the wing thickness, fuselage, and the nacelle locations.
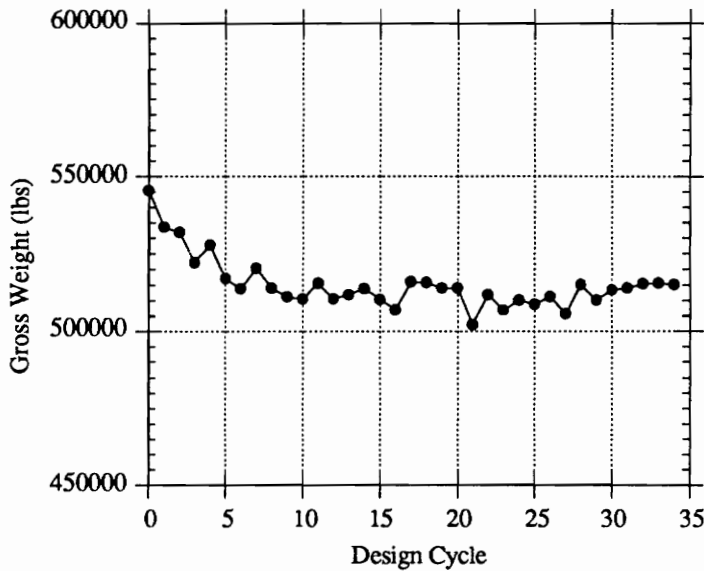
Fig. 6.5 — Gross Weight Convergence History for WFN_{m12} Case

6.1.3 — Wing-Fuselage-Nacelle Case for Reduced Landing Angle (WFN_{m11})

For this design, I again used the full set of 26 design variables. All the constraints were set to the nominal values described in Ch. 3, except for the landing-angle-of-attack limitation which was reduced from 12° to 11°. Although this represents only an 8.3% reduction in the constraint, it will be seen that this modest change affects the final design significantly.

The initial design for this case was the converged WFN_{m12} solution. Starting from this point, the WFN_{m11} case converged in only 10 cycles, and is shown in Fig. 6.7. The move limits are shown in Table 6.3.

The gross weight, range and landing angle-of-attack convergence histories are shown in Figs. 6.8 and 6.9. As with the WFN_{m12} case, a good initial design appears to have had a beneficial effect on the degree of convergence oscillations. For this
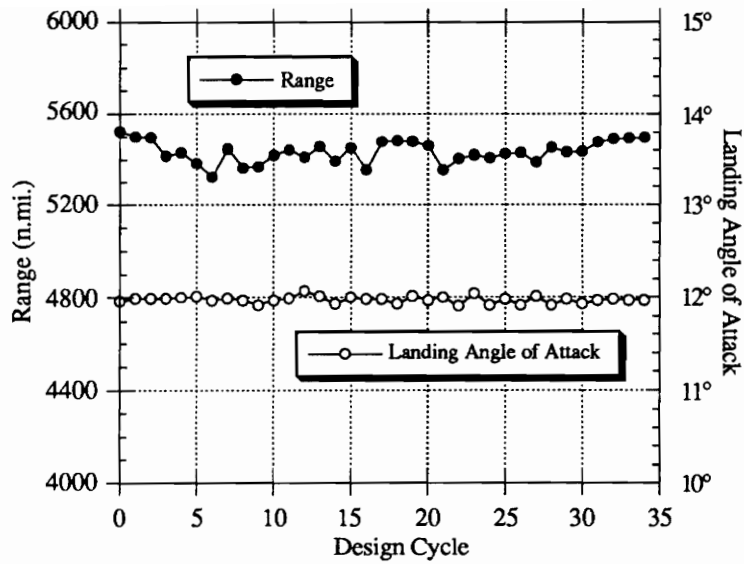
Fig. 6.6 — Range and Landing-Angle-of-Attack Convergence Histories for WFN_{m12} Case

case, the convergence is quite smooth relative to the previous two. Note that a weight penalty was incurred by the more stringent landing-angle requirement.

Table 6.4 presents several details of the three metallic-wing designs. The "initial" design in the table refers to the parametric model corresponding to the baseline configuration. The basic strategy used to reduce the gross weight was a reduction in mission fuel through an increase in aerodynamic efficiency.

The W_{m12} design shows a 3.3% improvement in gross weight compared to the initial design. This weight reduction was achieved through improved aerodynamic efficiency (16.5% increase in $(L/D)_{max}$) resulting in reduced fuel weight, but at the expense of a 22.8% increase in wing weight. Note that the initial design violated the 12° landing-angle requirement; early in the optimization, a weight penalty was incurred to satisfy this constraint.

The first attempt at a metal-wing wing-fuselage-nacelle design used the parametric model of the baseline configuration as the initial design. The final, optimized
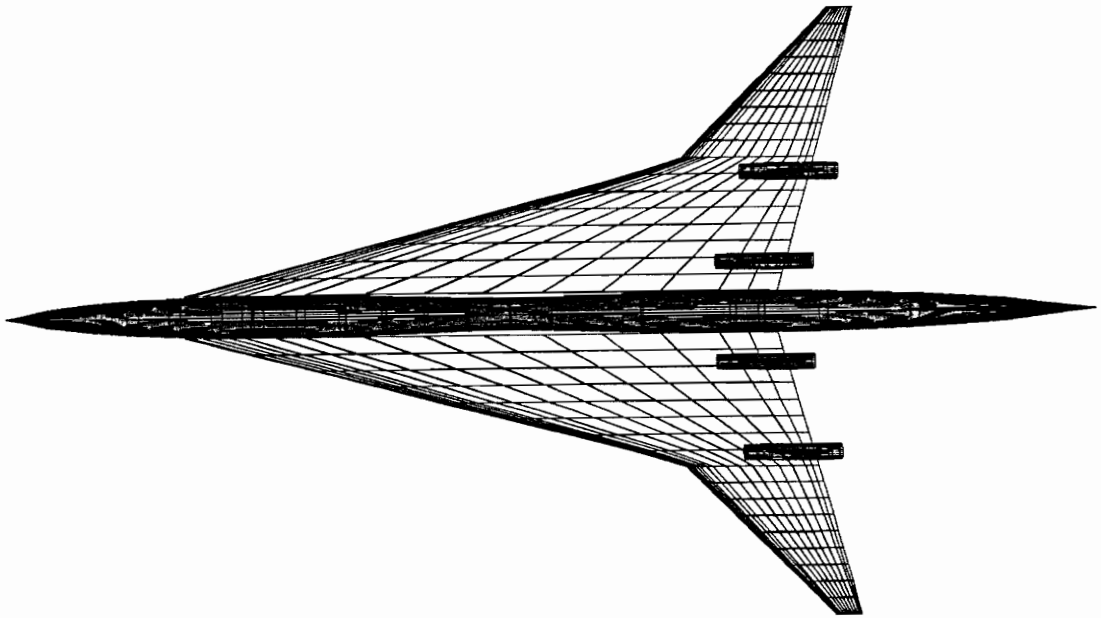
Fig. 6.7 — Metallic-Wing Wing-Fuselage-Nacelle Design for Reduced Landing Angle-of-Attack Requirement (WFN_{m11})

Table 6.3. Move Limits Used for WFN_{m11} Case

Design Cycle	Design Variable Move Limits
1-5	5%
6-10	2%

configuration had a gross weight of 546,607 *lbs*, an insignificant 0.06% improvement over the W_{m12} case. This result was both surprising and disconcerting, since I expected that the 10 additional design variables used to configure the fuselage and nacelles would allow the optimizer greater flexibility and thus yield a significantly improved design.

Another case was considered starting with the converged W_{m12} wing design variables in conjunction with the fuselage and nacelle variables from the model describing the baseline. This is the WFN_{m12} design case. It achieved an 8.8% reduction in gross weight compared to the initial design, and a 5.9% improvement
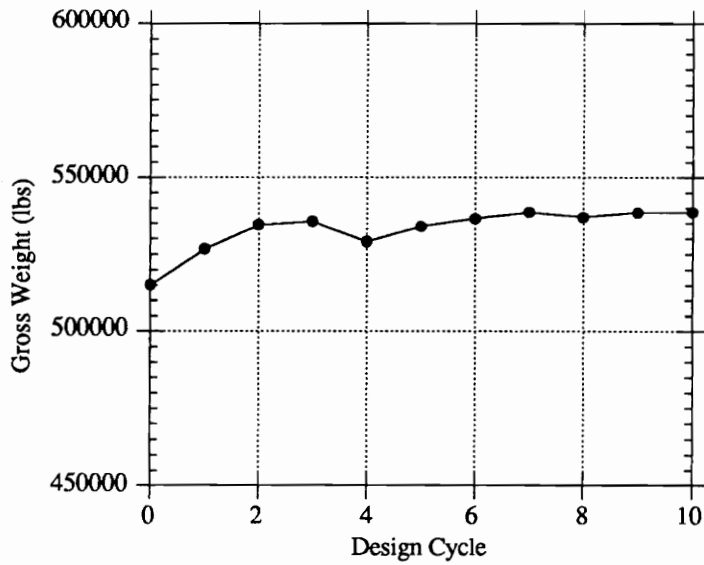
Fig. 6.8 — Gross Weight Convergence History for WFN_{m11} Case
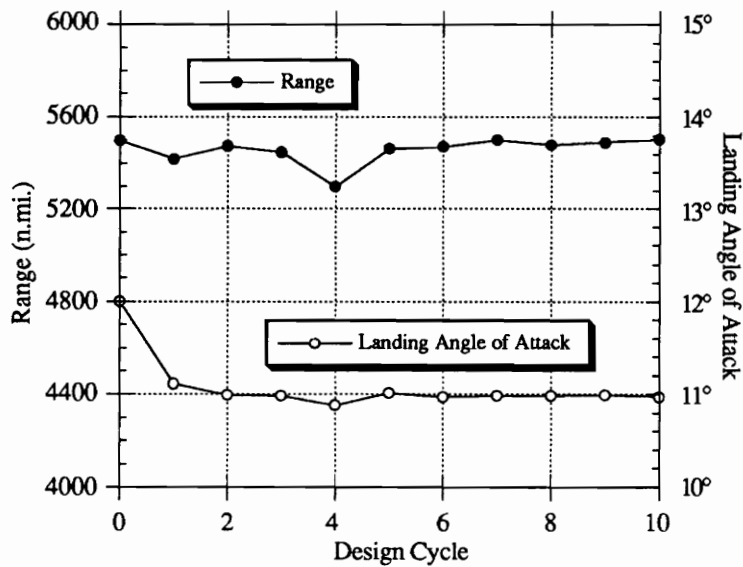
Fig. 6.9 — Range and Landing-Angle-of-Attack Convergence Histories for WFN_{m11} Case

over the W_{m12} design. Again, the weight savings was accomplished largely through

Table 6.4. Initial and Final Design Features

(Metallic-Wing-Structure Cases)

	Initial	W_{m12}	WFN_{m12}	WFN_{m11}
Gross Wt. (*lbs*)	565,760	546,955	514,958	538,494
Fuel Wt. (*lbs*)	290,905	254,590	236,514	248,387
Fuel / Gross	51.4%	46.6%	45.9%	46.1%
Wing Wt. (*lbs*)	70,515	86,611	77,352	85,969
Fus. Wt. (*lbs*)	40,148	40,148	37,746	39,095
Wing Area (ft^2)	9,100	11,460	10,523	11,356
Wing Load (*psf*)	62.17	47.73	48.94	47.42
Aspect Ratio	2.36	2.25	2.59	2.62
Root t/c (%)	2.96	2.14	2.51	2.57
Break t/c (%)	2.36	1.73	2.06	2.04
Tip t/c (%)	2.15	1.51	1.54	1.56
LE Sweep	74.0°	75.3°	74.0°	74.8°
	45.0°	51.8°	51.4°	44.0°
TE Sweep	0.0°	12.2°	29.1°	15.8°
	8.4°	25.3°	29.9°	14.7°
Range (*n. mi.*)	5,500	5,498	5,497	5,503
Landing Angle	13.8°	11.97°	11.97°	10.97°
$(L/D)_{max}$	9.53	11.10	11.32	11.28

improvements in aerodynamic efficiency: an 18.8% increase in $(L/D)_{max}$ relative to the initial design and a 2.0% increase compared to the W_{m12} case. Note, however, that the wing weight in the WFN_{m12} design was only 9.7% heavier than the initial design's. Thus, the increase in aerodynamic efficiency came with less than half of the wing-weight penalty found in the W_{m12} design. This result highlights the beneficial impact that simultaneous optimization of the wing, fuselage, and nacelles has on the design.

Starting from the W_{m12} wing design also improved the time required for optimization. While the design initiated from the baseline configuration converged in 45 cycles, the WFN_{m12} case required only 34.

The WFN_{m11} design, although 4.8% lighter than the initial design, incurred a 4.6% weight penalty relative to the WFN_{m12} design in order to meet the more demanding landing angle-of-attack constraint. The wing area increased 7.9% and the wing weight increased 11.1% relative to the WFN_{m12} case. In spite of these penalties, the WFN_{m11} design was still 1.5% lighter than the W_{m12} design, which again indicates that simultaneous design of the entire configuration is advantageous compared to single-component optimization. To put the weight penalties associated with the 11° landing-angle requirement into an economic perspective, the 23,536 lb weight penalty incurred with the 1° change is equivalent to the weight of 112 passengers and their baggage—nearly half the capacity of the aircraft. Thus, off-design requirements have a very significant impact on configuration design.

6.1.4 — Investigation for Local Minimum

The fact that the WFN_{m12} case was markedly superior to the wing-fuselage-nacelle design derived directly from the initial configuration suggests that the latter was a local minimum. One means to investigate this possibility was to evaluate the performance of a series of designs, defined as a function of ξ in Eq. (5.1), between the first result (x_0) and the WFN_{m12} design (x_1). Fig. 6.10 shows the gross weight variation and Fig. 6.11 shows the range of the designs between these two design points. Recall that the range constraint is 5,500 $n.\ mi.$, and note that the range performance deteriorates between the two designs before it regains its required level. Thus, there may be a constraint boundary between these two designs. This evidence supports the conclusion that the first wing-fuselage-nacelle design was a local minimum.

Had a second optimization not been started from the W_{m12} wing design, the superior WFN_{m12} might not have been discovered. Thus, it appears that for a design space characterized with a wavy behavior of a major constraint (see Fig. 6.11), it is important to try more than one optimization starting point.
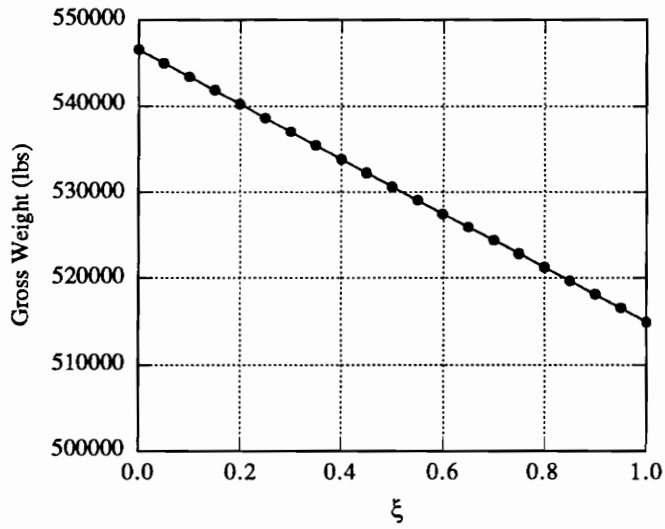
Fig. 6.10 — Gross Weight Variation between Wing-Fuselage-Nacelle Design Started from Initial Configuration, and WFN_{m12} Design
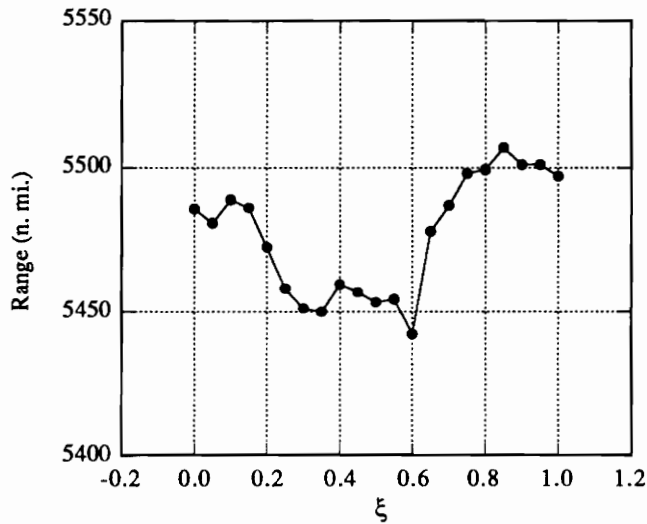
Fig. 6.11 — Range Variation between Wing-Fuselage-Nacelle Design Started from Initial Configuration, and WFN_{m12} Design

6.2 — Composite-Wing-Structure Optimization Cases

To investigate the influence of wing-structure technology on the configuration design, two designs were developed assuming composite, aeroelastically-tailored wings. To represent this choice of wing structure, I used $f_{comp} = f_{aert} = 1.0$ in Eq. (5.17). The three cases presented are two wing-alone and one wing-fuselage-nacelle optimizations, each with the nominal 12° landing angle-of-attack requirement.
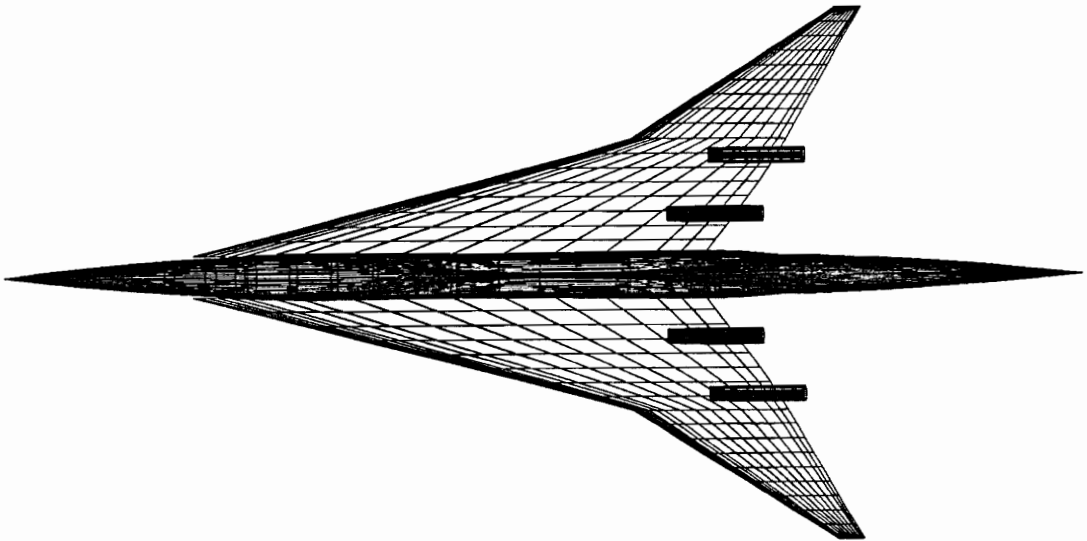
Fig. 6.12 — Composite-Wing Wing-Alone Design (W_{c12})

Table 6.5. Move Limits Used for W_{c12} Case

Design Cycle	Design Variable Move Limits
1-5	7%
6-15	5%
16-40	3%
41-45	2%

6.2.1 — Wing-Alone Case (W_{c12})

For this case, the 16 wing-design variables and the nominal constraint values listed in Ch. 3 were used. The initial design for the W_{c12} case was the parametric model corresponding to the baseline configuration. This case converged in 45 design cycles and is shown in Fig. 6.12. The move limits used for the different cycles are shown in Table 6.5. Convergence histories of the gross weight, the range and the landing angle of attack are shown in Figs. 6.13 and 6.14, respectively.
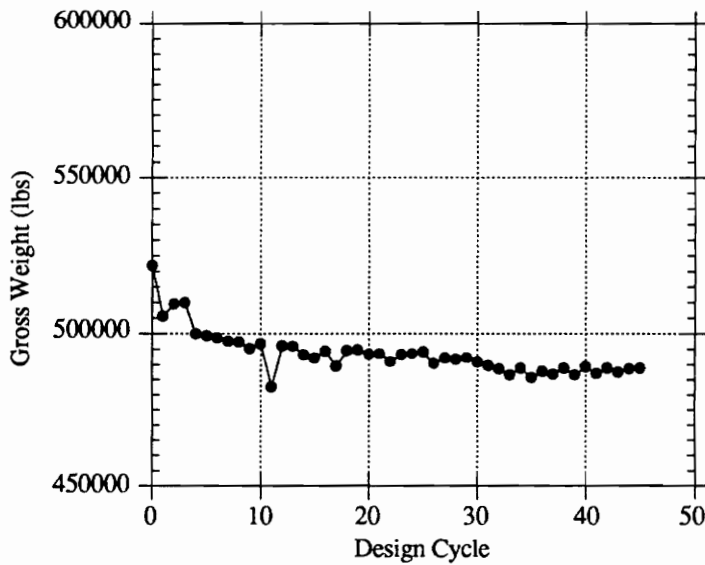
Fig. 6.13 — Gross Weight Convergence History for W_{c12} Case

Table 6.6. Move Limits Used for W_{c12_2} Case

Design Cycle	Design Variable Move Limits
1-2	5%
3-6	3%
7-10	2%
11-16	1%
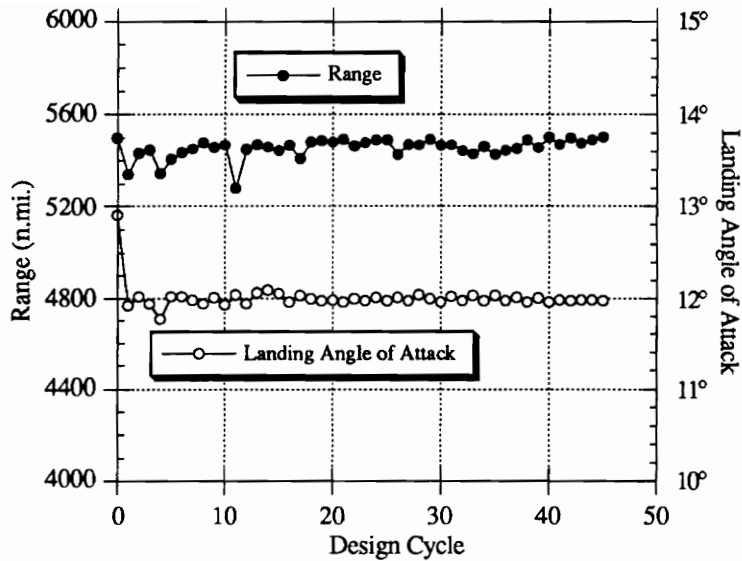
Fig. 6.14 — Range and Landing-Angle-of-Attack Convergence History for W_{c12} Case

6.2.2 — Second Wing-Alone Case (W_{c12_2})

The experience with the metallic-wing *WFN* cases, coupled with the fact that the aerodynamic performance of the W_{c12} case was lower than the W_{m12} case (see Tables 6.4 and 6.8), indicated that a second composite-wing wing-alone case should be investigated. This second case, W_{c12_2}, was started with the converged W_{m12} design variables and converged in 16 cycles; the design is shown in Fig. 6.15. The move limits employed for this case are shown in Table 6.6. Figs. 6.16 and 6.17 show the gross weight, range and landing-angle convergences.

6.2.3 — Wing-Fuselage-Nacelle Case (WFN_{c12})

For this case, the full set of 26 design variables was used. Again, the nominal constraint values listed in Ch. 3 were employed. The experience gained from developing the WFN_{m12} design prompted the choice of this design as the starting point for the WFN_{c12} optimization. This case converged in just 18 design cycles and is shown in Fig. 6.18. The move limits used for the design are shown in Table 6.7.
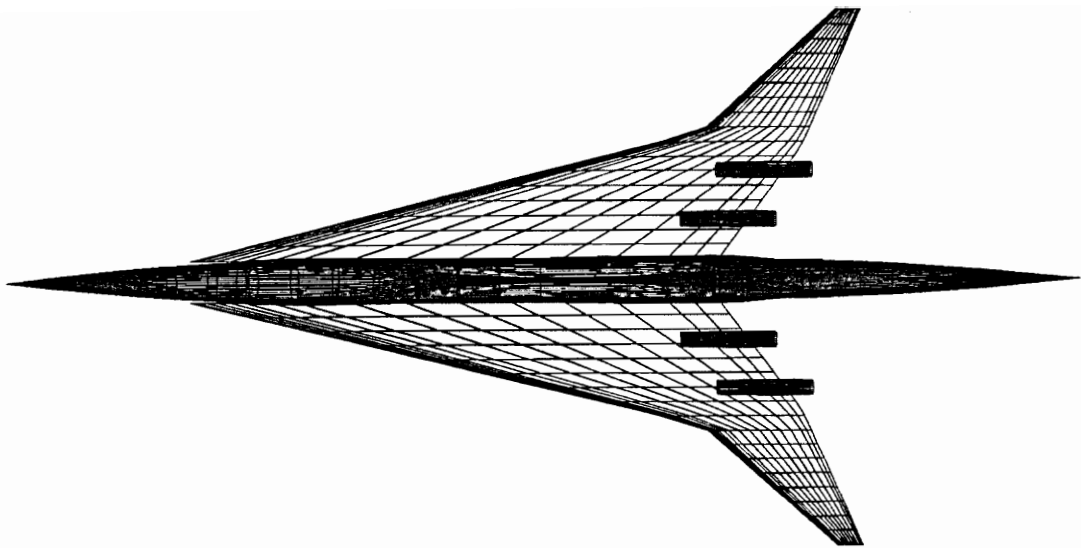
Fig. 6.15 — Second Composite-Wing Wing-Alone Design (W_{c12_2})
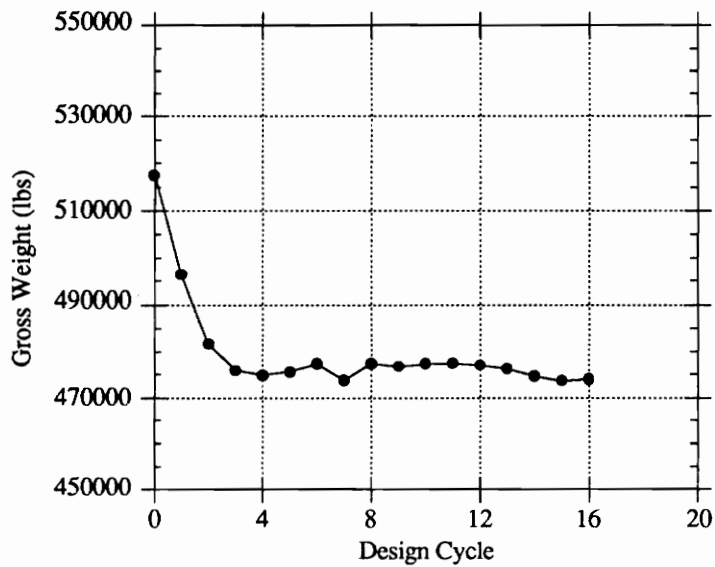
Fig. 6.16 — Gross Weight Convergence History for W_{c12_2} Case
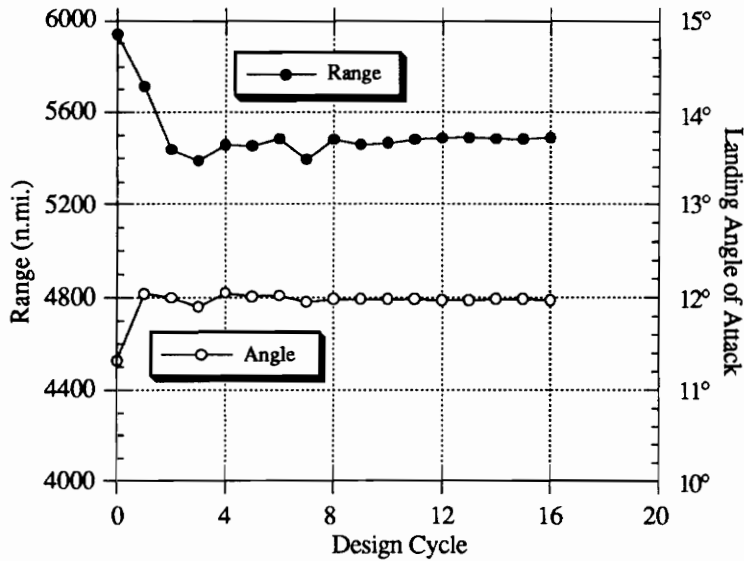
Fig. 6.17 — Range and Landing-Angle-of-Attack Convergence History for W_{c12_2} Case

Finally, convergence histories are presented in Figs. 6.19 and 6.20.

A summary of the characteristics of the initial and final composite-wing designs is presented in Table 6.8. Again, the designs achieved reductions in gross weight through decreased mission fuel from improved aerodynamic efficiency.

The W_{c12} design achieved a 6.3% reduction in gross weight from the initial design through a 14.8% reduction in mission fuel, at the expense of an increase in wing weight. The W_{c12_2} design, by contrast, achieved a 9.1% gross weight reduction by decreasing mission fuel 18.3%; the wing weight for this design exhibits less penalty than does the W_{c12} design. Clearly, the W_{c12_2} is superior to the W_{c12} design, which again highlights the importance of starting at different design points. The WFN_{c12} design had a gross weight 12.5% less than the initial design and 3.7% less than the W_{c12_2} configuration. As with the WFN_{m12} case, the improved aerodynamic perfomance cost less in terms of wing weight for the WFN_{c12} design than for the W_{c12} and W_{c12_2} designs: 2.4% weight penalty compared to 13.3% and 4.2% for the W_{c12}
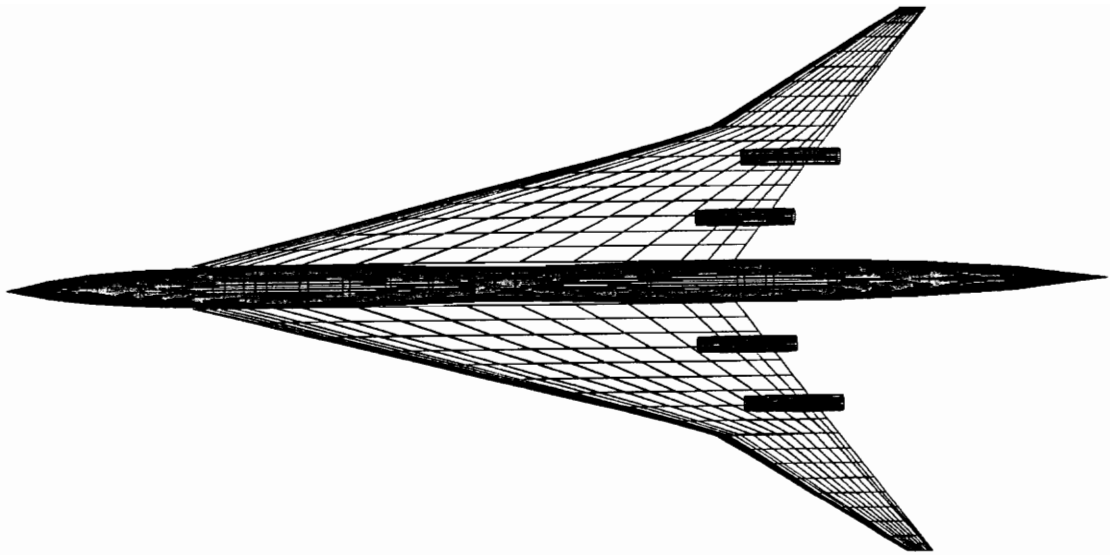
Fig. 6.18 — Composite-Wing Wing-Fuselage-Nacelle Design (WFN_{c12})

Table 6.7. Move Limits Used for WFN_{c12} Case

Design Cycle	Design Variable Move Limits
1-2	5%
3-10	3%
11-18	2%

and W_{c12_2} cases, respectively.

In comparison to their metal-wing counterparts, W_{c12} and WFN_{c12} weighed 11.9% and 11.4% less. Of these reductions, only 53.2% and 46.3%, respectively, came directly from reductions in wing weight. Thus, weight reduction in the wing was highly leveraged; every pound saved in the wing was worth roughly two pounds in the gross weight.

Tables 6.9 through 6.14 list the design variables at the beginning and end of each optimization case presented in this chapter.
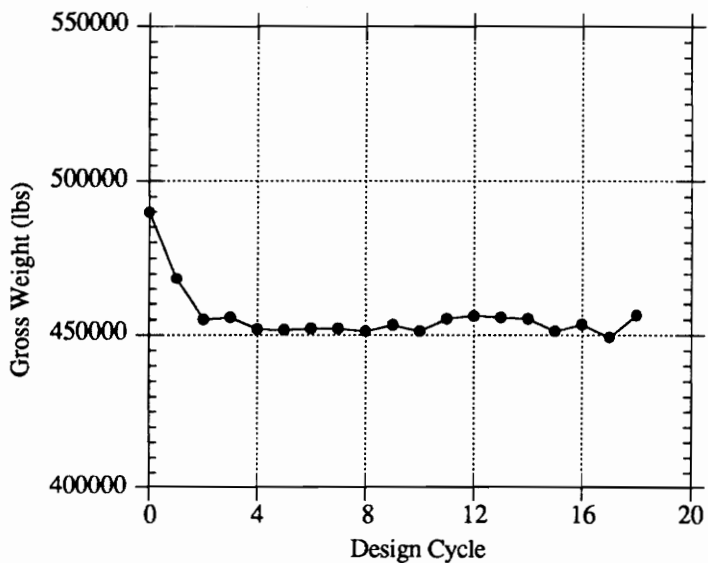
Fig. 6.19 — Gross Weight Convergence History for WFN_{c12} Case
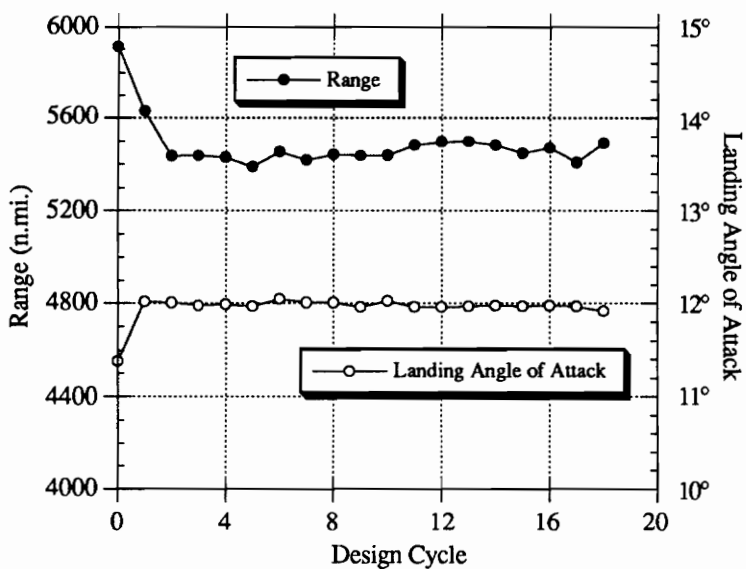
Fig. 6.20 — Range and Landing-Angle-of-Attack Convergence History for WFN_{c12} Case

Table 6.8. Initial and Final Design Features

(Composite-Wing-Structure Cases)

|	Initial	W_{c12}	W_{c12_2}	WFN_{c12}
Gross Wt. (*lbs*)	521,713	488,589	473,977	456,287
Fuel Wt. (*lbs*)	269,885	230,072	220,463	206,023
Fuel / Gross	51.7%	47.1%	46.5%	45.1%
Wing Wt. (*lbs*)	49,014	55,550	51,075	50,176
Fus. Wt. (*lbs*)	40,148	40,148	40,148	38,651
Wing Area (ft^2)	9,100	10,096	9,966	10,056
Wing Load (*psf*)	57.33	48.39	47.56	45.37
Aspect Ratio	2.36	2.39	2.46	2.36
Root t/c (%)	2.96	2.45	2.18	2.23
Break t/c (%)	2.36	1.54	1.63	1.71
Tip t/c (%)	2.15	1.51	1.51	1.53
LE Sweep	74.0°	74.9°	75.6°	75.4°
	45.0°	56.8°	47.4°	57.7°
TE Sweep	0.0°	36.7°	36.2°	36.3°
	8.4°	29.3°	23.5°	37.9°
Range (*n. mi.*)	5,500	5,501	5,491	5,491
Landing Angle	12.9°	11.97°	12.00°	11.92°
$(L/D)_{max}$	9.53	10.90	11.11	11.56

Table 6.9 Starting and Ending Design Variables for W_{m12} Optimization Case

Starting Values	Ending Values	Description
142.01	169.47	Wing root chord (ft)
99.65	143.34	LE break, x (ft)
28.57	37.73	LE break, y (ft)
142.01	176.05	TE break, x (ft)
28.57	30.39	TE break, y (ft)
138.40	189.83	LE of wing tip, x (ft)
9.30	7.02	Tip chord (ft)
67.32	74.33	Wing semi-span (ft)
0.50	0.48	Chordwise location of max. t/c
4.00	3.20	Airfoil LE radius parameter, I
2.96	2.14	Airfoil t/c at root (%)
2.36	1.73	Airfoil t/c at LE break (%)
2.15	1.51	Airfoil t/c at tip (%)
290,905	254,590	Mission fuel (lbs)
50,000	36,063	Starting cruise altitude (ft)
100	523	Cruise climb rate (ft/min)

Table 6.10 Starting and Ending Design Variables for WFN_{m12} Optimization Case

Starting Values	Ending Values	Description
169.47	148.62	Wing root chord (ft)
143.34	138.82	LE break, x (ft)
37.73	39.76	LE break, y (ft)
176.05	169.96	TE break, x (ft)
30.39	38.31	TE break, y (ft)
189.83	184.98	LE of wing tip, x (ft)
7.02	7.01	Tip chord (ft)
74.33	76.57	Wing semi-span (ft)
0.48	0.48	Chordwise location of max. t/c
3.20	4.64	Airfoil LE radius parameter, I
2.14	2.51	Airfoil t/c at root (%)
1.73	2.06	Airfoil t/c at LE break (%)
1.51	1.54	Airfoil t/c at tip (%)
70.00	34.00	Fuselage restraint 1, x (ft)
6.00	4.85	Fuselage restraint 1, r (ft)
135.00	136.45	Fuselage restraint 2, x (ft)
5.80	4.94	Fuselage restraint 2, r (ft)
170.00	149.57	Fuselage restraint 3, x (ft)
5.80	5.07	Fuselage restraint 3, r (ft)
215.00	250.15	Fuselage restraint 4, x (ft)
6.00	4.92	Fuselage restraint 4, r (ft)
17.79	17.14	Nacelle 1, y (ft)
32.07	38.25	Nacelle 2, y (ft)
254,590	236,514	Mission fuel (lbs)
36,063	20,303	Starting cruise altitude (ft)
523	1,355	Cruise climb rate (ft/min)

Table 6.11. Starting and Ending Design Variables for WFN_{m11} Optimization Case

Starting Values	Ending Values	Description
148.62	163.94	Wing root chord (ft)
138.82	136.72	LE break, x (ft)
39.76	37.11	LE break, y (ft)
169.96	175.30	TE break, x (ft)
38.31	40.05	TE break, y (ft)
184.98	179.04	LE of wing tip, x (ft)
7.01	7.00	Tip chord (ft)
76.57	80.92	Wing semi-span (ft)
0.48	0.49	Chordwise location of max. t/c
4.64	4.65	Airfoil LE radius parameter, I
2.51	2.57	Airfoil t/c at root (%)
2.06	2.04	Airfoil t/c at LE break (%)
1.54	1.56	Airfoil t/c at tip (%)
34.00	27.32	Fuselage restraint 1, x (ft)
4.85	4.46	Fuselage restraint 1, r (ft)
136.45	131.00	Fuselage restraint 2, x (ft)
4.94	4.61	Fuselage restraint 2, r (ft)
149.57	143.28	Fuselage restraint 3, x (ft)
5.07	4.58	Fuselage restraint 3, r (ft)
250.15	246.57	Fuselage restraint 4, x (ft)
4.92	4.98	Fuselage restraint 4, r (ft)
17.14	14.47	Nacelle 1, y (ft)
38.25	40.45	Nacelle 2, y (ft)
236,514	248,387	Mission fuel (lbs)
20,303	15,656	Starting cruise altitude (ft)
1,355	1,494	Cruise climb rate (ft/min)

Table 6.12 Starting and Ending Design Variables for W_{c12} Optimization Case

Starting Values	Ending Values	Description
142.01	144.02	Wing root chord (ft)
99.65	122.42	LE break, x (ft)
28.57	32.96	LE break, y (ft)
142.01	162.23	TE break, x (ft)
28.57	24.46	TE break, y (ft)
138.40	181.57	LE of wing tip, x (ft)
9.30	7.17	Tip chord (ft)
67.32	71.64	Wing semi-span (ft)
0.50	0.48	Chordwise location of max. t/c
4.00	4.62	Airfoil LE radius parameter, I
2.96	2.45	Airfoil t/c at root $(\%)$
2.36	1.54	Airfoil t/c at LE break $(\%)$
2.15	1.51	Airfoil t/c at tip $(\%)$
269,885	230,072	Mission fuel (lbs)
50,000	37,796	Starting cruise altitude (ft)
100	471	Cruise climb rate (ft/min)

Table 6.13 Starting and Ending Design Variables for W_{c12_2} Optimization Case

Starting Values	Ending Values	Description
169.47	149.52	Wing root chord (ft)
143.34	144.91	LE break, x (ft)
37.73	37.15	LE break, y (ft)
176.05	173.39	TE break, x (ft)
30.39	32.66	TE break, y (ft)
189.83	183.15	LE of wing tip, x (ft)
7.02	7.16	Tip chord (ft)
74.33	72.37	Wing semi-span (ft)
0.48	0.41	Chordwise location of max. t/c
3.20	2.97	Airfoil LE radius parameter, I
2.14	2.18	Airfoil t/c at root (%)
1.73	1.63	Airfoil t/c at LE break (%)
1.51	1.51	Airfoil t/c at tip (%)
254,590	220,463	Mission fuel (lbs)
36,063	35,433	Starting cruise altitude (ft)
523	546	Cruise climb rate (ft/min)

Table 6.14. Starting and Ending Design Variables for WFN_{c12} Optimization Case

Starting Values	Ending Values	Description
148.62	148.64	Wing root chord (ft)
138.82	140.98	LE break, x (ft)
39.76	36.60	LE break, y (ft)
169.96	172.80	TE break, x (ft)
38.31	32.87	TE break, y (ft)
184.98	195.42	LE of wing tip, x (ft)
7.01	7.08	Tip chord (ft)
76.57	71.08	Wing semi-span (ft)
0.48	0.47	Chordwise location of max. t/c
4.64	4.50	Airfoil LE radius parameter, I
2.51	2.23	Airfoil t/c at root (%)
2.06	1.71	Airfoil t/c at LE break (%)
1.54	1.53	Airfoil t/c at tip (%)
34.00	26.23	Fuselage restraint 1, x (ft)
4.85	4.36	Fuselage restraint 1, r (ft)
136.45	132.57	Fuselage restraint 2, x (ft)
4.94	4.77	Fuselage restraint 2, r (ft)
149.57	144.47	Fuselage restraint 3, x (ft)
5.07	4.82	Fuselage restraint 3, r (ft)
250.15	244.18	Fuselage restraint 4, x (ft)
4.92	4.99	Fuselage restraint 4, r (ft)
17.14	18.06	Nacelle 1, y (ft)
38.25	35.20	Nacelle 2, y (ft)
236,514	206,023	Mission fuel (lbs)
20,303	13,185	Starting cruise altitude (ft)
1,355	1,611	Cruise climb rate (ft/min)

It can be difficult, in the midst of the technical details of implementation and operation, to step back a bit and attempt to draw general conclusions about the applicability and use of an ongoing research project. There are, nonetheless, a number of conclusions and observations to be made.

The geometric parameterization methods developed for this work have been and should continue to be very useful. The blended-linear-equation strategy used to define the wing planform is a technique that could readily be applied to a variety of aircraft types—it is certainly not limited to HSCT-type planforms. The airfoil thickness distribution and rules used to link the planform to the wing-section shape are somewhat less general in applicability, but they serve to illustrate an important point. In order to keep the number of design variables used in an optimization problem to a reasonable number, it is valuable to reduce the definition to a few, relatively intuitive, design parameters. In this particular instance, the entire wing thickness distribution was described with just 5 parameters.

For the definition of a simple, axi-symmetric fuselage, the minimum-wave-drag-body approach is appropriate. It has the advantage of incorporating length and volume requirements directly into the formulation and, in addition, builds in low wave drag characteristics implicitly. It is somewhat less applicable generally than the wing-planform definition, in that it would be impossible to model more general, non-axisymmetric, fuselages with this technique.

One basic measure of the success of the geometric parameterization is that, with only 26 parameters used to define the configuration and mission, the optimizer still had sufficient freedom to satisfy the constraints and reduce the gross weight.

The sequential approximate optimization procedure, outlined in Ch. 3, works and effectively reduces the computational expense associated with complex problems. Although only the GLA method is used for approximating analyses, the lin-

ear and scaled approximations are also options for approximating detailed analysis methods. As stated in Ch. 5, the derivative-based methods (global-local and linear) are preferable to the scaled approximation since they allow the detailed analyses to influence the optimization more directly. There are, however, instances when the scaled approximation is an appropriate choice; for example, when an extremely expensive analysis method makes the calculation of derivatives impractical. Ref. 24 presents some optimization results obtained using the scaled approximation.

The variable-complexity strategy was demonstrated through the use of several simple aerodynamic models, and the simple structural (*i.e.*, weight) model. The coupling of simple and more detailed models in the optimization procedure effectively reduces the computational expense. Through the use of the weight equations, the general effects of structural considerations have been incorporated in the design. This approach allowed the optimization to proceed efficiently, and at the same time retained the multidisciplinary nature of the problem.

As was demonstrated by the preliminary results obtained using only the conceptual-level angle-of-attack models in Ch. 5, simple analysis techniques cannot be blindly applied to aircraft configurations for which they were not designed. This observation raises a similar issue related to the structural modeling used in the optimization. If the optimizer so successfully exploited weaknesses in the simple landing angle-of-attack models, it might have been just as successful finding weaknesses in the conceptual-level weight estimation methods used to evaluate the optimization objective function. This issue could be addressed using a variable-complexity approach to model the structure of the aircraft, specifically the wing.

The capability of the optimization was illustrated by the 6 case studies in the previous chapter. Although these cases only explored a few of the total number of possible design problems, they illustrated the basic influence of wing structure, full configuration design versus wing-alone design, and off-design performance requirements. The requirements of design range and the off-design landing-angle-of-attack

limitation were successfully integrated and designs developed that indicate significant improvements in aerodynamic performance and reduction in gross weight. Further, the impact of structural design technology was easily incorporated into several design cases. The ability to integrate a large number of design considerations simultaneously is one of the strengths of formalized optimization procedures.

Optimization methods are particularly useful in situations where the available design trades are not obvious *a priori*. For example, the position of the engine nacelles on the wing directly influences the wing weight, and at the same time affects the configuration wave drag. Given the difficulty of visualizing the effect of geometric changes upon the wave drag (the effect on wing weight is more straightforward), this is the sort of situation in which optimization methods are especially valuable. Thus, multi-disciplinary optimization can effectively balance competing requirements within separate disciplines, provided the issue of computational expense is addressed. In fact, the ultimate goal is to achieve not merely an acceptable compromise between requirements, but to derive a synergistic or complementary solution.

It seems inevitable, at the conclusion of a project such as this, that many things come to mind that have not been investigated that should or could be. This effort is no exception, and so I have the following recommendations for future work.

Smooth Supersonic Drag-due-to-Lift Calculation. The numerical noise associated with the supersonic panel code stands in the way of significantly larger move limits in the optimization process. One of the most significant improvements to the methodology presented here would be an effective way of dealing with this analysis noise. Although it would certainly be desirable to devise a panel method that was not subject to this problem, the issue of analysis noise is almost certainly not limited to this particular technique. Consequently, one valuable branch of optimization research would be the development of systematic methods used to address this problem.

Camber Considerations. The wing is this work has not included camber, although the method of generating the drag polar simulates the effects of a proper camber design. The assumption has been that the cambering of the wing, given the planform and thickness distribution, will have little effect on the vehicle gross weight and can, therefore, be accomplished after the configuration optimization. Camber should be included once issues of lift distribution on the wing (*e.g.*, for sonic-boom or trim considerations) become important.

Trim Considerations. Beyond fixing the quarter-chord location of the wing's MAC, no trim considerations were included in this problem. Two technical demands become important for their inclusion: center-of-gravity location estimation, and aerodynamic moment calculations. Addressing these opens up several interesting possibilities: configuration optimization including canards or horizontal tails, inclusion of engine-out stability requirements, estimation of basic dynamic characteristics, and incorporation of control-power requirements in the design.

Sonic-Boom Considerations. The sonic-boom characteristics of a given configuration are calculated using several concepts related to the wave-drag estimation methods. The far-field boom signature is determined from an equivalent-body area distribution formed from a wave-drag equivalent body in conjunction with a second area distribution on the wing. Traditionally, low-boom configurations have relied entirely on fuselage shaping in the presence of a given lift distribution and have incurred significant performance penalties. Simultaneous design of the fuselage and wing (and, thus, the lift distribution) using optimization methods could produce designs with acceptably low boom characteristics that retain high levels of performance.

Mission Profile Changes. The mission profile implemented in the present work is a very simple one, consisting solely of a supersonic cruise leg. Inclusion of additional mission features, most notably a subsonic cruise leg, would require only the addition of subsonic drag computation and some minor revisions to the range

calculation technique, but would allow more realistic mission definitions.

Detailed Structural Considerations. The choice of structural material employed in the aircraft's wing was shown in Ch. 6 to have a significant impact on the optimized configuration. Because the changes in wing weight are so highly leveraged on a final design, the wing is a natural candidate for structural optimization. Secondly, such investigation addresses the issue of whether or not the optimizer has taken advantage of the simple structures (weight) model.

I want to conclude on a personal note, and this list of future-work items provides an oddly appropriate context. If I had been asked $3\frac{1}{2}$ years ago what I hoped to accomplish as a graduate student, I doubt whether I would have been able to outline the work presented here and, further, I think I would have been surprised at its eventual scope. A number of courses, many hours before computer terminals, and quite a few late nights later I am satisfied with my progress but I also am freshly aware that it is only a beginning. One of the more humbling aspects of continued education is its tendency to highlight how much more there is to learn and to investigate. To those that (I hope) continue this research into advanced design techniques beyond my academic tenure, I have but one word of encouragement: enjoy it. I certainly have.

References

1. de Saint-Exupéry, A., *Airman's Odyssey*, Harcourt Brace Jovanovich, 1984, pp. 38-39.

2. Steiner, J.E., Bowes, G.M., Maxam, F.G., Wallick, S.L., and Gregoire, M.C., *Case Study in Aircraft Design—The Boeing 727*, AIAA Professional Study Series, September 1978, p. 24.

3. Grossman, B., Strauch, G.J., Eppard, W.M., Gürdal, Z., and Haftka, R.T., "Integrated Aerodynamic/Structural Design of a Sailplane Wing", AIAA Paper 86-2623, October 1986.

4. Haftka, R.T., Grossman, B., Eppard, W.M., Kao, P.J., and Polen, D., "Efficient Optimization of Integrated Aerodynamic-Structural Design," *International J. for Numerical Methods in Engineering*, **28**, 1989, pp. 593-607.

5. Grossman, B., Haftka, R.T., Kao, P.J., Polen, D.M., Rais-Rohani, M., and Sobieszczanski-Sobieski, J., "Integrated Aerodynamic-Structural Design of a Transport Wing", *J. of Aircraft*, **27**, No. 12, 1990, pp. 1050-1056.

6. Unger, E.R., Rais-Rohani, M., Hutchison, M.G., Haftka, R.T., and Grossman, B., "Multidisciplinary Design of a Subsonic Transport Wing", Proceedings of the Third Air Force/NASA Symposium on Recent Advances in Multidisciplinary Analysis and Optimization, San Francisco, CA, September 1990.

7. Rais-Rohani, M., "Integrated Aerodynamic-Structural-Control Wing Design", Ph.D. Dissertation, Virginia Polytechnic Institute and State University, August 1991.

8. Malone, B. and Mason, W.H., "Multidisciplinary Design Optimization in Aircraft Design using Analytic Technology Models," AIAA Paper 91-3187, September 1991.

9. McGeer, T., "Wing Design for Minimum Drag with Practical Constraints", *J. of Aircraft*, **21**, No. 11, 1984, pp. 879-920.

10. Gallman, J.W., Kroo, I.M., and Smith, S.C., "Design Synthesis and Optimization of Joined-Wing Transports", AIAA Paper 90-3197, September 1990.

11. Wrenn, G.A., and Dovi, A.R., "Multilevel Decomposition Approach to the Preliminary Sizing of a Transport Aircraft Wing", *J. of Aircraft*, **25**, No. 7, 1988, pp. 632-638.

12. Sobieszczanski-Sobieski, J., "Sensitivity Analysis and Multidisciplinary Optimization for Aircraft Design: Recent Advances and Results", *I.C.A.S.*, Paper 88-1.7.3, 1988.

13. Sobieszczanski-Sobieski, J., "On the Sensitivity of Complex Internally Coupled Systems", AIAA Paper CP-88-2378, and *AIAA Journal*, **28**, No. 1, 1990,

pp. 153-160.

14. Vanderplaats, G.N., "Automated Optimization Techniques for Aircraft Synthesis", AIAA Paper 76-909, Sept. 1976.

15. Stubbe, J.R., "PAYCOS—A Multidisciplinary Design Optimization Tool for Hypersonic Vehicle Design", AIAA Paper 92-4723, September 1992.

16. Volk, J., "Multidisciplinary Design Environment Development for Air Vehicle Engineering," AIAA Paper 92-1113, September 1992.

17. Welge, R.H., "Aerodynamic Technology Opportunities for a High-Speed Civil Transport", SAE Paper 881354, October 1988.

18. Kulfan, R.M., "Application of Favorable Aerodynamic Interference to Supersonic Airplane Design", SAE Paper 901988, October 1990.

19. Coen, P.G., Sobieszczanski-Sobieski, J., Dollyhigh, S.M., "Preliminary Results from the High-Speed Airframe Integration Research Project", AIAA 92-1004, February 1992.

20. Dovi, A.R., Wrenn, G.A., Barthelemy, J.-F.M., Coen, P.G., and Hall, L.E., "Multidisciplinary Design Integration System for a Supersonic Transport Aircraft", AIAA Paper 92-4841, September 1992.

21. Röhl, P. and Schrage, D., "Preliminary Wing Design of a High Speed Civil Transport Aircraft by Multilevel Decomposition Techniques," AIAA Paper 92-4721, September 1992.

22. Chang, I.C., Torres, F.J., "Wing Design Code Using Three-Dimensional Euler Equations and Optimization", AIAA Paper 91-3190, September 1991.

23. Nelson, C.P., "Effects of Wing Planform on HSCT Off-Design Aerodynamics", AIAA Paper 92-2629, June 1992.

24. Hutchison, M. G., Unger, E. R., Mason, W., Grossman, B., and Haftka, R. T., "Variable-Complexity Aerodynamic Optimization of an HSCT Wing Using Structural Wing-Weight Equations," AIAA Paper 92-0212, Jan. 1992; see also "Variable-Complexity Aerodynamic Optimization of a High-Speed Civil Transport Wing", *J. Aircraft*, (to appear).

25. Craidon, C.B., "Description of a Digital Computer Program for Airplane Configuration Plots", NASA TM X-2074, 1970.

26. Abbott, I.H., and von Doenhoff, A.E., *Theory of Wing Sections—Including a Summary of Airfoil Data*, Dover, 1959.

27. Barnwell, R., "Approximate Method for Calculating Transonic Flow About Lifting Wing-Body Configurations", NASA TR R-452, April 1976, pp. 58–61.

28. Mason, W.H., Siclari, M.J., Miller, D.S., and Pittman, J.L., "A Supersonic Maneuver Wing Designed for Nonlinear Attached Flow," AIAA Paper 83-0425, January 1983.

29. Eminton, E., "On the Minimisation and Numerical Evaluation of Wave Drag," Royal Aircraft Establishment Report AERO.2564, November 1955.

30. Grandhi, R.V., Thareja, R., and Haftka, R.T., "NEWSUMT-A: A General Purpose Program for Constrained Optimization using Constraint Approximations," *ASME Journal of Mechanisms, Transmissions and Automation in Design*, 107, pp. 94-99, 1985.

31. Haftka, R. T., "Combining Global and Local Approximations", *AIAA J.*, **29**, No. 9, Sept. 1991, pp. 1523-1525.

32. Johnson, V.S., "Life Cycle Cost in the Conceptual Design of Subsonic Commercial Aircraft", Ph.D. Dissertation, University of Kansas, May 1989.

33. Anderson, J.D., *Introduction to Flight, 3rd Edition*, McGraw-Hill Book Company, 1989.

34. Hutchison, M.G., Huang, X., Mason, W.H., Haftka, R.T., Grossman, B., "Variable-Complexity Aerodynamic-Structural Design of a High-Speed Civil Transport Wing", AIAA Paper 92-4695, Sept. 1992.

35. Ashley, H., and Landahl, M., *Aerodynamics of Wings and Bodies*, Dover, New York, 1985.

36. Eminton, E. and Lord, W.T., "Note on the Numerical Evaluation of the Wave Drag of Smooth Slender Bodies Using Optimum Area Distributions for Minimum Wave Drag", *J. of the Royal Aeronautical Society*, January 1956, pp. 61-63.

37. Hildebrand, F.B., *Advanced Calculus for Application, 2nd Edition*, Prentice-Hall, Inc., 1976.

38. Eminton, E., "On the Numerical Evaluation of the Drag Integral", ARC Reports and Memoranda No. 3341, October 1961.

39. Harris, Roy V., Jr., "An Analysis and Correlation of Aircraft Wave Drag", NASA TM X-947, 1964.

40. Lomax, H., Heaslet, M.A., and Fuller, F.B., "Integrals and Integral Equations in Linearized Wing Theory", NACA Report 1054, 1951.

41. Carlson, H. W., Miller, D. S., "Numerical Methods for the Design and Analysis of Wings at Supersonic Speeds", NASA TN D-7713, 1974.

42. Carlson, H. W., Mack, R. J., "Estimation of Leading-Edge Thrust for Supersonic Wings of Arbitrary Planforms", NASA TP-1270, 1978.

43. Carlson, H. W., Mack, R. J., Barger, R. L., "Estimation of Attainable Leading-Edge Thrust for Wings at Subsonic and Supersonic Speeds", NASA TP-1500, 1979.

44. Jones, R.T, and Cohen, D., *High-Speed Wing Theory*, Princeton University Press, 1960.

45. Hopkins, E.J., and Inouye, M., "An Evaluation of Theories for Predicting Turbulent Skin Friction and Heat Transfer on Flat Plates at Supersonic and Hypersonic Mach Numbers," *AIAA J.*, **9**, No. 6, June 1971, pp. 993-1003.

46. Mason, W.H., *Pak #4—Boundary Layer Analysis Methods*, Aerocal, Huntington, NY, 1981.

47. Hoerner, S.F., *Fluid-Dynamic Drag*, Hoerner, 1965.

48. Rech, J. and Leyman, C.S., "A Case Study by Aerospatiale and British Aerospace on the Concorde", AIAA Professional Study Series.

49. Polhamus, E.C., "Prediction of Vortex-Lift Characteristics by a Leading-Edge-Suction Analogy", *J. Aircraft*, Vol. 8, April 1971, pp. 193–199.

50. Bertin, J.J. and Smith, M.L., *Aerodynamics for Engineers, 2nd Edition*, Prentice Hall, 1989.

51. Margason, R.J. and Lamar, J.E., "Vortex-Lattice FORTRAN Program for Estimating Subsonic Aerodynamic Characteristics of Complex Planforms", NASA TN D-6142, February 1971.

52. Küchemann, D., *The Aerodynamic Design of Aircraft*, Pergamon Press, 1978, pp. 404–405.

53. Cohen, D. and Friedman, M.D., "Theoretical Investigation of the Supersonic Lift and Drag of Thin, Sweptback Wings with Increased Sweep near the Root," NACA TN-2959, June 1953.

54. Ericsson, L.E., and Reding, J.P., "Nonlinear Slender Wing Aerodynamics", AIAA Paper 76-19, Jan. 1976.

55. Nicolai, L.M., *Fundamentals of Aircraft Design*, METS, Inc., San Jose, 1975.

56. Diederich, F.W., "A Planform Parameter for Correlating Certain Aerodynamic Characteristics of Swept Wings", N.A.C.A. TN-2335, 1951.

57. McCullers, L.A., "Aircraft Configuration Optimization Including Optimized Flight Profiles", NASA CP-2327, Proceedings of Symposium on Recent Experiences in Multidisciplinary Analysis and Optimization, J. Sobieski, compiler, April 1984, pp. 395–412.

Although not part of the theoretical development, there were several guiding principles used in the program development which made for easy implementation and code maintenance. These principles evolved over a period of time and were a result of the open-ended nature of this design problem. That is, it was not always clear at the beginning of the research what sort of analysis methods would be required or what performance characteristics were important. To facilitate the ongoing development, a computational framework had to be devised that allowed flexibility for both expansion and internal changes without requiring extensive rewrites of existing computer code. The basic data flow and analysis modules are illustrated in Fig. A.1.

I believe that careful design of such a framework is at least as important as the analysis and geometric methods themselves. Long-term programming projects have a way of acquiring an undesirable history over time, in the form of bug fixes or shortcuts "temporarily" inserted during development—which become permanent, if inadvertent, features. Eventually, these innocuous additions can become problem sources that can be extraordinarily difficult to understand and locate. This tendency is particularly evident in the inherently transient graduate environment, and often results in large investments of time and effort which could have been avoided through careful program design. Four related strategies were developed to minimize such unnecessary effort: limited data visibility, common geometry and mission descriptions for all analyses, isolation of the design variables, and analysis code modularity.

A.1 — Limited Data Visibility

This principle may be expressed succinctly as a programming mandate: functions and subroutines may *only* access and modify data explicitly passed in the calling statement. Globally visible data (*e.g.,* FORTRAN common blocks, or "ex-
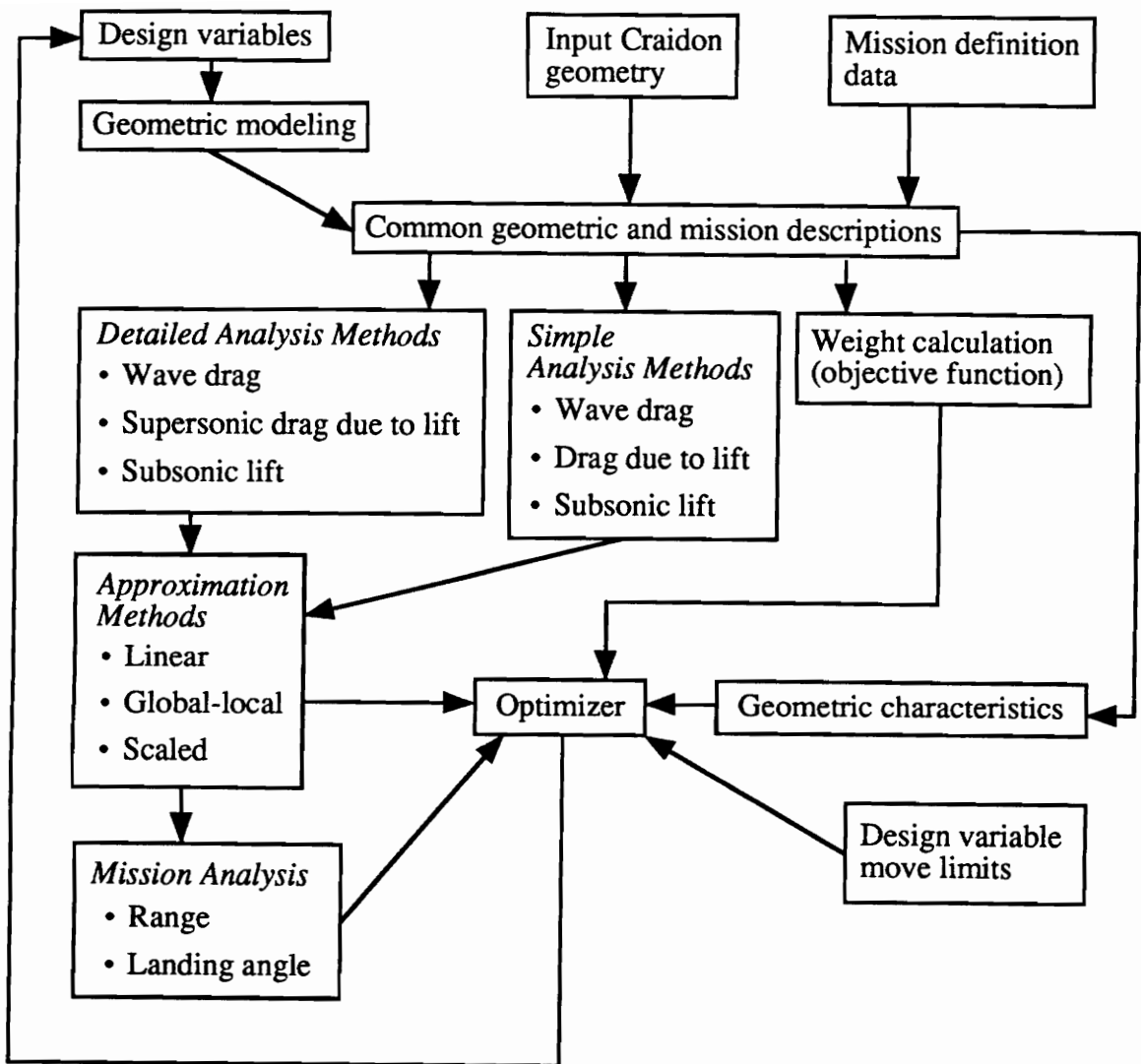
Fig. A.1 — Progam Analysis Modules and Data Flow

tern" variables in C) is appealing in that it dramatically reduces the length and complexity of function calls, but it often results in program bugs that are virtually impossible to locate and eliminate.

Such errors originate from data modification within a routine which has no apparent ability to change that data. Program bugs resulting from global data modification are especially difficult to understand when a person employs a function or routine written by someone else.

A.2 — Common Geometry and Mission Descriptions

A second, related principle is the use of common geometry and mission description formats. The geometry format was developed directly from the Craidon geometry description. Each of the analysis methods outlined in the following chapters has access to the configuration data and mission profile *only* through these universal descriptions. Consequently, all of the relevant information must be stored in this common format and each analysis method must be capable of interpreting the data into quantities specific to the given analysis (*e.g.*, wing planform coordinates for aerodynamic analysis).

This approach has proven especially valuable in a structural optimization research effort proceeding in parallel with the work presented here.[34] Although the design variables used in the structural optimization are completely different from those used in this work, the geometry description is the same and, thus, the aerodynamic and structural optimizations are linked only through this configuration description. Consequently, once this common format was agreed upon, both projects proceeded independently with the configuration optimization producing designs used for structural optimization studies.

A.3 — Separation of Design Variables and Geometry

As stated previously, I distinguish between the geometry definition and description. The geometry is defined using the design variables, but is described by the Craidon geometry format. This approach has the advantage that it effectively isolates the meaning of the design variables from the analysis.

There are only two routines in the program where the design variables are accessed for their specific meaning: in the geometry definition routine where the Craidon description is generated, and where explicit references are required in the calculation of the constraints. Since only these two routines depend on the design variable definitions, it is a relatively simple matter to change the meaning or number of the design variables. In contrast, if one set of design variables had been devised

and no intermediate description employed, the analysis methods would depend upon explicit design variable references. In this situation, changes to the design variables would be laborious and prone to errors, since the analysis codes themselves would have to be modified.

A.4 — Analysis Code Modularity

In some sense, this strategy comes about as a result of the previous three. By analysis modularity, I mean that the given analysis method is coded in such a way as to utilize only the data passed explicitly to it, that the method refers to the geometry and mission by the common data formats, and that the method does not refer explicitly to the design variables. Thus, the analysis methods may be upgraded or replaced with little or no impact on the rest of program.

Ideally, the function calls made to execute the given analysis would not change even if the analysis code were to be completely replaced. For example, the supersonic drag due to lift calculation is currently performed using a panel method that, by nature, produces a certain amount of numerical noise (see Chs. 4 and 5). It would eventually be desirable to replace this analysis code with one that produces smoothly varying results. Given the above requirements, such a replacement would not require any changes at all to the main program and could be integrated into the existing framework quickly and easily.

The author was born to Mr. and Mrs. Samuel Gerry Hutchison on September 10, 1964. After 18 years as a resident of the northern part of Virginia, he commenced his university education at Virginia Polytechnic Institute and State University in 1982. Upon completion of his Bachelor of Science degree in Mechanical Engineering in 1986, he took a job with the General Electric Company as a practicing engineer. October of 1987 marked his marriage to Catherine Mary Noone. In the fall of 1989, he returned to his *alma mater* to begin graduate studies and, during the spring of 1993, he completed his Doctor of Philosophy degree in Aerospace Engineering. The author then accepted a position as an engineer/analyst with the Aurora Flight Sciences Corporation of Manassas, Virginia.